

Electrochemical Energy Characteristics of Bismuth Oxide with Different Polymorphs

A Thesis

Presented in Partial Fulfillment of the Requirements for the

Degree of Master of Science

with a

Major in Materials Science and Engineering

in the

College of Graduate Studies

University of Idaho

By: Brandon Day

Major Professor: Krishnan Raja, Ph.D.

Committee Members: Vivek Utgikar, Ph.D.; Indrajit Charit, Ph.D.

Department Administrator: Eric Aston, Ph.D

May 2019

Authorization to Submit Thesis

This thesis of Brandon Day, submitted for the degree of Master of Science with a major in Materials Science and Engineering and titled “Electrochemical Energy Characteristics of Bismuth Oxide with Different Polymorphs”, has been reviewed in in final form. Permission, as indicated by the signatures and dates given below, is now granted to submit final copies to the College of Graduate Studies for approval.

Major Professor _____ Date _____

Krishnan Raja, Ph.D

Committee Members

_____ Date _____

Indrajit Charit, Ph.D

_____ Date _____

Vivek Utgikar, Ph.D

Department Administrator

_____ Date _____

D. Eric Aston, Ph.D

Abstract

Bismuth sesquioxide (Bi_2O_3) exists in six different polymorphs depending on its synthesis route and thermal treatments. Among these polymorphs monoclinic (alpha), tetragonal (beta), and cubic (delta) phases are widely used in different applications such as photocatalysts, gas and bio sensors, environmental remediation, and energy storage devices. In this study, bismuth oxide was synthesized by two different routes and two different configurations such as: 1) electrodeposited thin films on FTO or glass carbon substrates, and 2) chemically precipitated micron size particles. The as-synthesized material was amorphous. Two different crystalline structures (monoclinic and tetragonal) were obtained by appropriate precursor solutions and thermal annealing treatments. The energy storage characteristics of the amorphous and crystalline Bi_2O_3 were evaluated by a series of electrochemical techniques including cyclic voltammetry, galvanostatic charge-discharge cycling, impedance spectroscopy, and Mott-Schottky analyses. Electron microscopy, X-ray diffraction, and UV-Vis photo spectroscopy were used for material characterization before and after electrochemical testing. The experimental results indicated that the amorphous Bi_2O_3 had higher charge storage capacity than that of crystalline phases but the cyclic stability was inferior. While considering both the capacity and stability, the tetragonal Bi_2O_3 stabilized by Cr incorporation (chrombismite) showed promising results.

Acknowledgement

I would like to acknowledge my Advisor Dr. Krishnan Raja for accepting me as his graduate student. Additionally, I would like to acknowledge NEUP for funding this project, and also all my committee members for taking time out of their busy schedules to help me obtain my master's degree in Material Science and Engineering.

Dedication

I would like to thank my family for their support in wanting to pursue higher education. Additionally, I want to thank James Zillinger and Bethany Kersten for helping me get this project started when I first arrived in Moscow. Furthermore, I want to thank all my friends up here for helping me with characterization and Anumat for supplying all us graduate students with copious amounts of coffee to help keep the energy maintained. Also, in memory of Dr. Thomas Bitterwolf who was willing to be on my committee despite everything he had going on, you will be missed.

Table of Contents

Authorization to Submit Dissertation	ii
Abstract.....	iii
Acknowledgements.....	iv
Dedication.....	v
Table of Contents.....	vi
List of Figures.....	vii
List of Tables	xi
Chapter 1: Introduction.....	1
Chapter 2: Background	3
Chapter 3: Objective and Scope.....	5
Chapter 4: Experimental Procedure	5
Chapter 5: Results and Discussion.....	9
Chapter 6: Conclusions and Future Work.....	32
References.....	36
Appendix: Figures	38

List of Figures

Figure 1: Comparison of three energy storage systems	38
Figure 2: Capacitor Vs. Super Capacitor	38
Figure 3: Linear sweep voltammograms.....	39
Figure 4: Cyclic Voltammograms	39
Figure 5: Cyclic Voltammogram curve.....	40
Figure 6: α phase solution from left to right: Platinum Counter Electrode	40
Figure 7: β phase solution from left to right: Platinum Counter Electrode.....	41
Figure 8: Cyclic Voltammetry α phase varying scan rate comparison	41
Figure 9: Cyclic Voltammetry β phase varying scan rate comparison	42
Figure 10: FTO glass deposition from left to right: As-deposited Chrombismite	43
Figure 11: α phase deposit on FTO glass cyclic voltammetry	43
Figure 12: UV-Vis spectrum of α phase during potentiostatic experiment at 1.08 V.....	44
Figure 13: Potentiometric V-t Galvanostatic electrodeposition of α and β Bi_2O_3	44
Figure 14: 10 second α deposition on glassy carbon	45
Figure 15: 30 second α deposition on glassy carbon	45
Figure 16: 60 second α deposition on glassy carbon	46
Figure 17: 300 second α deposition on glassy carbon	47
Figure 18: 300 second α deposition on glassy carbon 500 x mag.....	47
Figure 19: 10 second β deposition on glassy carbon	48
Figure 20: 30 second β deposition on glassy carbon	48
Figure 21: 60 second β deposition on glassy carbon	49
Figure 22: 300 second β deposition on glassy carbon 30K mag.....	49
Figure 23: 300 second β deposition on glassy carbon 5K mag.....	50

Figure 24: UV-Vis α as deposited.....	50
Figure 25: UV-Vis α annealed on FTO.....	51
Figure 26: UV-Vis β as-deposited on FTO.....	51
Figure 27: UV-Vis β annealed on FTO.....	51
Figure 28: XRD as-deposited α phase on glassy carbon.....	52
Figure 29: XRD α phase calcined 500° C on glassy carbon.....	52
Figure 30: As-deposited α phase on GC 30K mag.....	53
Figure 31: Calcined 500°C α phase GC.....	53
Figure 32: Circuit equivalent for as-deposited annealed α	54
Figure 33: Post 1 mA CCD testing of FTO samples.....	54
Figure 34: Circuit equivalent for exp.3.....	55
Figure 35: Mott-Schottky data for as deposited α phase.....	55
Figure 36: Mott-Schottky data for annealed α phase.....	56
Figure 37: CCD 0.1 mA as deposited α phase.....	56
Figure 38: CCD 0.1 mA annealed α phase.....	57
Figure 39: CCD 1 mA annealed α phase.....	57
Figure 40: XRD α annealed post-experiment.....	58
Figure 41: XRD as deposited β phase.....	58
Figure 42: XRD of annealed β phase.....	59
Figure 43: XRD as deposited β phase on glassy carbon.....	60
Figure 44: XRD annealed β phase on glassy carbon.....	60
Figure 45: XRD annealed β phase on glassy carbon.....	61
Figure 46: Circuit equivalent for as deposited and.....	61
Figure 47: Mott-Schottky for as deposited β phase.....	62

Figure 48: Mott-Schottky for annealed β phase.....	62
Figure 49: Auxetic Behavior.....	63
Figure 50: CCD 0.1 mA as deposited β phase.....	63
Figure 51: CCD 1 mA as deposited β phase.....	63
Figure 52: CCD 0.1 mA annealed β phase.....	64
Figure 53: CCD 1 mA annealed β phase.....	64
Figure 54: XRD post experiment as deposited β phase.....	65
Figure 55: XRD post experiment annealed β phase.....	65
Figure 56: Chrombismite solution from left to right.....	66
Figure 57: UV-Vis CB.....	66
Figure 58: XRD as deposited Chrombismite.....	67
Figure 59: XRD annealed Chrombismite.....	67
Figure 60: As deposited Chrombismite.....	68
Figure 61: Annealed Chrombismite.....	68
Figure 62: Mott-Schottky for as deposited Chrombismite.....	69
Figure 63: Mott-Schottky for annealed Chrombismite.....	69
Figure 64: CCD 0.1 mA for as deposited Chrombismite.....	70
Figure 65: CCD 1 mA for as deposited Chrombismite.....	70
Figure 66: CCD 0.1 mA for annealed Chrombismite.....	71
Figure 67: CCD 1 mA for annealed Chrombismite.....	71
Figure 68: XRD post 1 mA experiment as deposited Chrombismite.....	72
Figure 69: XRD post 1 mA experiment annealed Chrombismite.....	72
Figure 70: XRD of annealed β phase on ITO.....	73
Figure 71: SEM of as deposited α Bi_2O_3 on ITO substrate.....	73

Figure 72: SEM of annealed α Bi_2O_3 on ITO substrate	74
Figure 73: Circuit model for annealed α and β phase on ITO.....	74
Figure 74: Charge carrier density for annealed α and β	75
Figure 75: CCD of annealed α phase on ITO.....	75
Figure 76: CCD of annealed β phase on ITO.....	76
Figure 77: XRD of post CCD annealed β phase	76
Figure 78: SEM of Bi_2O_3 pressed into nickel foam	77
Figure 79: Equivalent Circuit for Bi_2O_3 Ni Foam.....	77
Figure 80: Mott-Schottky data for Bi_2O_3 Ni Foam composite.....	78
Figure 81: CCD for α phase Bi_2O_3 Ni Foam composite	78
Figure 82: CCD for β phase Bi_2O_3 Ni Foam composite	79

List of Tables

Table 5.1: EIS component values for α phase as deposited	13
Table 5.2: EIS component values for α phase annealed	14
Table 5.3: Charge Carrier Density for As Deposited α Phase	14
Table 5.4: Charge Carrier Density for Annealed α Phase.....	15
Table 5.5: Capacitance (Fg^{-1}) Values of α Phase As Deposited and Annealed	15
Table 5.6: EIS Circuit Component Values for As Deposited β Phase	16
Table 5.7: EIS Circuit Component Values for Annealed β Phase	18
Table 5.8: Charge Carrier Density of As Deposited β Phase.....	18
Table 5.9: Charge Carrier Density for Annealed β Phase.....	19
Table 5.10: Capacitance (Fg^{-1}) Values of β Phase As Deposited and Annealed	19
Table 5.11: EIS Circuit Component Values for As Deposited Chrombismite Phase	21
Table 5.12: EIS Circuit Component Values for Annealed Chrombismite Phase	22
Table 5.13: Charge Carrier Density of As Deposited Chrombismite Phase	23
Table 5.14: Charge Carrier Density for Annealed Chrombismite Phase.....	23
Table 5.15: Capacitance (Fg^{-1}) of As Deposited and Annealed Chrombismite.....	23
Table 5.16: Equivalent Circuit Component Values for Annealed α , β , and CD samples	24
Table 5.17: Capacitance (Fg^{-1}) Comparison of α , β , CB.....	25

Chapter 1: Introduction

Improving the capabilities of our current energy storage capabilities has been a continuing challenge in the modern world. Currently, lithium ion batteries are one of the better energy storage products that are out on the market with a specific power of 250-340 W/kg. However, to give enough energy for various technology to work such as electric vehicles (Tesla model S) requires 7,104 batteries. To fit this many cell into the Tesla, the base of the cars body is needed for space. With so many batteries required for the car to function an additional 1200 lbs. is added to the weight of the vehicle.

In other areas having enough capabilities to store excess power is a necessity regarding power plants such as solar and wind plants. During a full day giving optimum conditions, the average energy from the sun that reaches the surface of the earth comes to 5300 Watt-hours per meter squared [1]. The current top efficiency for photovoltaic cells that are used in solar power plants is 22.2% [2]. With a 1 m² panel, of the 5300 Watt-hour of solar energy, 1176.6 Watt-hours will be collected. With 25 acres for a solar farm 5 Megawatts of power can be generated, which is sufficient to power 1500 homes [2]. However, solar power plants only generate energy while the sun is out. At night they go dormant due to the lack of enough solar radiation. For this reason, any town powered by a solar farm will not have any power at night. In order to deal with this drawback, any excess energy produced during the day will need to be stored so that cities and towns can have continuous around the clock power provided. For example, a single house to make sure there is enough energy for night time use require at least 2 lead acid batteries to sustain them. If one solar farm powers 1500 houses, they would require 3,000 lead acid batteries. Finding the necessary real-estate for these batteries would not be an issue since most solar farms are on 25 acres minimum of land. The main issue would be disposing of that many lead acid batteries if they all fail around the same time.

Another renewable energy source that would require battery storage capabilities for down time hours are wind power plants. Wind turbines have a better efficiency than solar panels when it comes to converting the given source of energy to power needed for cities. They have an efficiency ranging from 30% to 40% on average. One of the drawbacks to wind farms is finding a location where there is as close to constant wind flow as possible. Generally, these areas are in remote locations far from towns and cities. This requires longer lengths of transmission lines to bring the power from far off resulting in an increase in funds needed to build a wind farm.

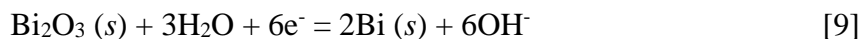
Additionally, even in these areas the wind does not flow at a constant rate or all the time. For these times when more energy is generated than is needed or during no wind down times, energy storage is going to be required to count for these moments. However, unlike solar farms where can build the storage under the complex, windmills must be spread far enough apart so the blades do not interfere with one another. This leads to needing to determine a different place to put the batteries besides beneath the windmills. To accomplish this a complex is created where the power flows through to reach the cities. In this complex there will be a bay for the batteries to be placed and can be charged and discharged as needed. Once again, the same thing will be required where 3000+ batteries will be needed for this. With lead acid batteries mentioned earlier let's take that as an example of an approximation of space needed. One type of lead acid battery has the dimensions of 13.411 cm X 6.71 cm X 5.99 cm, resulting in a total volume for one being 539.03 cm³. To fit a minimum of 3000 batteries a room would need to be built to hold a total of 1,617,090 cm³ worth of lead acid batteries.

There are other options that can be used besides lead acid batteries. In Appendix A, Figure 1, it compares cost, lifespan, and depth of discharge of 3 possible batteries. It associates lead acid, lithium-ion, and salt water batteries and compares them one to another. Lithium-ion batteries while being the most expensive has the best life span and a descent depth of discharge (how much it can be drained to keep optimum performance) is the best option for energy storage [3]. For a comparison of how many batteries would be needed for lithium-ion batteries a 50 kilo-watt Tesla uses approximately 7,000 18650 batteries. For a 5-Megawatt solar power plant a 100 x more lithium-ion batteries would be need for proper energy storage. That would require enough space to fit approximately 100 Tesla's. One Tesla has the dimensions of 497.84 cm x 195.58 cm x 6.52 cm which accounts to a volume of 6.35×10^5 cm³. Resulting in needing a structure that can house a total of 6.35×10^7 cm³ volume worth of 18650 lithium-ion batteries. To improve the efficiency of electric vehicles by decreasing its weight through decrease in battery quantity or reduce the necessary structure size for power energy storage, improving the energy density of batteries or using an alternative type of energy storage method will be important to achieving these goals. The goal for this thesis was to research and characterize the behaviors of bismuth sesquioxide energy storage capabilities on various substrates.

Chapter 2: Background

Supercapacitors have the charge/discharge rate of capacitors (1-10 seconds), while having specific power on the same order as batteries. Additionally, supercapacitors can be created as a thin film on various substrates to allow them to be used for various applications such as sensors, placed on car bodies, etc. Furthermore, desired design requirements are to have a charge and discharge time of less than 10 minutes, have a capacitance above 300 F (farads), which is on the same level of lithium-ion batteries, and be able to go through thousands of cycling states before energy storage efficiency begins to decrease [4]. Compared to normal capacitors where they store charge on the surface, supercapacitors are generally an electrode that has a porous surface that can hold more charge. Additionally, when two supercapacitor plates are put together instead of the usual dielectric material a very thin sheet of carbon for example is used. When a charge gets built up it results in an opposite charge being created on either side of the separator, creating a double-layer charge [5]. This can be seen in Appendix A, Figure 2. They were first commercialized by NEC who purchased their technology from SOHIO in 1971 [6]. One of the first oxides to be extensively researched was ruthenium oxide between 1975 and 1980. The highest level of capacitance that has been achieved for ruthenium oxide was 768 F/g [7]. However, ruthenium is an expensive material to work with. Currently, on the market to purchase a kilogram of ruthenium it would cost \$1286. In order to make supercapacitors more cost effective for industrial purposes, cheaper oxides have been investigated.

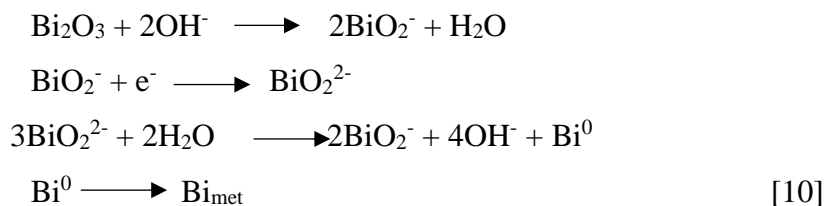
A good alternative to use is bismuth sesquioxide (Bi_2O_3). This can exist in 5 different polymorphs (phases). These are a monoclinic (α) phase that is stable at room temperature, tetragonal (β) phase, body center cubic (γ) phase, triclinic (ϵ) phase, and a face centered cubic (δ) phase which is stable between 700-800°C. Additionally, the cost to purchase a kilogram of bismuth is currently \$110, making it approximately ten times cheaper to use than ruthenium. Furthermore, Bi_2O_3 can obtain a theoretical capacitance of 1370 F/g [8]. During charging and discharging cycles Bi_2O_3 can be reduced to its metallic state and then back to its oxide state through the following reaction:



During the cathodic cycle a six-electron transfer process occurs causing Bi_2O_3 to go to its metallic state. As it starts heading back to anodic potentials the process reverses causing the metallic bismuth to return to an oxide state, which can be seen in Appendix A, Figure 3. Lee,

Changhyun, et. Al noticed that the changes in frequency seen in Figure 3B shows a mass decrease during cathodic scan due to oxide being reduced to metallic state. Between Figure 3 and 4 in Appendix A, it demonstrated how the amount of metallic Bi in Bi-Bi₂O₃ films can be tuned by controlling the anodic potential limit or oxidation time of the system [9].

In another paper by Wang, S.X., et. Al, researched Bi₂O₃ activated carbon composite reported another reaction process of Bi₂O₃ being reduced to bismuth metal. During cyclic voltammetry experiments at 5 mV/s in a 6 M KOH solution, for the most part should a typical rectangular shape. However, a pair of redox peaks were observed in the curves shown in Appendix A, Figure 5 [10]. A couple of potential possibilities that they note is it could be due to a catalytic induction, or oxidation of some untransformed Bi⁰ during reduction. The reaction occurs through the following process:



Where Bi⁰ is active atoms, Bi_{met} is metal bismuth. As Bi₂O₃ is converted into metallic bismuth only one stage involves a single electron is transferred and the rest is chemical reaction. This is different compared to the proposed mechanism by Lee, Changhyun et. Al, where it was a single step reaction involving the transfer of six electrons to go from Bi₂O₃ to bismuth metal.

Bismuth sesquioxide has several polymorph phases it can form, with the four main ones being a monoclinic α phase, tetragonal β phase, body center cubic γ phase, and a face center cubic δ phase. Li et al [11], reported electrodeposition of α Bi₂O₃ with grape like morphology using a galvanostatic condition (20 mAcm⁻²) in an electrolyte consisting of 0.1 M Bi(NO₃)₃, 3 M HCl and 0.04 M EDTA at room temperature. In another paper by Petrovic, et. Al [12], created an α phase structure showing trace amounts of β phase, rhombohedral Bi, and ω Bi₂O₃. By calcining the sample at 600° C for 90 minutes, resulted in a single α phase structure. In another paper by Switzer and his co-workers demonstrated electrodeposition of the cubic δ phase using alkaline solutions at 65° C [12, 13]. In another paper by Laurent et. Al [14], employed a similar procedure reported by Switzer, et. Al, using a different substrate to obtain δ phase coating under galvanostatic conditions in the range of 1 to 5 mAcm⁻².

On the other hand, Sarma et. Al [15], obtained monoclinic α phase deposit on to TiO_2 nanotubular substrate using alkaline Bi^{3+} solution with tartaric acid addition as complexing Agent. While Gujar et. Al [15], synthesized $\alpha \text{Bi}_2\text{O}_3$ onto a copper substrate in Bi^{3+} containing pH 12 solution under cyclic voltammetry between 0 and -1 V.

Chapter 3: Objective and Scope

Understanding the nucleation mechanics and behaviors of electrochemically deposited Bi_2O_3 will lead to improving deposition performance and creating desired phase. This paper will discuss the nucleation mechanics of both alpha and beta phase of bismuth oxide (Bi_2O_3). Alpha (monoclinic structure) and beta (tetragonal structure) phase will be deposited on glassy carbon to determine if alpha phase deposits differently from beta phase.

Energy storage capabilities of α and β phase Bi_2O_3 will be determined using EIS, Mott Schottky, and cyclic charge discharge (CCD) experiments. EIS and Mott Schottky was used to determine if its electrochemical properties change after going through charge and discharge cycles. Charge and discharge cycles were used to determine the materials cyclic stability, along with calculating its energy storage capabilities.

Chapter 4: Experimental Procedure

4.1 Materials and Preparation

Understanding the nucleation of Bi_2O_3 having a uniform surface to deposit onto was desirable. For this purpose, glassy carbon from (insert company) in 50mm X 50mm was used. Each plate was polished starting at 500 grit sandpaper up to 1500 grit followed by 1-micron polish solution. Afterward, they were cleaned by ultrasonicated in isopropyl alcohol, followed by acetone, then rinsed with DI water. FTO glass was ordered from Techinstro (New York City, NY) in 50mm X 50mm pieces and were cut down to 10mm X 50mm pieces. Each sample was ultra-sonicated in an isopropyl alcohol, followed by acetone then rinsed off in DI water. Afterward, each sample was pre-weighed before depositing Bi_2O_3 layer.

ITO glass was ordered from Adafruit (New York City, NY) in 50mm X 50mm pieces and were cut down to 10mm X 50mm pieces. They were then ultra-sonicated in an isopropyl alcohol bath, followed by being rinsed off in DI water. Nickel foam was purchased in rolls from MTI Corporation (Richmond, CA). Each nickel foam was cut in 10mm X 20mm pieces and cleaned in the same manner as the ITO glass. Afterward, each sample was pre-weighed before being coated with Bi_2O_3 .

Alpha phase solution consists of, 0.2 M of bismuth nitrate purchased from Sigma Aldrich (St. Louis, MO) mixed with 0.2 M tartaric acid powder. The powders were dissolved in 150 mL of water and stirred. While being mixed the bismuth nitrate partially dissolves due to the tartaric acid, forming $[\text{Bi}(\text{C}_4\text{H}_4\text{O}_6)(\text{C}_4\text{H}_5\text{O}_6)] \cdot \text{H}_2\text{O}$, resulting in a milky white solution [5]. Stirring the solution continuously, 1.8 M of NaOH was added to the mixture, creating bismuth hydroxide ($\text{Bi}(\text{OH})_2^+$), nitrates, and various other compounds. This allows for the remaining bismuth nitrate to go into solution, causing it to go from milky white to clear. For beta phase, once the solution went clear 0.04 M sodium dichromate hydrate was added to the solution and heated to 40° C.

4.2 Electrodeposition

Bi_2O_3 was electrochemically deposited onto glassy carbon using a Gamry potentiostat. α phase was created at room temperature, using platinum for the counter electrode and Ag/AgCl for the reference electrode. The Ag/AgCl electrode was created in house by filling a pipet with an Agar mixture made by heating 10 ml of saturated KCl solution to 80°C. Once it had reached desired temperature 0.5 g of Agar was added and mixed until it turned into a gel. This was then

drawn up into the pipets. A silver wire was anodized in a saturated KCl water mixture at 5 volts for 13 minutes. Saturated KCl was added to the Agar filled pipet and the anodized wire was placed in the pipet. Agar was used to behave as a frit allowing only ion transport to occur and not molecular transport. Cyclic Voltammetry was performed to determine the current density that would be needed for galvanostatic deposition. To reduce the amount of surface area exposed to solution the side of the glass that was coated with ITO, had an electrochemical tape covering the non-conductive side of the glass. Surface area of 1.35 cm^2 was used for the glassy carbon and FTO glass. Setup for α and β phase can be seen in Appendix A, Figure 1 and 2.

Using cyclic voltammetry graphs in Appendix A Figure 3 and Figure 4, show both α and β redox potentials. This was performed by changing the scan rate from 10 mV/sec up to 200 mV/sec. To create an α phase, a 150 mL solution was made using 0.2 M $\text{Bi}(\text{NO})_3$, 0.2 M $\text{C}_4\text{H}_6\text{O}_6$, 1.92 M NaOH. Once created a glassy carbon substrate was used as the working electrode, a platinum plate for a counter electrode, and an Ag/AgCl reference electrode. For beta phase, 0.05 M $\text{Na}_2\text{Cr}_2\text{O}_7$ was added to alpha solution once it had turned clear. This solution was then heated to a temperature of 40° C before experiments were performed.

Using glassy carbon as a substrate, nucleation behavior was determined. This was accomplished by using a galvanostatic process using a Gamry 1000 potentiostat. α phase was deposited at a current density of 7.885 mA/cm^2 with times that ranged from 10 seconds, 30 seconds, 60 seconds, 300 seconds, and lastly 1800 seconds. β phase was deposited at a current density of 7.885 mA/cm^2 , with same deposition times as α . Once completed, each sample was looked at using a Supra 3S VP LEO scanning electron microscope (SEM) to determine the nucleation that occurred on the substrate. Afterward, the 1800 second samples were placed in an x-ray diffractometer (XRD) to determine their crystalline structure. Once completed the samples were annealed at 500° C for α and 400° C for β to be characterized again to determine if there was any change in structure after annealing.

FTO glass was deposited on using the same current density as glassy carbon samples for 30 minutes to obtain a thick deposit. These specimens shown in Appendix A, Figure 5 had their electrochemical properties determined by using electrochemical impedance spectroscopy (EIS), Mott Schottky, Cyclic Charge Discharge (CCD), followed by EIS and Mott Schottky experiments on as-deposited samples in a 0.5 M NaOH solution. Afterward, α samples that were

annealed at a temperature of 500° C, 400° C for β , were characterized using the same techniques as the as-deposited specimens.

Using FTO samples, band gap of each phase was obtained. For experimental setup a Gamry UV-Vis was used. Before placing the sample into the cuvette, a dark spectrum and blank solution were collected. Once obtained for α phase a Bi_2O_3 solution was placed in the cuvette, followed by placing an Ag/AgCl reference electrode, platinum counter electrode, and FTO working electrode. Referring to a cyclic voltammetry graph shown in Appendix A, Figure 6 the potential for oxidation reaction was determined and used for a potentiostatic experiment. Using a potential of 1.08 V a 60 second deposition was performed, and a UV-Vis spectrum was collected during this time to later be used to determine the band gap for α phase which is shown in Appendix A, Figure 7. To determine β phase a coated FTO glass was placed in the cuvette to determine its band gap. Additionally, through β deposition process a chrombismite (CB) deposition was created and results were compared to α and β phase.

Bi_2O_3 was electrochemically deposited onto ITO glass using a Gamry potentiostat. Alpha phase was created at room temperature, using platinum for the counter electrode and Ag/AgCl for the reference electrode. The Ag/AgCl electrode was created in house by filling a plastic pipet with an Agar mixture made by heating 10 ml of saturated KCl solution to 80°C. Once it had reached desired temperature 0.5 g of Agar was added and mixed until it turned into a gel. This was then drawn up into the pipets. A silver wire was anodized in a saturated KCl water mixture at 5 volts for 13 minutes. Saturated KCl was added to the Agar filled pipet and the anodized wire was placed in the pipet. Agar was used to behave as a frit allowing only ion transport to occur and not molecular transport. Cyclic Voltammetry was performed to determine the current density that would be needed for galvanostatic deposition. To reduce the amount of surface area exposed to solution the side of the glass that was coated with ITO, had an electrochemical tape covering it as can be seen in Figure 1. A surface area of 1.35 cm² was used for the ITO glass, while the nickel foam had a different surface area used and was an approximation due to the varying size of pores in the foam.

Using the cyclic voltammetry graph indicated in Figure 1, a current of 0.71 mA was used, dividing the current value by 1.35 cm² from the surface area exposed to solution, resulted in a current density 0.5259 mA/cm². Galvanostatic was used at the calculated current density for 20 minutes before doubling the current density to 1.0518 mA/cm² for 40 minutes to achieve a

deposit onto the ITO glass. The solution was continuously stirred during deposition. Some of the samples were calcined at 380°C for 2 hours.

For beta phase, 0.05 M $\text{Na}_2\text{Cr}_2\text{O}_7$ was added to alpha solution when it had turned clear. Temperature was brought to 45° Celsius. A few of the samples were calcined at 400°C for 2 hours. After plating of the samples, x-ray diffraction (XRD) and scanning electron microscopy (SEM) were used to determine the crystal structure of the depositions. Afterward, charge-discharge cycles (CCD) and cyclic voltammetry (CV) were applied to determine cycle life and capacitance of the alpha and beta phases.

4. 3 Powder Coating of Nickel Foam

Alpha powder was made by mixing 10.45 g of $\text{Bi}(\text{NO}_3)_3$, 7.88 g citric acid, and 10.05 g NaOH. It was then diluted in 100 ml of DI water and continuously stirred for 2 hours. Afterward, the mixture was filtered, washed, and vacuum dried at 80°C overnight, the powder was then annealed at 380°C for 2 hours.

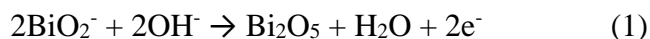
Beta powder was made by diluting 10.48 grams of $\text{Bi}(\text{NO}_3)_3$ in 115 ml 1M of HNO_3 . Once well mixed it was added dropwise into a 3.1:10 ratio solution of Na_2CO_3 :Water solution. It was stirred continuously for 2 hours, followed by filtering, washing with DI water and vacuum drying at 80°C over night. Once dried it was annealed at 400° C for 2 hours.

Once each powder was made, a slurry was created from combining 3 wt% poly vinyl fluoride (PVF) binder, 5 wt% carbon black, and Bi_2O_3 powder. To dissolve the binder into slurry N,N dimethylformamide was used. This slurry was then coated onto the Ni foam substrate and was first pressed at 35 MPa (5 tons) of pressure using a 3628 Bench-Press Spex Sample Press (7). This pressure fractured the Ni foam; therefore, the pressure was reduced to 3 tons, achieving the same result. When pressed the sample was dried at 100°C in a vacuum furnace overnight.

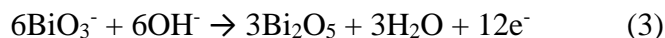
Chapter 5: Results and Discussion

5.1 Nucleation behavior of α and β phase

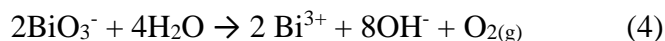
The Bi_2O_3 deposition was carried out under galvanostatic conditions, using highly alkaline solution with pH ~14. According to the E-pH diagram of the Bi- H_2O system [3!], bismuth exists as BiO_2^- at potentials within the water stability region and as BiO_3^- at potentials where oxygen evolution would occur. Figure 5 show the potentiometric V-t plots of the galvanostatic electrodeposition of α and β Bi_2O_3 coatings onto glassy carbon substrate. During initial periods of galvanostatic condition, the potential increased for the α phase deposition, reaching a maximum potential of 1.3 $V_{\text{Ag}/\text{AgCl}}$ at 3 seconds and decreased with the continuation of the constant current. The potential plateaued after 20 seconds of deposition at a value of 1.27 $V_{\text{Ag}/\text{AgCl}}$. In case of the β Bi_2O_3 deposition, which consisted of or both Bi^{3+} and Cr^{6+} species. In the as prepared solution, the deposition potential showed an irregular oscillating behavior during initial 50 seconds and decreased slowly before plateauing at a potential of 1.02 $V_{\text{Ag}/\text{AgCl}}$. It took about 150 seconds to reach steady state potential for the β Bi_2O_3 deposition. The maximum potential recorded was 1.16 $V_{\text{Ag}/\text{AgCl}}$. Laurent et al proposed the following reaction for the deposition of Bi_2O_3 :



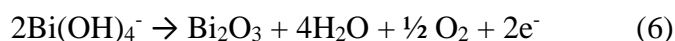
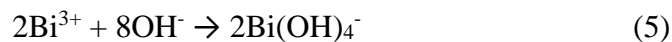
Under Galvanostatic condition, the recorded potentials were nobler than 1 $V_{\text{Ag}/\text{AgCl}}$. At these potentials, bismuthate species BiO_3^- could be present at the electrode/electrolyte interface. Therefore, the possible reaction of electrodeposition could be given by following reaction:



The Bi_2O_5 could decompose to Bi_2O_3 evolving oxygen. Recently Einkauf et. Al!, studied the stability of the BiO_3^- species in the aqueous solution and showed decreased stability when the acidity increased as a first order reaction



Other possible follow-up reactions could be:



When the electrodeposition is carried out under potentiostatic conditions, two types of nucleation and growth mechanisms are considered such as (i) instantaneous nucleation and (ii) progressive nucleation [21]. However, under galvanostatic conditions, non-steady state conditions lead to accumulation of adatoms at the instant of application of an anodic current, which results in increased overpotential [22].

Following the theoretical description of galvanostatic nucleation and growth proposed by Isaev and Grishenkova[23], the components of current during nucleation and growth of Bi_2O_3 could be described as:

Component 1: Charging of the electric double layer by the current:

$$i_d = C_d \frac{dE}{dt} \quad \text{equation 1}$$

Where C_d is double layer capacitance

dE/dt is the potential build up across double layer during time period dt

Component 2: Transportation of the anions across the electrode/electrolyte interface from the bulk of the solution to the positively polarized electrode surface. The current involved in this proces is given by the following relation as proposed by Aogaki and Makino [24]:

$$i_t = n * F \left(D_{ad} \frac{\partial C_{ad}}{\partial x, \partial y} + D_0 \frac{\partial C_{(x,y,z,t)}}{\partial z} \right) \quad \text{equation 2}$$

Where D_{ad} is diffusivity of adsorbed species such as hydroxyl and metabismuthate, ∂x , ∂y are surface coordinates, D_0 is diffusivity of species in the bulk electrolyte, ∂z is coordinate normal to the electrode surface.

Component 3: Current flow during the growth of bismuth oxide cluster could be given by the Butler-Volmer relation:

$$i_g = i_0 \left(e^{\frac{\beta F \eta}{RT}} - e^{\frac{-(1-\beta) \eta}{RT}} \right) \quad \text{equation 3}$$

Where β is transfer coefficient, η is overpotential for the reaction $\text{BiO}_3^- \rightarrow \text{Bi}_2\text{O}_5$, i_0 is the exchange current density for the oxidation of bismuthate to bismuth oxide. The applied constant current is the sum of the above three components:

$$i_{app} = i_d + i_t + i_g \quad \text{equation 4}$$

The variations in the potential during the galvanostatic deposition is associated with the charge and discharge of the double layer, adsorption and surface diffusion of adatoms or adsorbed species, and changes occurring on the surface area of the electrode due to evolution of different morphologies of the newly deposited material.

The potential increased during the initial period of galvanostatic deposition. The increase could be correlated with the increase in number of Bi_2O_3 clusters as observed from the SEM morphologies of the deposits depicted in Figure 8 and 9. The number of nucleated crystals increased during the initial 30 seconds. The recorded potential also increased during this period. No significant increase in the number density of nucleated crystals could be observed at 60 seconds as seen in Figure 10. The potential reached a plateau value indicating a steady state condition. During this time, the nucleated crystal started growing in size and no nucleation occurred. The α Bi_2O_3 showed more faceted or angular clusters while β phase showed more rounded clusters, as seen in Figure 13 and 15

5.2 Characterization of α phase

In Appendix A, Figure 5 shows the as-deposited with annealed samples on FTO glass. Before electrochemical experiments were conducted UV-Vis was used to determine the band gap of each phase. Converting UV-Vis counts to transmittance followed by using the log of $1/T$ absorbance was calculated. Using equation 2 to convert the wavelength into electron volts the band gap of Bi_2O_3 was determined.

$$E = h \cdot c / \lambda \quad \text{equation 5}$$

Where h is Planck's constant, c is the speed of light in meters per second, and λ is the wavelength. Once the electronvolt value has been calculated, it was plotted versus the square of absorption multiplied by electronvolt value. This produced the graph seen in Figure 18. Creating a linear line seen in Figure 18 and taking the value where it intersects with the X-axis the bandgap value of 2.36 eV for α phase as deposited was determined. This value corresponds close to the band gap of α phase Bi_2O_3 [9]. To determine if there was a difference in the band gap after the sample was annealed, UV-Vis was performed again after treatment. Referring to Figure 19 The band gap decreased slightly to 2.25 eV for the calcined sample. This is still within the range of what has been reported in literature for α phase.

X-ray diffraction (XRD) was performed on glassy carbon for as deposited samples and after annealed at 500°C for α phase. Upon initial deposition of α phase on glassy carbon

substrate the hue was golden in color of the deposition, while for β deposition was brown in color. To determine if they were crystalline upon deposition they were placed in an X-ray diffraction machine and ran through 2θ angles of 15° - 70° . Analysis of as deposited samples for α seen in Appendix A Figure 11 shows a few broad peaks where max intensity is seen at angles of 25° and 43.5° . With the peak being broad for α sample it is difficult to determine if this peak corresponds with the monoclinic phase or a cubic phase since both phases have XRD peaks between the angles of 19° and 28° . However, with the second peak being closer to an angle that is seen in a cubic structure that has a value 43.97 while the closest for monoclinic is 44.3° . From this it can be inferred that the α deposit semi-crystalline structure appears to be more of a cubic structure than monoclinic.

Another sample was annealed in a Thermolyne Thermo Scientific Box furnace for 2 hours at a temperature of 500° C. After XRD scan was done of annealed sample a noticeable difference can be seen when compared to the as-deposited scan. In Appendix A, Figure 23 instead of seeing a couple broad peaks shown in Figure 22, very sharp identifiable peaks can be seen. The strongest peaks showing up at angles of 27.6° , 33.4° , and 46.6° degrees. Along with these peaks and the others seen in the graph it compares to the monoclinic (α) phase (JCPD 98-001-8774). A single lone peak that is seen at a 2θ value of 38.05 arrives from the FTO substrate that it has been deposited on.

Once confirmed this was α phase, SEM was done on glassy carbon substrate to see how it differed from the 30 minute as-deposited specimen. Referring to Appendix A Figures 24 and 25, a difference can be seen between the two figures. In Figure 24 the structure for as deposited α phase appears to have a structure similar looking to that of coral. Upon close inspection, it can be seen that there are tiny nanospheres that are grouped together to make the larger structure that is seen. However, for the annealed sample when reviewed under the same magnification the structure has more of an amorphous appearance to it. The nanospheres have merged together to create a more uniform oblong structure compared to the coral look of as deposited structure. While the structure may not appear crystalline after being annealed, using XRD it was determined that it was in the proper crystal phase when associated to the as deposited structure that was only semi-crystalline.

After determining the physical characteristic difference between as-deposited and annealed α phase, the electrochemical behaviors were determined. This was done by running

EIS at open circuit potential, followed by mott-schottky that was done at varying frequency ranging from -1.1 V to 0.1 V. Afterward, the samples went through a CCD experiment until it charged to a voltage of -1.1 or 300 seconds was achieved at an amp rate of 0.1 mA. It was then discharged to either a voltage of 0.1 or after 300 seconds had passed. Once completed, another EIS was performed at a new OCP value followed by Mott Schottky. It was then post massed to determine the capacitance of the system for the 0.1 mA CCD experiment. Upon post massing, CCD was performed again but at an amp of 1 mA. This was done to see how well the various phases would hold up under more real world conditions. This was followed up with another EIS at new OCP, Mott-Schottky and then post massed once again.

From EIS experiments, equivalent circuits of each deposition was created for the three different experiments performed. Before the first CCD experiment was performed EIS was ran to have a baseline to compare after Bi_2O_3 had been discharged to determine if any change was seen in the model or circuit values. Circuit model for as deposited α phase and experiment 1 and 2 for annealed α can be seen in Appendix A, Figure 26. Table 1 shows the values for the components seen in Figure 26 for as deposited α phase.

Table 5.1: EIS component values for as deposited α phase

	R_p	R_u	Y_0	α	χ^2
Exp. 1	54200	95.38	1.4E-05	0.897	6.25E-04
Exp. 2	9700	87.71	3.45E-05	0.889	4.86E-04
Exp. 3	224400	67.9	2.35E-05	0.913	7.98E-04

When comparing Exp. 1 with Exp.2 it can be seen that the value R_p that is for the solution resistance decreased after CCD had been performed. Additionally, Y_0 value that is for capacitance increased after the material went through discharge cycles at 0.1 mA. This comes from the phenomena that as time passes the material has had time to get use to the accepting of the charge. This inturn results in the increase of the capacitance in the system. However, when compared to Exp. 3 there is a large increase in R_p and a bit of a drop in capacitance. Exp. 3 was the test after CCD had been done at an 1 mA. After the dishcharge cycling had completed, almost all of the Bi_2O_3 had fallen off of the substrate which can be seen in Figure 27. For this reason most of the values calculated for Exp. 3 are probably mostly from the FTO glass than

from the Bi_2O_3 . This is due to the Bi_2O_3 undergoing additional strain from the increase in current. Since the FTO is a rigid body, it does not allow for much flexibility as the structure changes to accept charge. Under the increased strain the Bi_2O_3 thin film will delaminate from the surface over time.

For the annealed α phase sample the same circuit diagram shown in Figure 26 is used for Exp.1 and Exp. 2. However, with Exp. 3 being done after the 1 mA discharge the circuit model for this run changed and can be seen in Appendix A, Figure 28. Table 2 shows the values for the circuit components for Exp.1 and Exp. 2 annealed α .

Table 5.2: EIS circuit component values for annealed α

	R_p	R_u	Y_0	α	χ^2
Exp. 1	8.24E+06	248	8.94E-06	0.968	1.77E-03
Exp. 2	8.94E+04	248	1.50E-05	0.943	1.94E-03

The values for Exp. 3 can be found in Table 16 along with Exp.3 for β annealed and CB annealed. When comparing the values for capacitance and resistance between as deposited and annealed a general trend can be seen. Between the two experiments the value for R_p decreased and the Y_0 value increased. It can be seen though that the Y_0 value was higher than annealed. This could be due to the fact that the as deposited sample might have a mixture of phases that can account for the increase of Y_0 value being higher. However, through the CCD experiments the annealed sample held up better than the as deposited sample. Being in the more stable monoclinic phase than the semi-crystalline phase it was able to handle a greater amount of current being placed on it.

Mott Schottky was used after EIS to understand how the charge carrier density changed after 0.1 mA and 1 mA CCD were completed. Keeping the frequency constant over a voltage range from -1.1 V to 0.1 V a graph shown in Appendix A, Figure 29 and 30 can be compiled and using the slope from the plot charge carrier density can be determined. Calculated values for as deposited α sample can be found in Table 3.

Table 5.3: Charge Carrier Density for as deposited α phase

	Exp. 1	Exp. 2	Exp. 3	Exp. 3-2
Slope	20587078178	7511545502	8733000918	10827923557
Carrier Density (cm⁻³)	1.49E+20	4.09E+20	3.51E+20	2.83E+20

After 0.1 mA CCD, charge carrier density increased from 1.49×10^{20} to 4.09×10^{20} cm⁻³. As the Bi₂O₃ goes through more cycles it becomes easier for the charge to move through out the material causing the increase between Exp.1 and Exp. 2. However, as mentioned in previous section after the 1 mA CCD most of the material had delaminated from the substrate, causing the reduction in charge carrier density.

When comparing the as deposited values to annealed α phase shown in Table 4, there is a decrease in the amount of carrier densities in the annealed α phase than in the as-deposited phase.

Table 5.4: Charge Carrier Density for annealed α phase

	Exp. 1	Exp. 2	Exp. 3	Exp. 3-2
Slope	1.58E+11	60812713098	67137699583	72575348952
Carrier Density (cm⁻³)	1.94E+19	5.05E+19	4.57E+19	4.23E+19

With the annealing of the sample, any surface defects that were created during deposition could have decreased, resulting in a decrease in charge carrier density [10]. When the sample is first deposited onto the substrate with it being in a semi-crystalline state, there are a fair amount more of broken bonds, voids, and other defects in the as deposited state. This will result in more available charge carriers but lower mobility. After the deposition is annealed some of the defects will be removed causing the carrier quantity to decrease.

Using CCD the capacitance and durability of each deposit was determined. During the charge cycle Bi₂O₃ will be reduced to its metallic state through a six electron transfer stage. Upon discharge it will loose the electron and convert back to the Bi₂O₃ state. After it went

through 10 cycles of charge/discharge, the discharge state was referred to and using equation 3 capacitance was calculated.

$$C = \frac{I*t}{V*m} \quad \text{equation 3}$$

Where I is current in amps, t is time in seconds, V is voltage, and m is weight in grams. Two separate CCD's were performed, one was done at a current of 0.1 mA and the second was done at 1 mA. This was done to determine if the material could withstand a higher current load before it began to degrade. Referring to Figures 31, 32, and 33, the CCD graphs can be seen for as deposited and annealed α phase. Using the change in voltage and how long it took for the system to discharge capacitance per gram (F/g) was calculated and can be seen in Table 5.

Table 5.5: Capacitance (F/g) values of α phase as deposited and annealed

	0.1 mA	1 mA
As Deposited	2.2	0
Annealed	318.04	622.04

For as deposited sample done at 1mA, when the first charge cycle started the load was too high for the sample and all the material delaminated. Due to this, no capacitance or graph were created for this process. One of the losses of energy during discharge cycle is due to it being dissipated by the material internal resistance. As time progressed in the 0.1 mA experiment, it can be seen that as the material went through more cycles the amount of time it took for to discharge increased. This is a result of the material over time getting used to accepting the charge. As a result the internal resistance decrease, allowing more of the energy to be properly discharged between the electrodes. When comparing the capacitance value between as deposited and annealed, there is a 150 times increase once it has been annealed. This is due to the material being in a pure crystalline phase, thus allowing for charge mobility to increase. With an increase in mobility, minimizing of defects and energy efficiency improving over time the annealed α phase is able to have a higher capacitance. Additionally, the durability for the annealed material improved. Since it was in a more stable form the 1 mA experiment was able to be performed. This resulted in a higher capacitance being seen. However, when referring to Figure 5 it can be seen that the annealed α deposit on the far right has some deposit remaining on the substrate, but most of the material could not hold up to the strain and had delaminated

from the surface. The material remaining on the surface had turned from the white of the α phase to a grey hue, which is indicative of the bismuth being in the metallic state. XRD was used to determine if it was still α Bi_2O_3 or if it had turned to the metallic state. Referring to Appendix A, Figure 34 it can be seen that the strongest peaks are of the FTO substrate, while the remaining bismuth deposition has turned into either the triclinic phase or hexagonal bismuth metal phase. From this it can be inferred that at a discharge rate of 1 mA that after every discharge cycle not all of the material converted back to Bi_2O_3 , instead stayed in the metallic state.

5.3 Characterization of β phase

UV-Vis was performed on as deposited and annealed β phase sample. Using equation 2 the electronvolt was determined to create the graph seen in Appendix A, Figure 20. Making a linear line to intersect the x-axis it was determined that the band gap for as deposited sample was 2.2 eV. To determine band gap of β annealed Figure 21 in Appendix A was used. The line intersected the x-axis at 2 eV. This value corresponds to the band gap that has been seen with an amorphous Bi_2O_3 structure [9]. In the paper by Leonite, L. et. Al the value they have given for β phase was approximately 3 eV. A potential reason for the difference between the two values is that Leonite, L. et Al experiments of β phase was not a pure β phase, but showed a mixture of BiO and $\text{Bi}_2\text{O}_{2.75}$ with the β phase. As to where the characterization of β phase on FTO through XRD shown in Appendix A, Figure 35 showed a more pure phase. The difference between their mixture of different phases and having a more pure phase β is enough to change the band gap from what was seen for the annealed β sample.

X-ray diffraction (XRD) was performed on glassy carbon on as deposited samples and after annealed at 400 ° C for 2 hours of β phase. As deposited β sample had a single noticeable peak at an angle of 27.8° and another less intense peak seen at an angle of 45.6° seen in Appendix A, Figure 36. After annealing of the sample XRD shows defined peaks that associate with the β tetragonal phase referred from JPCD 00-0559-0331. A few peaks can be seen at an angle of 26.6° that is associated with a triclinic phase and another defined peak at 38.05° that correspond with FTO substrate.

SEM was used to look at the structure of both as deposited and annealed β phase which can be seen in Appendix A, Figure 37, 38 and 39. As seen with α phase, after a long period of time nanospheres are created to form the main structure of the Bi_2O_3 deposition. After being

annealed as can be seen in Figure 40 and 41 they form a more amorphous looking structure with no real definable characterization to it. Even though on the nanoscale both α and β phase have the same physical appearance, from doing XRD analysis it can be seen that they are both different phases of Bi_2O_3 .

With physical characteristics determined, the electrochemical properties were analysed next. The same procedure was used to determine β phase assets as was done for α phase. EIS was performed to determine the circuit model for β phase, which can be seen in Appendix A, Figure 42. The values for the circuit components are displayed in Table 5.

Table 5.6: EIS circuit component values for as deposited β phase

	R_p	R_u	Y_0	α	χ^2
Exp. 1	2.42E+07	84.75	2.17E-05	0.823	3.88E-03
Exp. 2	9.60E+06	77.09	3.00E-05	0.903	8.40E-04
Exp. 3	4.90E+03	80.04	1.94E-04	0.839	1.16E-03

After the 0.1 mA CCD, the capacitance value increased while the R_p and R_u values decreased. As seen with as deposited α phase, after the material goes through initial discharge cycles the material has been allowed to get use to accepting charge into more of its structure causing for the capacitance to increase and a decrease in resistance. For Exp. 3 as can be seen in Figure 16 most of the deposition has delaminated from the surface. This resulted in a decrease in capacitance. Circuit component values for annealed β phase are in Table 6.

Table 5.7: EIS circuit component values for annealed β phase

	R_p	R_u	Y_0	α	χ^2
Exp. 1	2.38E+05	102.1	1.17E-05	0.964	8.85E-04
Exp. 2	2.90E+03	98.56	3.10E-05	0.924	7.54E-04

Exp. 1 and Exp. 2 followed the circuit model displayed in Figure 26. The annealed β phase showed a similar trend to the as deposited material, where the value for R_p decreased and Y_0 increased. When comparing the two values together the Y_0 value for Exp. 2 was only a little

higher for annealed than as – deposited. For circuit models the greatest difference between them was the R_p value was lower in annealed experiment compared to as deposited.

After EIS experiments, Mott Schottky was done to determine the charge carrier density of the as deposited and annealed β phase. Taking the slope of each line in the graphs shown in Appendix A, Figure 43 and 44 the charge carrier density for both samples were calculated. The data from each of these experiments are shown in Table 8 and 9, refer to Table 13 for Exp. 3 values.

Table 5.8: Charge carrier density for as deposited β phase

	Exp. 1	Exp. 2	Exp. 3
Slope	23690184090	13536767956	286769037.1
Carrier density (cm⁻³)	1.30E+20	2.27E+20	1.07E+22

Table 5.9: Charge carrier density for annealed β phase

	Exp. 1	Exp. 2	Exp. 3
Slope	3576035164	5450801341	19767436564
Carrier Density (cm⁻³)	8.58E+20	5.63E+20	1.55E+20

Between Exp.1 and Exp. 2 for β as deposited, the carrier density increased after CCD at 0.1 mA experiment. This potentially occurred due to the material under going initial strain from the constant current, resulting in more defects arising. The opposite is seen for annealed β phase. Additionally, there is a higher quantity of charge carriers than as deposited. With it being a tetragonal structure there are potentially more available oxygen ions throughout the material compared to as deposited creating the higher quantity of available carrier density. Furthermore, in the annealed sample the carrier density decreased potentially due to the auxetic nature of the material. β phase Bi_2O_3 differs from α phase by the fact that it has a negative poisson ratio, which means when it is put under tension instead of shrinking in the direction perpendicular to applied force it stretches which is demonstrated in Appendix A, Figure 45 [12]. With the

material able to adjust as it accepts more charge, it in turn potentially allows for mobility to increase which results in a decrease of charge carrier density.

To determine the capacitance of β phase and durability of material CCD experiments were accomplished at a current of 0.1 mA and 1 mA. This can be seen in Appendix A, Figure 46-49. The as deposited β phase sample at 0.1 mA showed a different trend compared to the as deposited α phase. Instead of the discharge cycle time increasing as it underwent more cycles, the amount of time that it took for it to fully charge decreased. By the tenth cycle it was fully charged in 82 seconds instead of 300 seconds. Under 1 mA condition the same result was seen in the graph however, about half way through the cycles the material started delaminating and by the end most of the material had fallen off. A potential reason for seeing the decrease in charging time is that as the cycling continued charge only built on the surface of the material instead of in the material. Since surface charge is quicker to build and dissipate than interior charge, the time needed for it to come to build a charge to the max voltage range occurred sooner than with α phase. The same phenomena was seen around the sixth cycle in the 1 mA experiment. However, for this test by the sixth cycle a portion of the material had delaminated which can be seen in Figure 16. Due to this the remaining CCD was based on both the FTO substrate and Bi_2O_3 .

For annealed β phase 0.1 mA experiment, as time progressed the amount of time it took for the material to discharge decreased from the initial cycle. Initially when the CCD first begins the material has yet to accept any charge yet and the structure has yet to undergo the auxetic behavior. As time continues more of the material has had force applied to it due to the incoming charge, resulting in more of the substance to have become deformed. With the Bi_2O_3 having undergone auxetic deformation, it allows for the charge to enter the material easier than in initial stages, in turn this results in the charge having an easier time to leave the system as well. This causes the material to discharge in less time. As it underwent the 1 mA experiment, the same phenomena started being seen as the as deposited 0.1 mA trial. Additionally, over time the material turned from its initial yellow color seen in Figure 5 to a metallic grey shown in Figure 16. One thing to be noted is that even after the 1 mA CCD most of the annealed β phase remained on the substrate unlike the previous samples. The fast charge and discharge can be a result of two factors, the first factor can be from as mentioned before that after the 0.1 mA CCD most of the material has undergone auxetic deformation. From this most of the charge was able

to get in and out of the material with relative ease. The second factor comes from most of the material staying in the metallic state as the cycles continued. The potential result of this is most of the charge stored came from surface charge than internal storage. Since it is mostly in the metallic state the oxygen that is the main component of charge regulation is not available to provide internal energy storage. The capacitance values for these experiments are shown in Table 10.

Table 5.10: Capacitance (F/g) of as deposited and annealed β phase

	0.1 mA	1 mA
As Deposited	35.94	967.54
Annealed	20.31	118.67

The capacitance value for 1 mA as to be expected is higher than 0.1 mA. This is from there being more internal storage available, due to it already undergoing the auxetic transformation from initial CCD. The anomaly is the high capacitance seen in the 1 mA as deposited sample. Since both FTO and the Bi_2O_3 was involved this would create a discrepancy in the charge storage. Potentially, this could come from FTO having good surface charge capabilities and coupled with the Bi_2O_3 pseudo capacitance capabilities, resulted in a higher than expected capacitance. Further research is required to determine the mechanisms behind this phenomena.

Post experiment XRD was done on annealed and as deposited β phase material. From the graphs shown in Appendix A, Figure 50 for as deposited phase that the remaining material has turned into the same phase structure as α phase as deposited. For annealed β phase sample most of the peaks in the graph correspond to metal bismuth with a hexagonal structure. At angle of 62.1° there is a small peak that corresponds to the β phase. It can be inferred that under the 1 mA CCD that there is not enough time for the phase switching from oxide to metal then back. The out come from this is if more cycles had been performed, the entire material would eventually be metallic bismuth.

5.4 Characterization of Chrombismite

Chrombismite (CB) was created using the same solution for β phase. It was then heated to 50°C where the solution turned from a clear vibrant yellow to a cloudy orange hue. This is

shown in Appendix A, Figure 51. Once in this state 30 minute galvanostatic experiment was completed on both FTO and glassy carbon. One of the samples was placed in the box furnace to be annealed for 2 hours at 400° C. Before electrochemical characterization was conducted, UV-Vis was done on the as deposited sample. Using equation 2 to determine electronvolts of the system and comparing it to α multiplied by energy for y-axis, a band gap of 1.93 eV was determined. This value corresponds with what has been seen in literature for amorphous structures which has been reported as ~2 eV [9].

Next XRD analysis was conducted to see the structure of the as deposited and annealed samples. These Figures can be seen in Appendix A, Figure 52 and 53. For as deposited sample the same thing was seen for previous as deposited sample, showing a semi crystalline phase with one peak corresponding to the FTO substrate. Using JCPD 00-037-0958 and 00-059-0331 for annealed CB that the XRD lined up with the proper structure having one peak belonging to the triclinic phase.

Following XRD, SEM images were taken of as deposited and annealed displayed in Appendix A, Figure 54 and 55. When comparing the as deposited image to the annealed sample, some of the nanospheres have coalesced together. These images line up with what has been seen with both α and β phase.

With physical characterization completed, the samples went through the same electrochemical procedure as α and β material. Using EIS the equivalent circuit model was determined for both as deposited and annealed. Figure 15 was the equivalent model for Exp.1 -Exp. 3 for as deposited and Exp. 1 and Exp. 2 for annealed sample. The component values for both of these are seen in Table 11 and 12.

Table 5.11: EIS equivalent circuit component values as deposited chrombismite

	R_p	R_u	Y_0	α	χ^2
Exp. 1	75.96 E3	76.83	2.10E-05	0.845	5.30E-03
Exp. 2	1.77E+03	89.44	4.19E-04	0.8	1.53E-03
Exp. 3	7.82E+03	72.93	3.47E-05	0.889	2.13E-03

Table 5.12: EIS equivalent circuit component values annealed chrombismite

	R_p	R_u	Y_0	α	χ^2
Exp. 1	1.16E+06	111	1.19E-05	0.957	1.77E-03
Exp. 2	4.27E+03	109.4	3.94E-05	0.889	1.94E-03

For as deposited sample, the R_p value increased after 0.1 mA CCD was performed and again after 1 mA. The Y_0 value decreased in Exp. 2 then was seen to raise more than Exp. 1. When compared to annealed sample the R_p value decreased by approximately 3 order of magnitude and the capacitance raised after CCD of 0.1 mA experiment.

Mott schottky data was analysed to determine the quantity of the charge carrier density for CB. The graph for this data can be found in Appendix A, Figure 45 and 46, while the values are displayed in Table 13 and 14 below.

Table 5.13: Charge carrier density values for as deposited chrombismite

	Exp. 1	Exp. 2	Exp. 3
Slope	97933904775	24916944462	24533069093
Carrier Density (cm⁻³)	3.13E+19	1.23E+20	1.25E+20

Table 5.14: Charge carrier density for annealed chrombismite

	Exp. 1	Exp. 2	Exp. 3	Exp. 3-2
Slope	4149016871	4845096318	9966327626	4124286769
Carrier Density (cm⁻³)	7.40E+20	6.33E+20	3.08E+20	7.44E+20

Using the slopes from each experiments that was determined from the graphs in Figure 56 and 57 charge carrier density was determined. In the as deposited sample the charge carrier density increased after 0.1 mA CCD and again once 1 mA was completed. As the as deposited sample went through discharge cycles the color started turning from the brown hue seen in Figure 5 on the far left to the grey hue seen in Figure 16. This color is associated with it turning into the metallic state of bismuth. Metals have a larger charge carrier than ceramics. Therefore,

as the CCD progresses with more of the material turning to the metallic state, the density will also increase. As for the annealed sample as it goes CCD for 0.1 mA to 1 mA the carrier density decreases from one experiment to the other. This follows the standard trend for the annealed samples. As time continues more of the material gets use to the acceptance of charge thus internal resistance decreases with each cycle pass. This will result in a decrease in charge carrier density.

Determining capacitance and durability of CB material CCD was accomplished at values of 0.1 mA and 1 mA. These graphs can be referred to in Appendix A, Figure 57-60. The CCD graphs for as deposited sample show a similar trend to as deposited β phase. As time progressed for the 0.1 mA experiment the material charges almost to max after a short time, then plateaus for the remainder of the 300 secs. A difference that was seen with the as deposited sample was its consistency. The discharge time after the first couple of cycles, the discharge time only decreased by one second for the next three cycles then stated at the same discharge time of approximately 190 seconds for the remainder of the time. Another interesting point is that the CCD performed at 1 mA is pretty close to charge and discharge times as the 0.1 mA procedure. Additionally, there was no material lose even after the 1 mA experiment. Even though it has not been annealed, the additionally amount of chromium in the deposit has made the able to handle a larger current load than the previous samples. After the sample was annealed, its ability to handle the charge was seen to have decreased. When comparing the graphs of annealed CB with annealed β phase they appear to have a similar charge and discharge behavior. As the cycles progress the time it takes to charge decreases. This is more prominent in the 1 mA CCD experiment. Since both β phase and annealed CB are a tetragonal structure, then the CB has the potential of also having auxetic behavior. Additionally, as seen in Figure 16 the annealed sample has mostly turned to the metallic grey hue with still some remnants of the original orange color associated with the CB structure. Furthermore, some of the deposit has delaminated from the substrate compared to the as deposited version. The capacitance values are seen in Table below.

Table 5.15: Capacitance (F/g) of as deposited and annealed Chrombismite

	0.1 mA	1 mA
As Deposited	36.26	361.37
Annealed	31.38	301.95

Comparing the capacitance values it can be seen that the capacitance value for the as deposited material is higher than the annealed version. For CB material having the sample annealed potentially had it in too rigid of a structure in comparison to the as deposited sample. This resulted in a decrease in its ability to handle the higher current load. Furthermore, with a higher percentage of chromium to oxygen it was able to handle the higher current load. However, once it was annealed the extra oxygen that got introduced resulted in the oxygen taking more of the charge load reducing its capacitance and durability.

XRD was used to determine the change in the crystal phase post 1 mA CCD. These figures can be referred to in Appendix A, Figures 61 and 62. After going through CCD experiment, the as deposited shows mostly a hexagonal structure with one peak that corresponds to α phase and another to β phase. While the annealed sample post analysis XRD shows only metallix hexagonal state and a corresponding β peak. With the outcome of the as deposited sample showing better stability and capacitance, it can be inferred that a mixture of phases shows better potential than a pure phase.

3.5 Comparison of α , β , and chrombismite

EIS for all annealed sample Exp. 3 showed a different circuit equivalent model compared to the as deposited samples. The circuit equivalent model is shown in Figure 17 and the component values displayed in Table below.

Table 16: Equivalent circuit component values for annealed α , β , and CD samples

	R_s	R_p	R_c	C_p	m	C_c	n	χ^2
α annealed	242	123.7	342.5	3.32E-04	1	1.92E-04	0.574	6.70E-05
β annealed	122.3	851.5	174.6	3.00E-04	0.708	8.25E-05	0.734	6.78E-05
CB annealed	103.3	783.3	0.00E+00	3.20E-04	8.52E-01	3.60E-05	8.02E-01	6.86E-05

Both α and β phase deposition material had delaminated from the substrate by the time Exp. 3 EIS was performed. It can be seen that the C_p and C_c value for β phase had a smaller

capacitance than α phase. The annealed β phase still had most of the material on it but was in the metallic bismuth phase. This provided it with less capacitance than the FTO/Bi₂O₃ mixture of the annealed α phase deposit. The CB deposit values for capacitance were lay between α and β phase. To determine which composition had the best results the capacitance values were compared one to another. These values can be seen in Table 17 below.

Table 17: Capacitance (F/g) comparison of α , β , CB

	0.1 mA	1 mA
α As Deposited	2.2	0
α Annealed	318.04	622.04
β As Deposited	35.94	967.54
β Annealed	20.31	118.67
CB As Deposited	36.26	361.37
CB Annealed	31.38	301.95

From the data displayed in Table 17, the material that showed the highest level of capacitance β as deposited sample, followed by α annealed, lastly CB as deposited. From referring to just the data in the table it would seem that the best material would be as deposited β . However, after only ten cycles most of the Bi₂O₃ had been delaminated from the surface, while α annealed had completely fallen off the substrate. Even though it does not have the highest capacitance it was seen to have the greatest durability.

5.6 Characterization of α and β phase on ITO

Before electrochemical were performed on the ITO substrate physical characterization was performed on the samples. Both as deposited and annealed sample of α and β had the same structure when seen under SEM. The as deposited sample had the same appearance as FTO deposition, where nanospheres can be made out that makes the structure as a whole. There is a noticeable difference can be seen after it was annealed. Both α and β phase appeared the same under SEM on ITO where the spheres had fused together similar to FTO. However, while the fused particles made more of a plate structure on FTO, on ITO a few conical structures can be seen on the substrate. This variance could be due to the different crystalline structure between FTO and ITO, where ITO has a cubic structure while FTO is tetragonal [10]. Both α and β had

the same color hue as the FTO samples. To confirm this XRD scans were performed on β sample. This graph can be referred to in Figure 65. The result was that the ITO spectrum matched up the β phase of FTO β annealed.

To better understand the effect of substrate on the electrochemical performance of bismuth sesquioxide, α and β phase were electrochemically deposited on ITO glass. Furthermore, FTO has a softening point around 650°C while ITO's is 525°C . Depending on the phase attempting to obtain of Bi_2O_3 , the ITO would be approaching its softening point by the time proper annealing temperatures are reached.

α and β phase on ITO glass electrochemical properties were determined using EIS, Mott Schottky, and CCD. Using EIS the equivalent circuit was determined for both α and β ITO, which can be seen in Figure 65. The circuit diagram for ITO shows a difference compared to FTO where it is an RLC circuit instead of an RC model. This circuit diagram relates to both before and after CCD experiment. The component values are in Table 18 and 19 below.

Table 5.18: Circuit component values pre CCD for α and β phase on ITO

	R_1	R_2	Y_0	L
α	246.1	3.33E+06	1.73E-05	4.10E+11
β	176.7	4.57E+06	2.92E+07	1.39E+12

Table 5.19: Circuit component values post CCD for α and β phase on ITO

	R_1	R_2	Y_0	L
α	185.6	2.79E+06	1.73E-05	4.10E+11
β	168.3	1.10E+07	2.92E-05	1.39E+12

After CCD the only values that changed from before CCD was the resistance values. R_1 decreased for both α and β , while R_2 lowered for α it increased for β . The increase in R_2 value was due to the β phase starting to delaminate partially from the surface of ITO.

Mott Schottky was performed to determine the charge carrier density for α and β phase. Taking the slope of each line from the plot seen in Figure 71, the charge carrier density was calculated and the values are shown in Table 20 below.

Table 5.20: Charge carrier density for annealed α and β phase on ITO

	Slope 1	Carrier Density (cm ⁻²)	Slope 2	Carrier Density (cm ⁻²)
Pre α	2252322607	1.36E+21	6082651223	5.30E+20
Post α	3080960485	9.97E+20	8201538014	3.74E+20
Pre β	3185008503	9.64E+20	12323714168	2.49E+20
Post β	2587807481	1.19E+21	5525336840	5.56E+20

As the potential changes it goes from an oxide region to where it gets reduced to the metallic state. This change results in two different slopes appearing in the graph. In both slopes for α phase the charge carrier density was seen to decrease after CCD. As the material becomes used to accepting charge with time, the internal resistance begins to drop increasing mobility. As a result the carrier density decreases. β phase had the opposite result occur, where it had a lower initial charge carrier density. After CCD, the charge carrier density increased. Unlike with the FTO deposition the β phase did not turn into the metallic grey hue of metallic bismuth. Instead by the end of the charge discharge cycles part of it had started to turn the white color of the monoclinic structure. When comparing the pre CCD charge carrier density for slope 1 the quantity for post β phase is similar to that of the α carrier density. The second slope has only a slight increase in comparison. This carrier density difference comes from the mixture of phases of α and β .

Determining the durability and capacitance of the samples CCD was performed at a current load of 0.1 mA, lasting 300 seconds, 5 cycles, between the voltage range of -1 to 0 V. Referring to Figure 75 for α phase, from one cycle to the next they are relatively consistent. As the cycles continued the time it took for the material to discharge increased. The longer the cycles go the more material that gets involved in the storage of energy, resulting in an increase in discharge time. Additionally, the internal resistance decreases seen from the circuit models,

resulting in more energy being used for electrochemical process than being lost through dispersion in the structure. For β phase it showed a quicker discharge time compared to α phase. Referring to Figure 76 it can be seen that the discharge time while showing some increase over time was relatively short in its duration. This could be due to the energy that was lost while it was changing phases on top of material loss during the CCD. A possibility as to the difference in durability between α and β phase is that the tetragonal structure of β phase has a higher mismatch energy than the cubic structure than the α phase. The α phase ended up having a higher capacitance than β phase, where α was 23.853 Fg^{-1} and β was 9.6996 Fg^{-1} .

With the β phase showing the most change during CCD testing, it was analysed using XRD to determine if the crystal structure had changed. Referring to Figure 77 a peak corresponding to the α phase appears, along with this the β crystal direction (0 0 2) disappears while the (2 1 3) directions arrives. A cause for the phase change on ITO is naturally it is the most stable at room temperature. Additionally, for the ITO substrate it the α phase is more stable. This results in the β phase converting into the α phase due to it being the more energy favorable state.

5.7 Characterization of α and β phase on nickel foam

Creating α and β phase powders, it was mixed with PVF binder and carbon black, then pressed at 35 MPa into a nickel foam substrate. Before any electrochemical experiments were performed SEM was used to analyze the composite material. Powder α and β phase had the same appearance under SEM which can be seen in Figure 78. The powder had a more distinct crystal morphology appearance compared to the deposition on the glassy carbon, FTO, and ITO substrates. The black regions in the sample are from the carbon black that was mixed in the slurry. Carbon black is needed to improve the conductivity of the powder mixture.

Once physical characteristics had been determined, EIS was used to determine the circuit equivalance model for the Bi_2O_3 composite. The circuit model for this can be seen in Figure 79, while the circuit component values can be seen in Table 21 and 22 below.

Table 5.21: Circuit component values for pre CCD Bi_2O_3 Ni Foam composite

	Rs	Rc	Rp	Cc	Cp	L
α	1.972	396.1	1.46E+04	9.64E-05	2.22E-04	9.52E-03
β	1.88	617.6	1.63E+04	1.40E-04	2.58E-04	1.28E-03

Table 5.22: Circuit component values for post CCD Bi₂O₃ Ni Foam composite

	Rs	Rc	Rp	Cc	Cp	L
α	2.075	371.8	4.79E+04	1.29E-04	3.06E-04	9.07E-04
β	2.406	402.7	4.47E+04	1.31E-04	3.28E-04	6.33E-04

The R_s values increased after CCD, while the R_c values decreased for both α and β phase. Furthermore, C_c and C_p values increased for α while inductance decreased. For β phase C_c and inductance decreased, in turn C_p increased. Improvement in α composite was brought on by the material getting use to accepting charge as the cycles continued. Whereas, β composite value change are due to it initially changing phases and eventually it was seen flaking from the substrate. There was still β material left in the nickel foam, however, by the end of the cycles a fair amount had degraded that the component value readings were potentially more from the nickel foam than the material.

Mott Schottky was used to determine the charge carrier density for Bi₂O₃ composite. Using the graph shown in Figure 80 the slope was determined and used to calculate the charge carrier density shown in Table 23 below.

Table 5.23: Charge carrier density for α and β Bi₂O₃ Ni Foam composite

	Slope 1	Carrier Density (cm⁻³)	Slope 2	Carrier Density (cm⁻³)
pre α	1355121	2.26585E+24	816193.8	3.76197E+24
post α	1059970	2.89678E+24	1016075.5	3.02192E+24
pre β	802598.9	3.82569E+24	582117.67	5.2747E+24
post β	3246950	9.45656E+23	1058109.4	2.90187E+24

The charge carrier density for α phase for slope 1 was seen to increase in the amount of charge carrier density while slope 2 decreased. Slope 1 is taken during the potential window for reduction to metallic bismuth. After charge discharge cycling some of the material was converted to the metallic state. Metals have a higher charge carrier density than ceramics causing the density to increase. Slope 2 is taken during the potential window for where the metallic state should be converting back to the oxide state. The decrease in charge carrier density after CCD is due to the material internal resistance decreasing. This results in a decrease in charge carrier density. For β composite the charge carrier density decreased for both slopes. During the CCD cycles the material was seen to go from the yellow hue of β

phase to the grey hue of metallic bismuth. Additionally, the Bi_2O_3 began to degrade from the substrate and mostly carbon black could be seen after CCD experiments. With a reduction in Bi_2O_3 on the substrate resulting in a decrease of charge carrier density.

Capacitance and durability of the material were determined using CCD method. For α phase composite the discharge time was only 42 seconds as seen in Figure 82, showing that it had a relatively low efficiency. However, even though the discharge time did not increase over time it also stayed consistent. Referring to Figure 83, β phase composite initially showed good promise with its charge and discharge state. In the first couple of cycles the 300 second window passed, and the material still had not completely discharged, showing 100 % efficiency for this time. However, as the cycles continued the discharge time became shorter and shorter, eventually discharging completely before 300 seconds had been completed. It could be seen that as time went on the Bi_2O_3 changed phases and eventually degraded from the material. The resulting capacitance for α phase was relatively low at a value of 0.8342 Fg^{-1} . β phase had a much higher capacitance at a value of 56.261 Fg^{-1} , however its inability to maintain the efficiency even after going through five cycles would need to be addressed in future experiments to find a way to improve longevity of the material.

5.8 Comparison of FTO, ITO and Nickel Foam Substrate

Various substrates have been used to determine if the material Bi_2O_3 is deposited on to affect the capacitance and durability. The capacitance values for each material is shown in Table 24 below.

Table 5.24: Capacitance (Fg^{-1}) comparison of substrates under 0.1 mA and 1mA conditions

	0.1 mA	1 mA
As Deposited α FTO	2.2	0
Annealed α FTO	318.04	622.04
Annealed α ITO	23.853	0
Powder α Ni Foam	0.834	0
As Deposited β FTO	35.94	967.544
Annealed β FTO	20.31	118.67
Annealed β ITO	9.6996	0
Powder β Ni Foam	56.261	0
As deposited CB FTO	36.26	361.37
Annealed CB FTO	31.38	301.95

From the data provided in the table the one with the best capacitance was as deposited β on FTO under 1 mA condition, followed by annealed α on FTO, then as deposited CB on FTO. Additionally, for stability of material the Bi_2O_3 deposited on FTO had the best results when it came to last the charge discharge cycles. While ITO had descent capacitance, most of the material delaminated from the surface after undergoing 0.1 mA experiments. For that reason, no CCD was performed on ITO samples at 1 mA. The same out come was seen with the Bi_2O_3 Ni Foam composite.

Chapter 6: Conclusions and Future Work

During nucleation of Bi_2O_3 on glassy carbon substrate it can be seen in the galvanostatic process that the voltage reached steady state. During this time the bismuth no longer nucleated on the surface, and the material already nucleated on started to grow. The α Bi_2O_3 showed more faceted or angular clusters while β phase showed more rounded clusters.

Experimental results indicated that the amorphous Bi_2O_3 structure had higher charge storage capacity than crystalline phases, however, the cyclic stability was inferior. For both capacity and stability, the tetragonal Bi_2O_3 stabilized by Cr incorporation (chrombismite) showed promising results having an energy storage capability of 361 Fg^{-1} for as deposited sample and annealed is 301.95 Fg^{-1} . Additionally, it showed the greatest stability maintaining its structure on the substrate after 20 cycles.










Further experiments will be performed on the chrombismite structure to determine its cycle life and energy storage capability. Furthermore, improving stability of α and β phase to be able to withstand higher current loads and better cycle performance will be further investigated.

References

1. Johnson, C. "Solar Energy – How Much Energy comes From the Sun." *Solar Energy- How Much Energy Comes From the Sun*, 14 Jan. 2019, mb-soft.com/public2/energyso.html
2. Docekalova, Praethip. "Are Solar Energy Farms the Answer to Renewable Energy?" *Open Access Government*, 11 Jan. 2019, www.openaccessgovernment.org/solar-energy-farms/56768/
3. "How to Choose the Best Battery for a Solar Energy System." *EnergySage*, 8 Mar. 2019, www.energysage.com/solar/solar-energy-storage/what-are-the-best-batteries-for-solar-panels
4. Capacitor Guide, (2018). Supercapacitors [Web log post]. Retrieved April 01, 2018 from <http://www.capacitorguide.com/supercapacitor/>
5. Gujar, T.P., et. Al, *Electrosynthesis of Bi₂O₃ Thin Films and Their Use in Electrochemical Supercapacitors*, pg. 1479-1485, Journal of Power Sources Elsevier, 2006
6. Lokhande, C.D., et. Al, *Metal Oxide Thin Film Based Supercapacitors*, pg. 255-270, Current Applied Physics, 2011
7. Bohannan, Eric, et. Al, *Low-temperature Electrodeposition of the High-temperature Cubic Polymorph of Bismuth (III) Oxide*, pg. 97-107, Solid State Ionics Elsevier, 1999
8. Fischer, Anne, et. Al, *Incorporation of Homogenous, Nanoscale MnO₂, within Ultra porous carbon...*, pg. 281-286, American Chemical Society, 2007
9. Pang, Suh-Cem, et. Al, *Novel Electrode Materials for Thin-Film Ultracapacitors...*, pg. 444-450, Electrochemical Society, 2000
10. Yuan Guohui, et. Al, *Oxygen-Deficient Bismuth Oxide/Graphene of Ultrahigh Capacitance...*, pg. 1-9, 2017
11. Wang, Joseph, et. Al, *Insights into the Anodic Stripping Voltammetric Behavior of Bismuth Film...*, pg. 29-34, Analytic Chimica Acta, 2001
12. Hutton, Emily, et. Al, *An Introduction to Bismuth Film Electrode for use Cathodic*, pg. 707-711, Electrochemistry Communications, 2001
13. Vytras, Karel, et. Al, *Novelty in Potentiometric Stripping Analysis: Total Replacement...*, pg. 19-20, Electroanalysis, 2002
14. Krolicka, Agnieszka, et. Al, *Bismuth-Film-Plated Carbon Paste Electrodes*, pg. 193-196, Electrochemistry Communications, 2002
15. Kruusma, Jaanus, et. Al, *Mercury-Free Sono-Electroanalytical Detection of Lead in Human*, pg. 700-706, Analytical and Bioanalytical Chemistry, 2004
16. Ziegler, John, et. Al, *Status of Reversible Electrodeposition Electrochromic Devices*, pg. 477-493, Solar Energy Materials and Solar Cells, 1999
17. Cordoba De Torresi, S.I., et. Al, *Optical Characterization of Bismuth Reversible Electrodeposition*, pg. 11-16, Journal of Electroanalytical Chemistry, 1996
18. Jeffrey, Craig, et Al., *In Situ Scanning Tunneling Microscopy of Bismuth Electrodeposition on...*, pg. L367-L372, Surface Science 2002
19. Pourbaix, M., *Atlas of Electrochemical Equilibria in Aqueous Solution*, 2nd Ed., N.A.C.E, Houston, USA, 1974
20. Laurent, K., et. Al, *Structure and Conductivity Studies of Electrodeposited δ Bi₂O₃*, pg. 1735-1739, Solid State Ionics, 2008
21. Einkauf, J.D., et. Al, *Solubility and Complexation of the Bismuthate Ion in Nitric Acid Systems*, pg. 15341-15349, Inorganic Chemistry, 2018

22. Milchev, A, et. Al, *Two-Dimensional Progressive and Instantaneous Nucleation with overlap...*, pg. 2399-2403, *Electrochimica Acta*, 2011
23. Gamburg, Yu, *Some Novel Efforts to Describe the Nucleation and Growth at Electrodeposition*, pg. 353-359, *Journal of Solid State Electrochemistry*, 2013
24. Isaev, Vladimir, et. Al, *Galvanostatic Nucleation and Growth Under Diffusion control*, pg. 1505-1508, *Journal of Solid State Electrochemistry*, 2013
25. Isaev, Vladimir, et. Al, *Galvanostatic Phase formation*, pg. 2383-2386, *Journal of Solid State Electrochemistry*, 2014
26. Isaev, Vladimir, et. Al, *Galvanostatic Nucleation and Growth Under Diffusion control*, pg. 1505-1508, *Journal of Solid State Electrochemistry*, 2013
27. Evseenko, V.I, et Al, *Synthesis of High-Purity Bismuth (III) Tartratahydrotartrate Trihydrate*, Institute of Solid State Chemistry Siberian Branch Russian Academy of Science, 2003
28. Lee, Changhyun, et. Al, *Preparation of Au-Bi₂O₃ Nanocomposite by Anodic Electrodeposition Combined with Galvanic Replacement*, pg. D499-D503, *Journal of The Electrochemical Society*, 2014
29. Leontie, L., et. Al, *Structural and Optical Characteristics of Bismuth Oxide Thin Films*, *Surface Science*, pg. 507-510, 2002
30. Kim, Dong-Ho, et. Al, *Structure and Electrical Transport Properties of Bismuth Thin Films....*”, *Applied Surface Science*, pg. 3525-3531, 2006
31. Gualous, H., et Al., *Experimental Study of Supercapacitor Serial Resistance and Capacitance Variations with Temperature*, *Journal Power Sources*, pg. 86-93, 2003
32. Saadatmand, Sanaz, et Al., *Auxetic Materials, Materials with Negative Poisson's Ratio*, *Material Science and Engineering International Journal*, pg. 1-3, 2017

Appendix A:

Battery	Cost	Lifespan	Depth of Discharge
Lead Acid			
Lithium			
Saltwater			

© EnergySage

Figure 1: Comparison of three energy storage options [3]

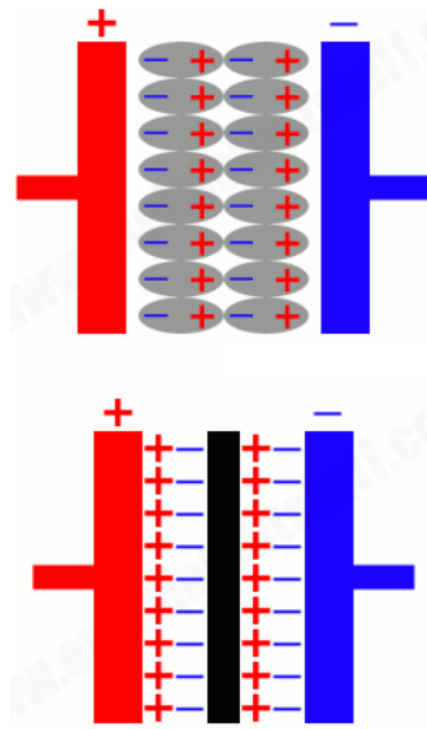


Figure 2: Capacitor Vs. Super-Capacitor [5]

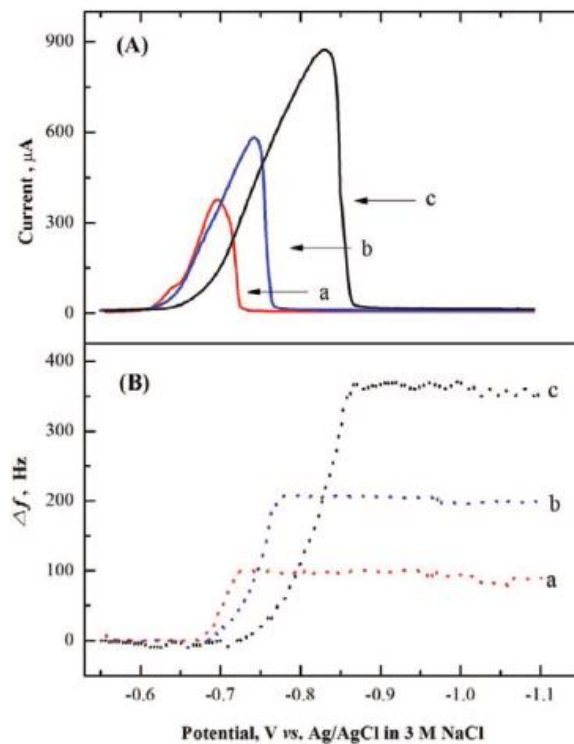


Figure 3: (A) Linear sweep voltammograms and (B) corresponding frequency changes for a Bi_2O_3 film on Pt in 0.1 M NaOH. Bi_2O_3 film was prepared by anodic oxidation of Bi foil in 0.1 M NaOH at 0.1 V for (a) 1 s, (b) 60 s, and (c) 100 s [9]

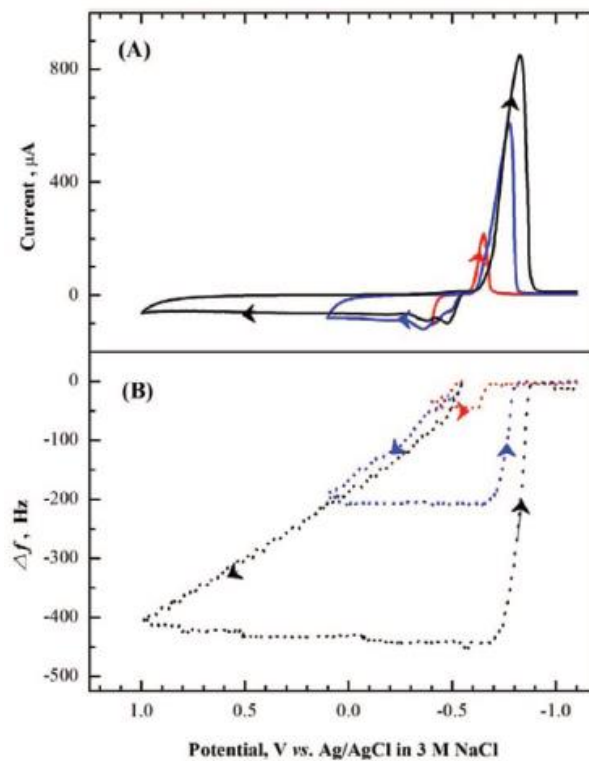


Figure 4: (A) Cyclic voltammograms and (B) corresponding frequency changes for electrodeposited Bi layer on Pt electrode in 0.1 M NaOH [9].

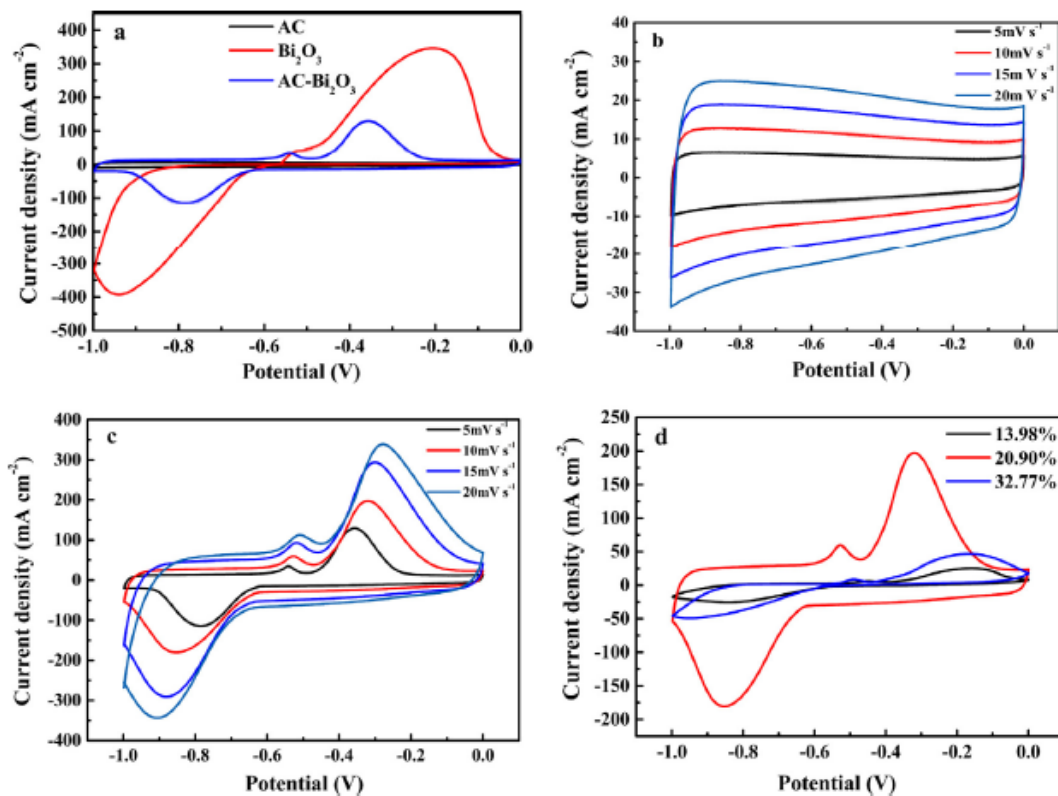


Figure 5: Cyclic Voltammetry curves: (A) CV of AC, Bi_2O_3 and AC- Bi_2O_3 ; (B) CVs of AC different sweep rates; (C) CVs of AC- Bi_2O_3 at different sweep rates; (d) CVs different content AC- Bi_2O_3 composite [10]

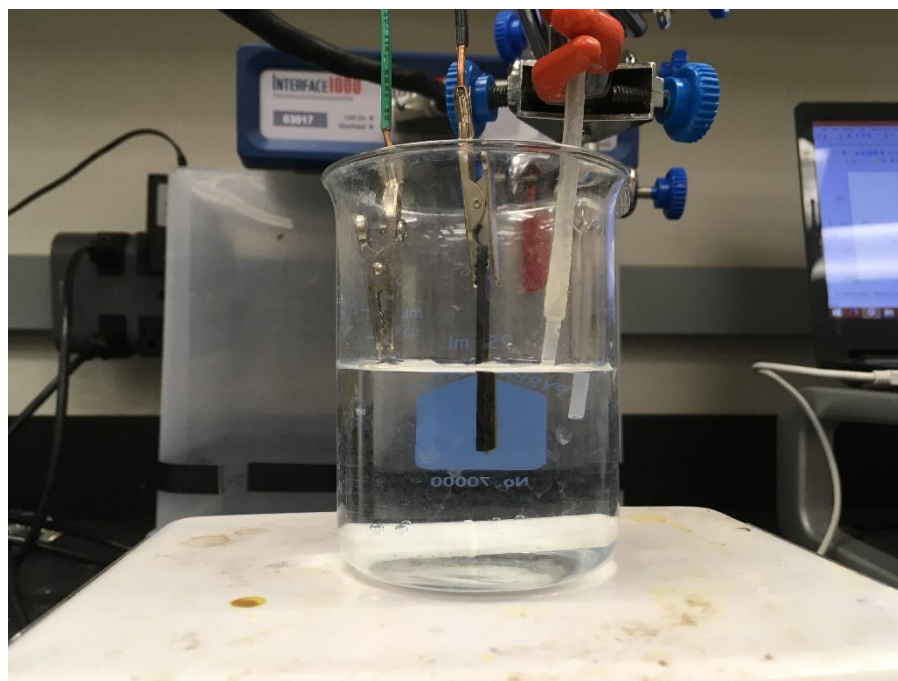


Figure 6: α phase solution from left to right: Platinum Counter Electrode, Glassy Carbon Working Electrode, Ag/AgCl Reference Electrode

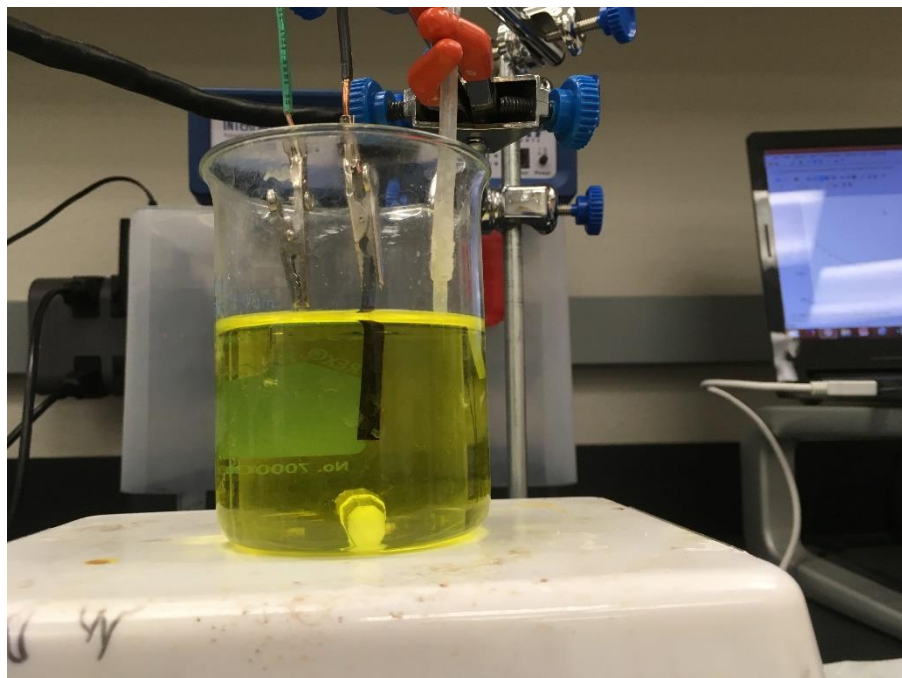


Figure 7: β phase solution from left to right: Platinum Counter Electrode, Glassy Carbon Working Electrode, Ag/AgCl Reference Electrode

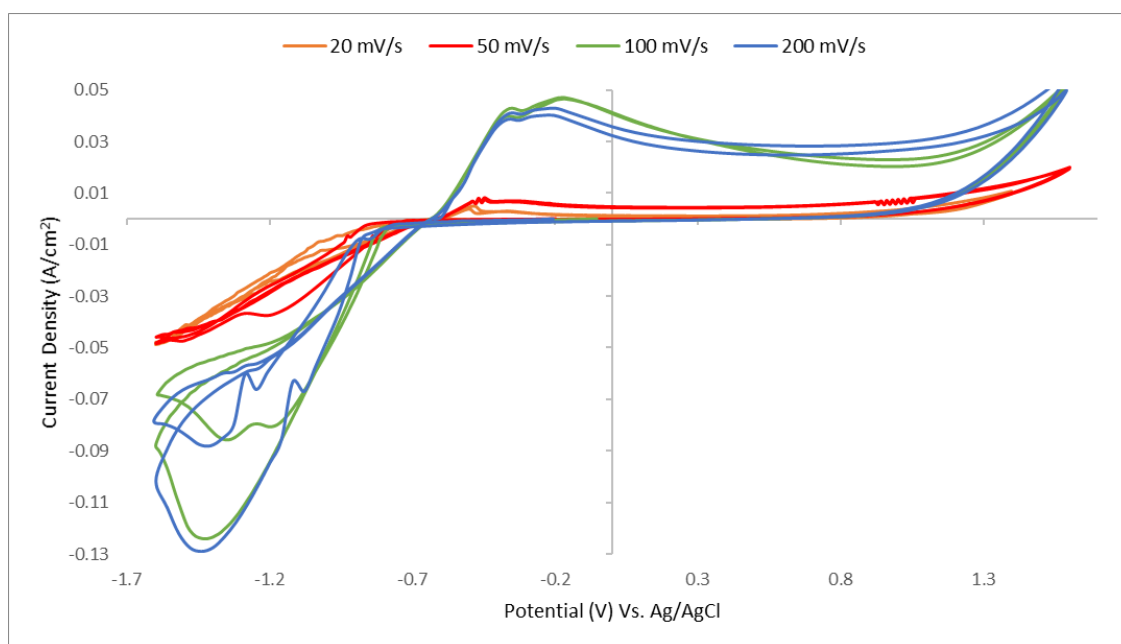


Figure 8: Cyclic Voltammery α phase varying scan rate comparison

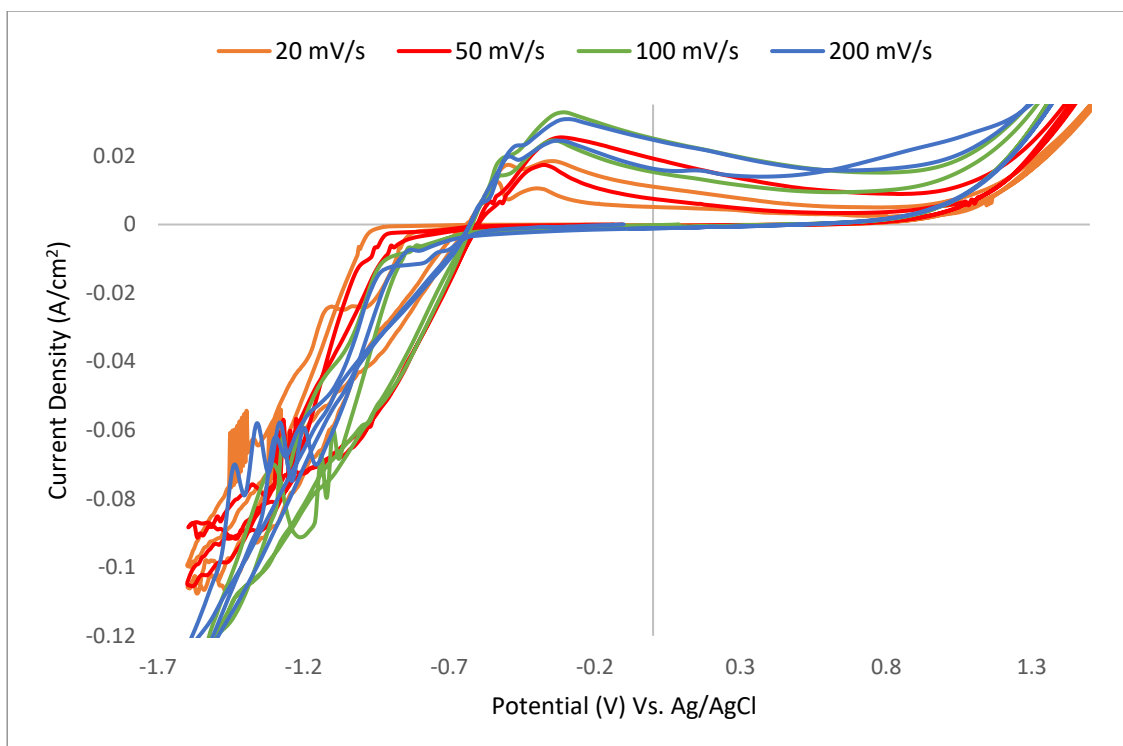


Figure 9: Cyclic Voltammetry β phase varying scan rate comparison

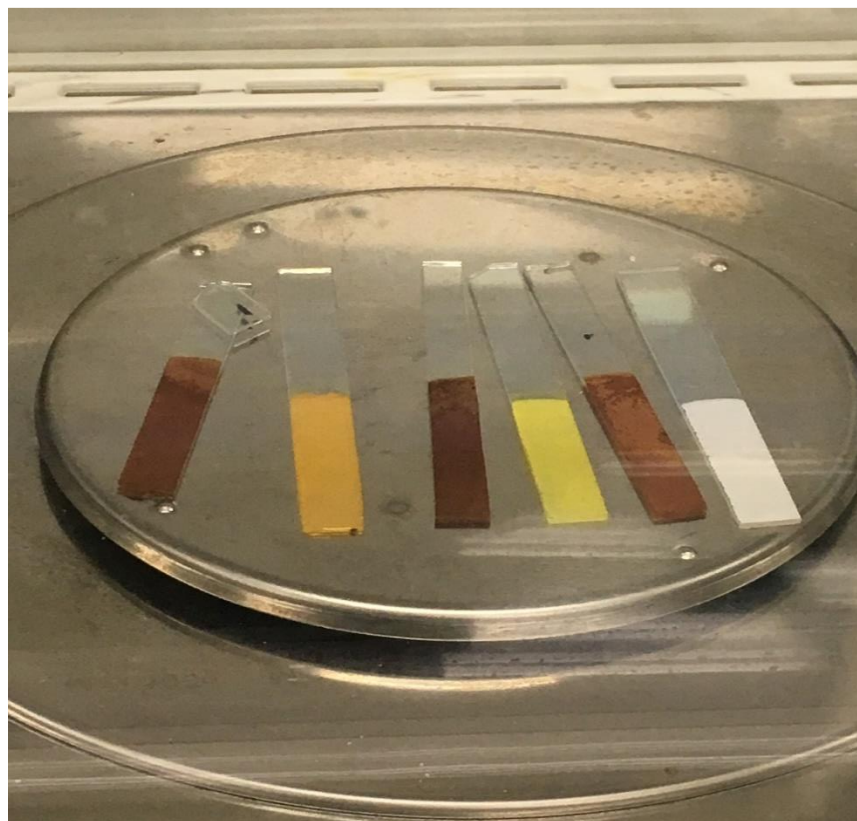


Figure 10: FTO glass deposition from left to right: As-deposited Chrombismite, Annealed Chrombismite, As-deposited β phase, Annealed β phase, As-deposited α phase, Annealed α phase

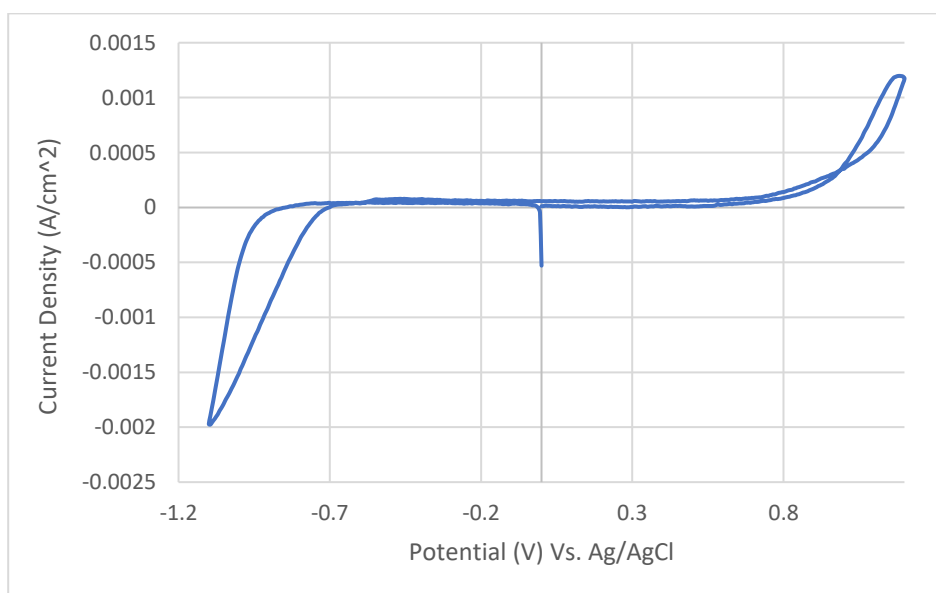


Figure 11: α phase deposit on FTO glass Cyclic voltammetry

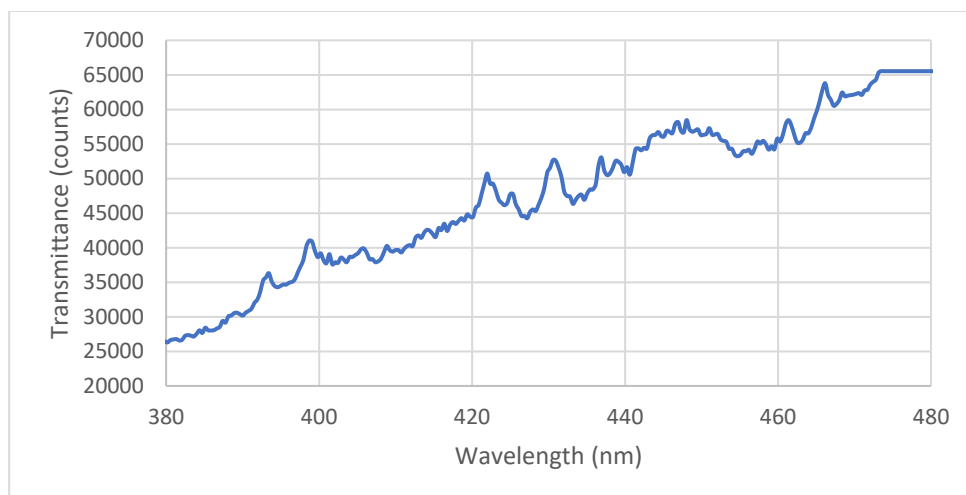


Figure 12: UV-Vis spectrum of alpha phase during potentiostatic experiment at 1.08 V

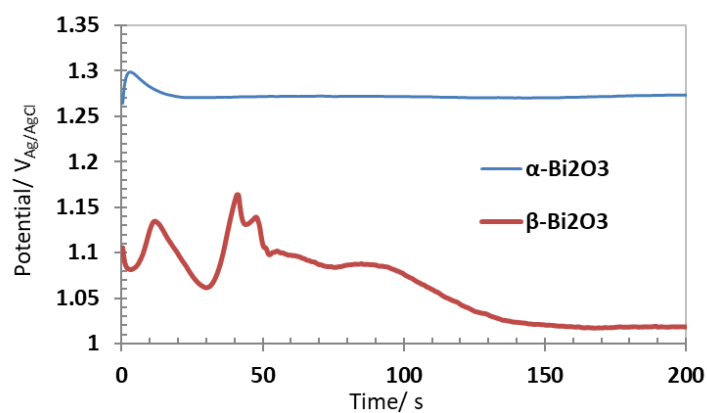


Figure 13: potentiometric V-t plots of galvanostatic electrodeposition of α and β Bi_2O_3 coatings onto glassy carbon

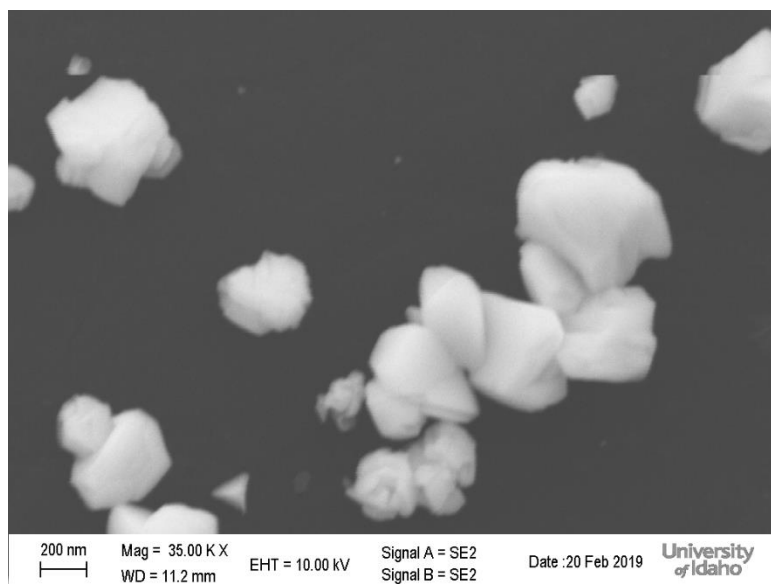


Figure 14: 10 second α deposition on glassy carbon

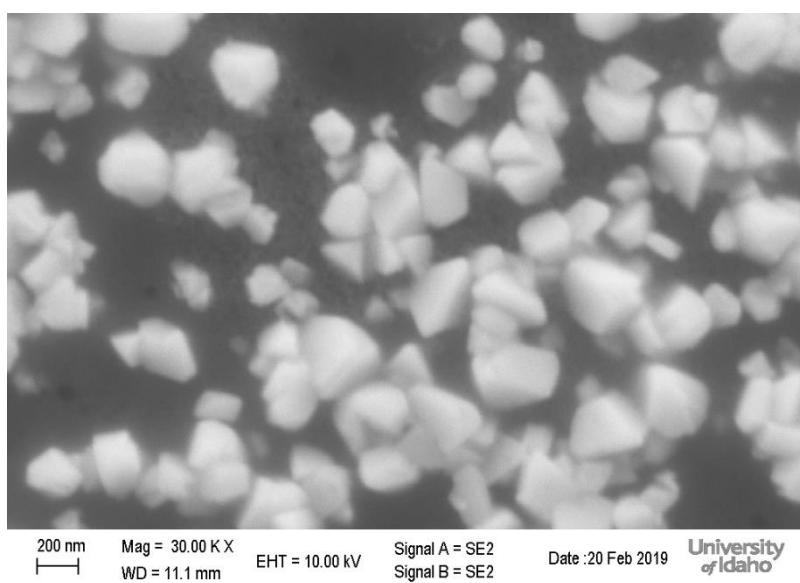


Figure 15: 30 second α deposition on glassy carbon

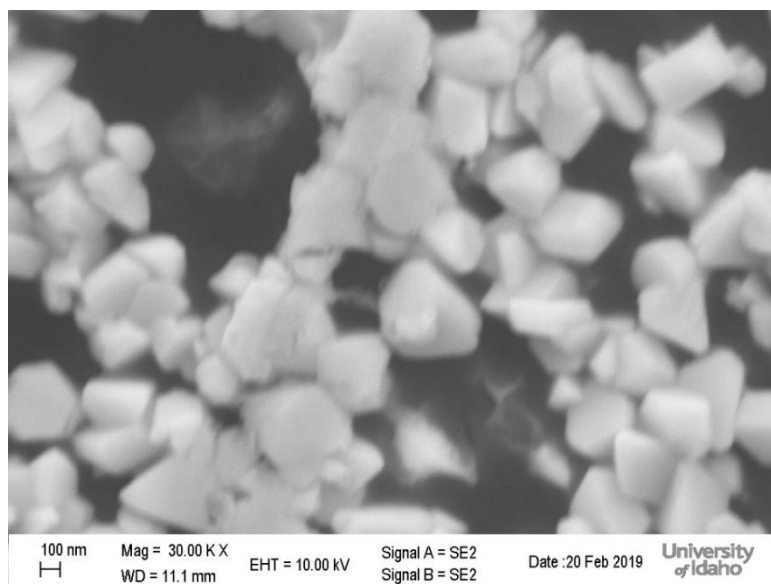


Figure 16: 60 second α deposition on glassy carbon

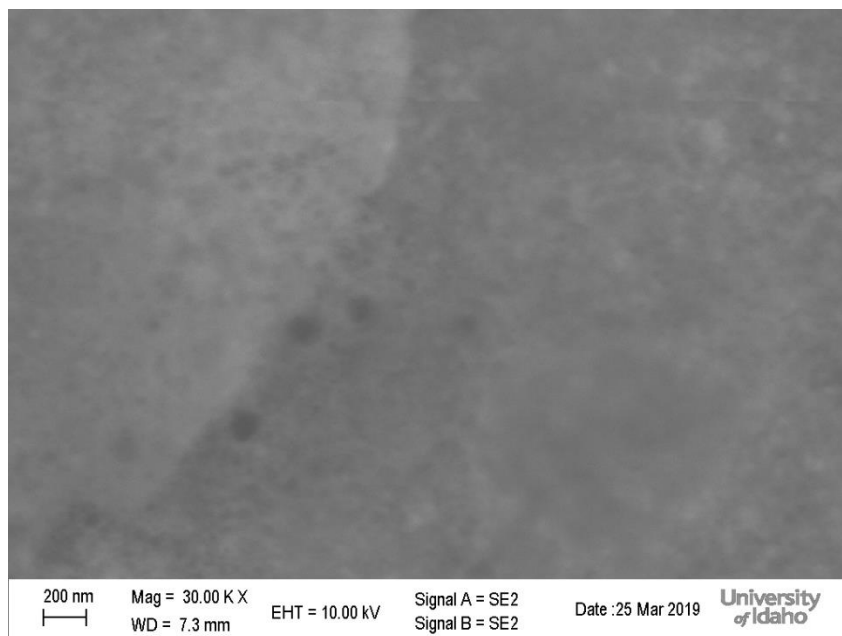


Figure 17: 300 second α deposition on glassy carbon

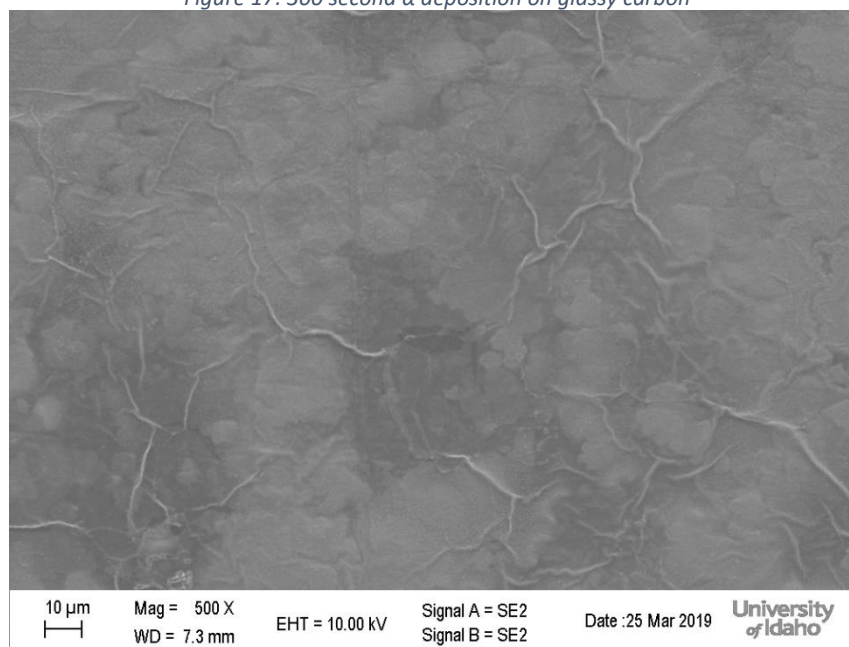


Figure 18: 300 second α deposition on glassy carbon

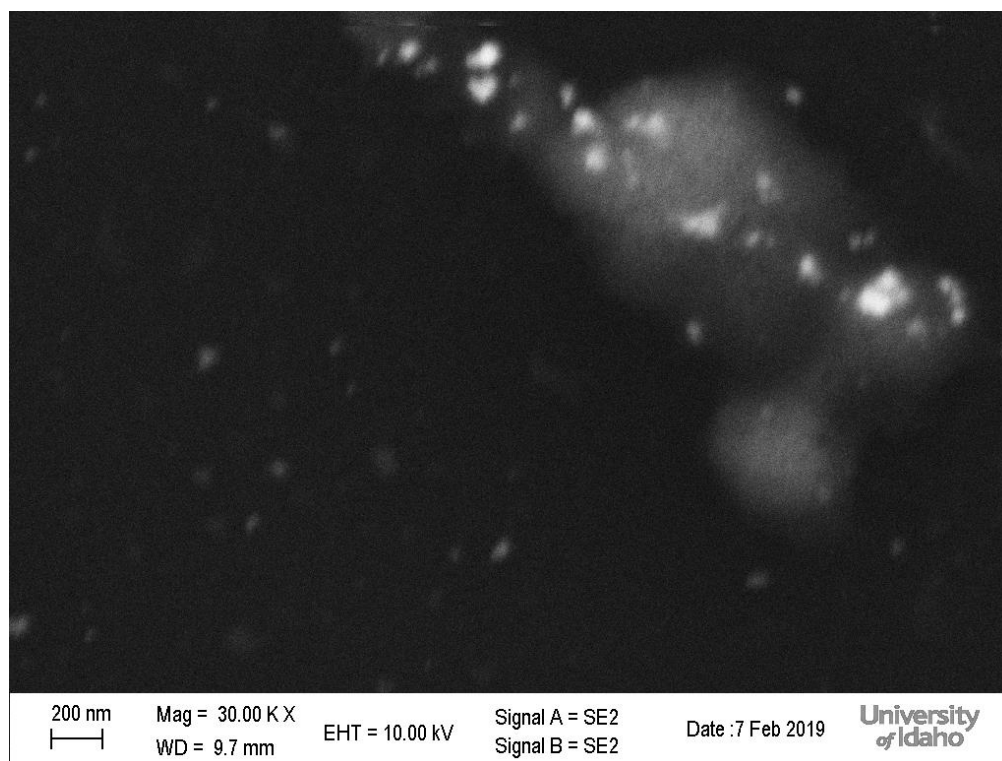


Figure 19: 10 second β deposition on glassy carbon

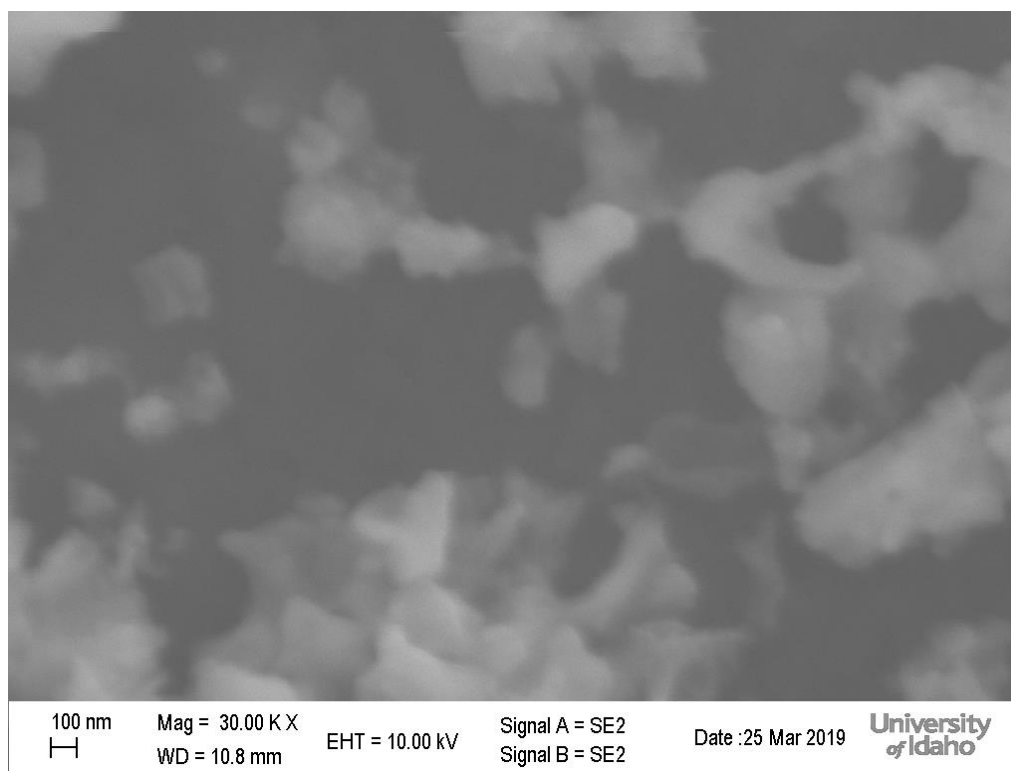


Figure 20: 30 second β deposition on glassy carbon

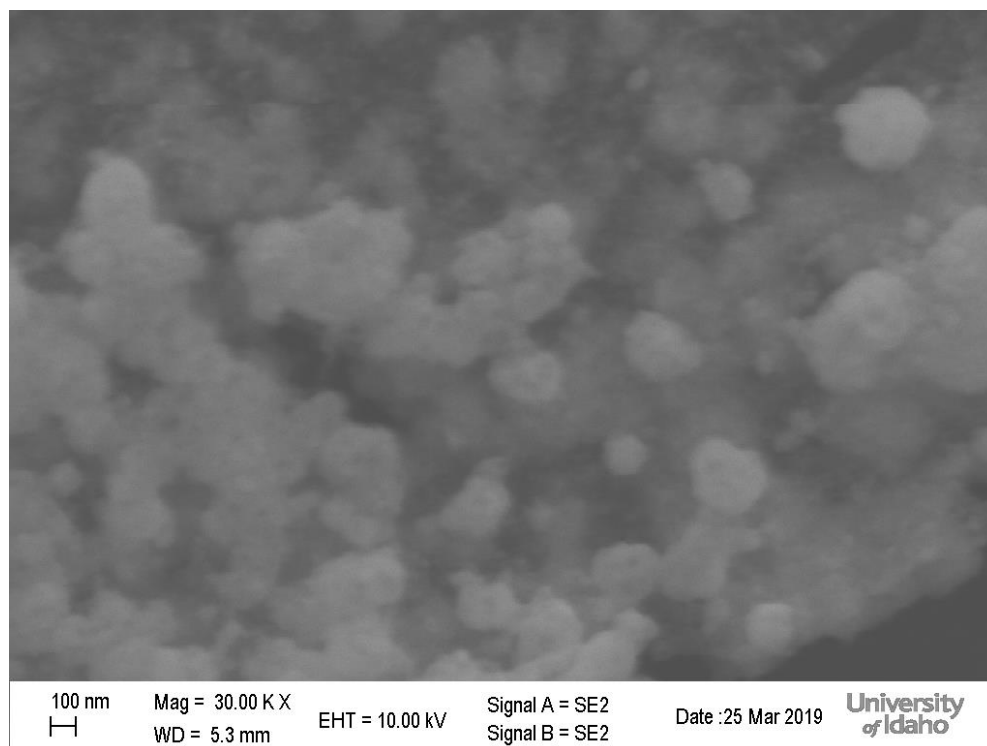


Figure 21: 60 second β deposition on glassy carbon

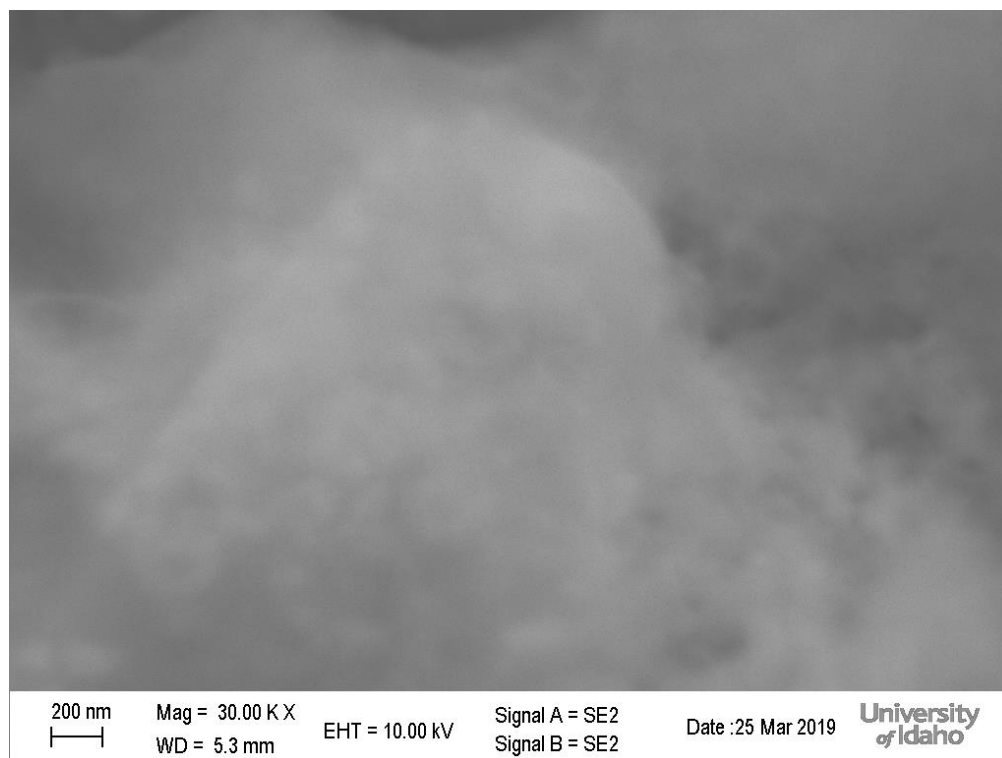


Figure 22: 300 second β deposition on glassy carbon 30000 magnification

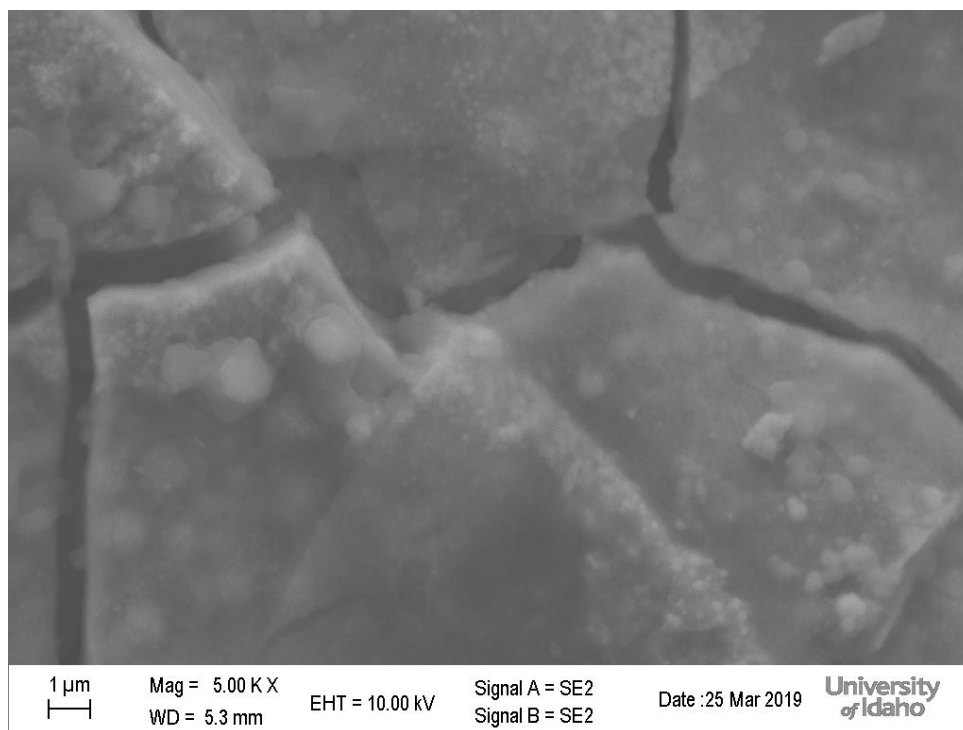


Figure 23: 300 second β deposition on glassy carbon 5000 magnification

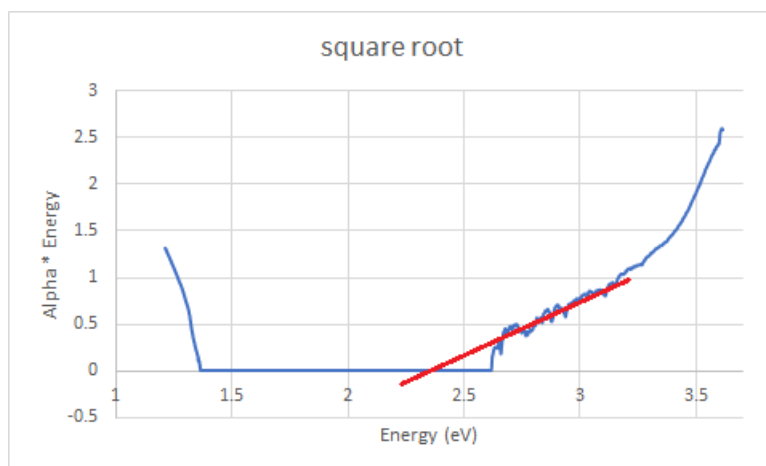


Figure 24: UV-Vis α as deposited

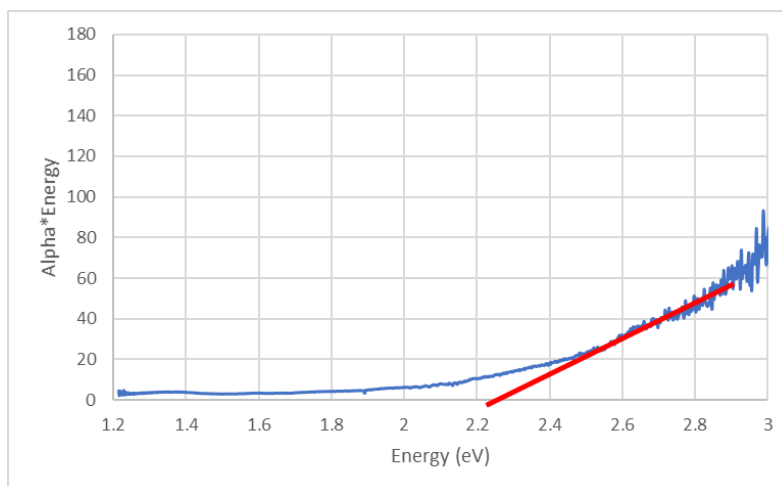


Figure 25: UV-Vis α annealed on FTO

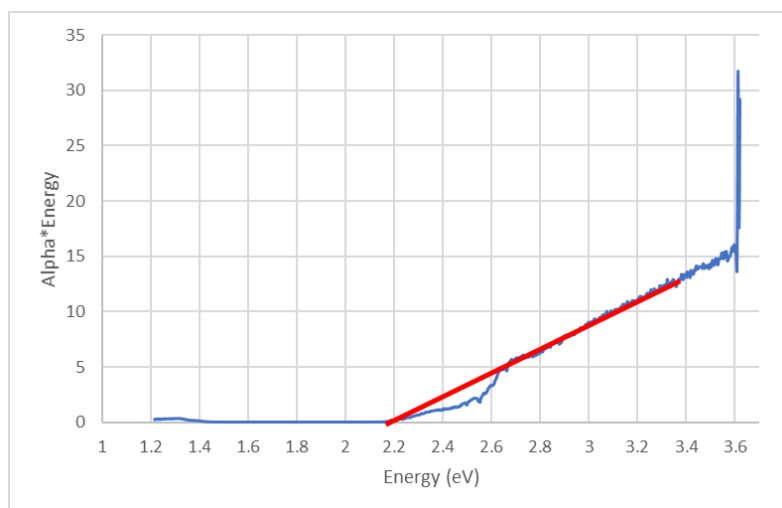


Figure 26: UV-Vis β as-deposited on FTO

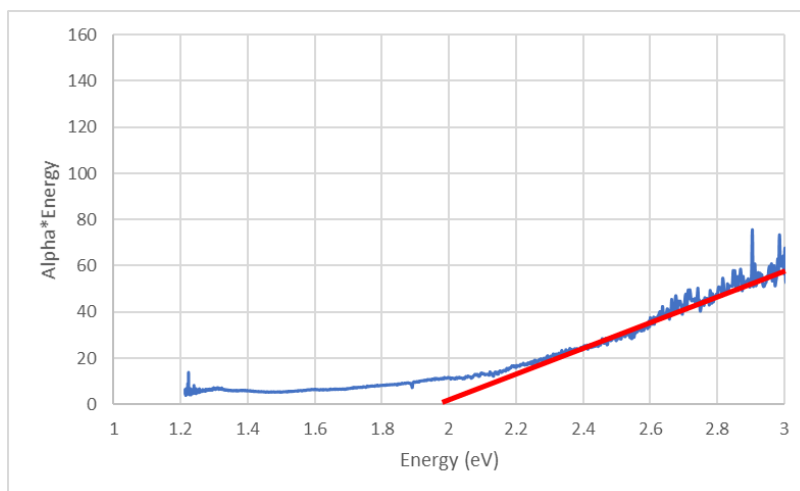


Figure 27: UV-Vis β annealed on FTO

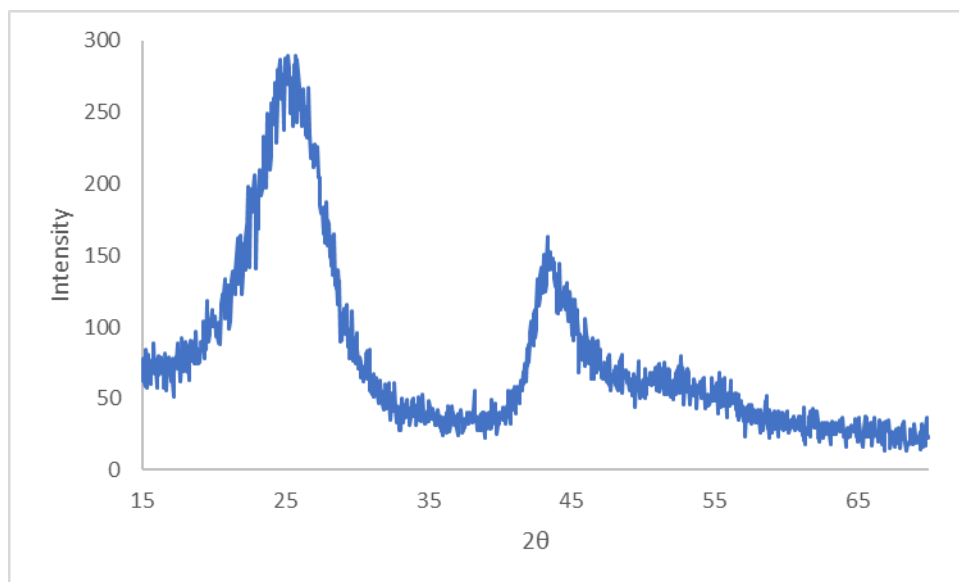


Figure 28: XRD as deposited α phase

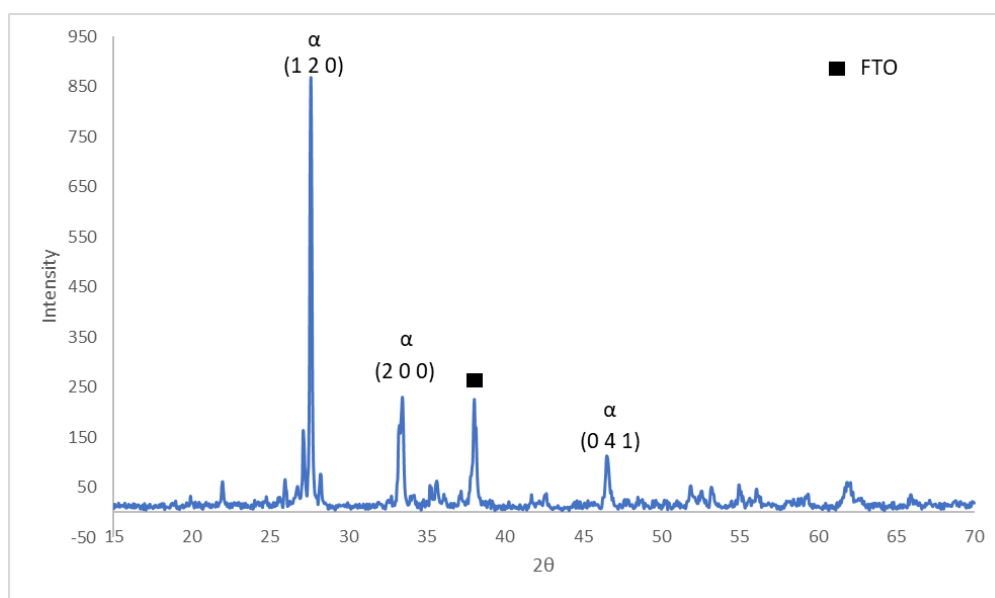


Figure 29: XRD α phase calcined 500°C

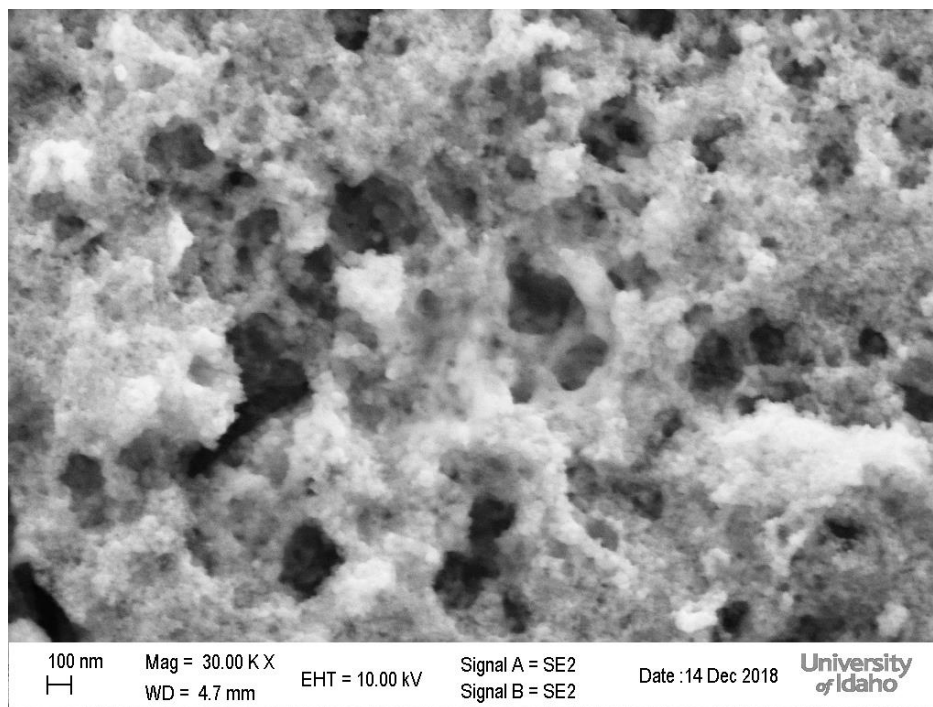


Figure 30: As-deposited α phase on GC 30000 X magnification

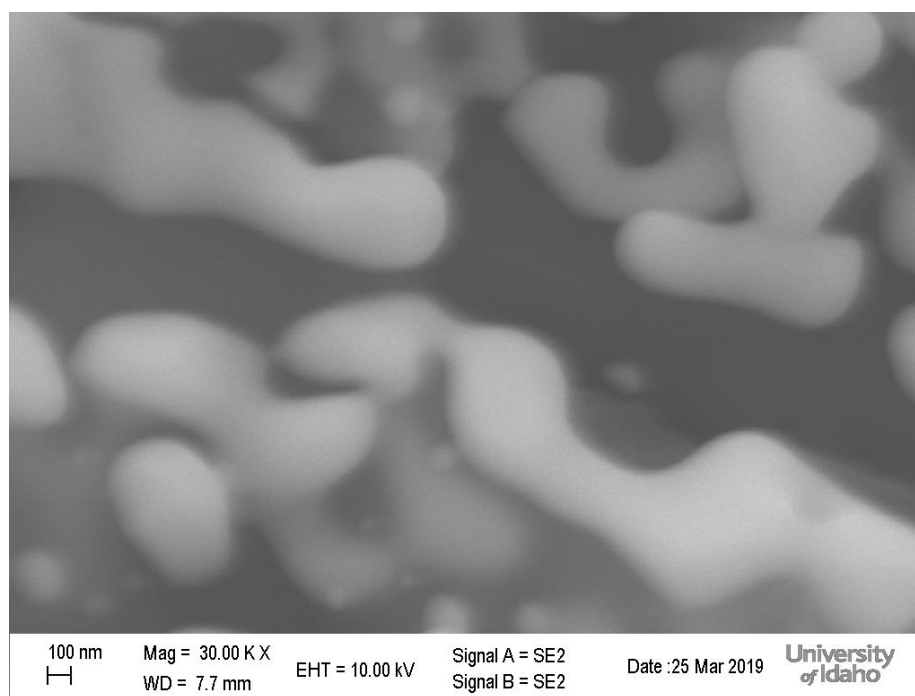


Figure 31: Calcined 500°C α phase GC

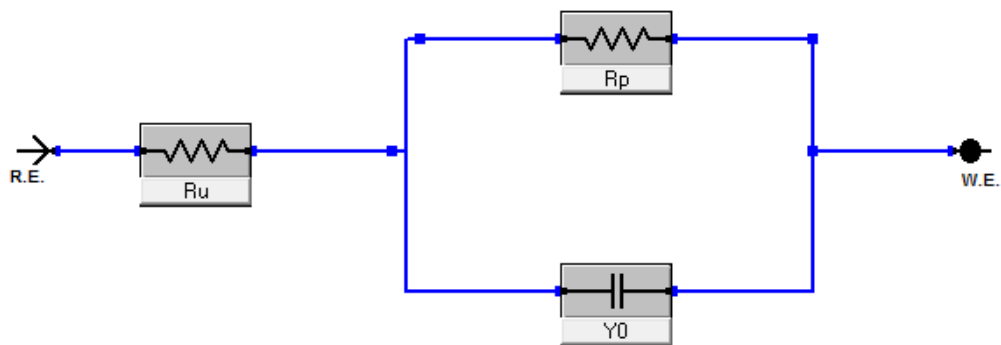


Figure 32: Circuit equivalent for as deposited and annealed α and Exp. 1 and Exp. 2 CB

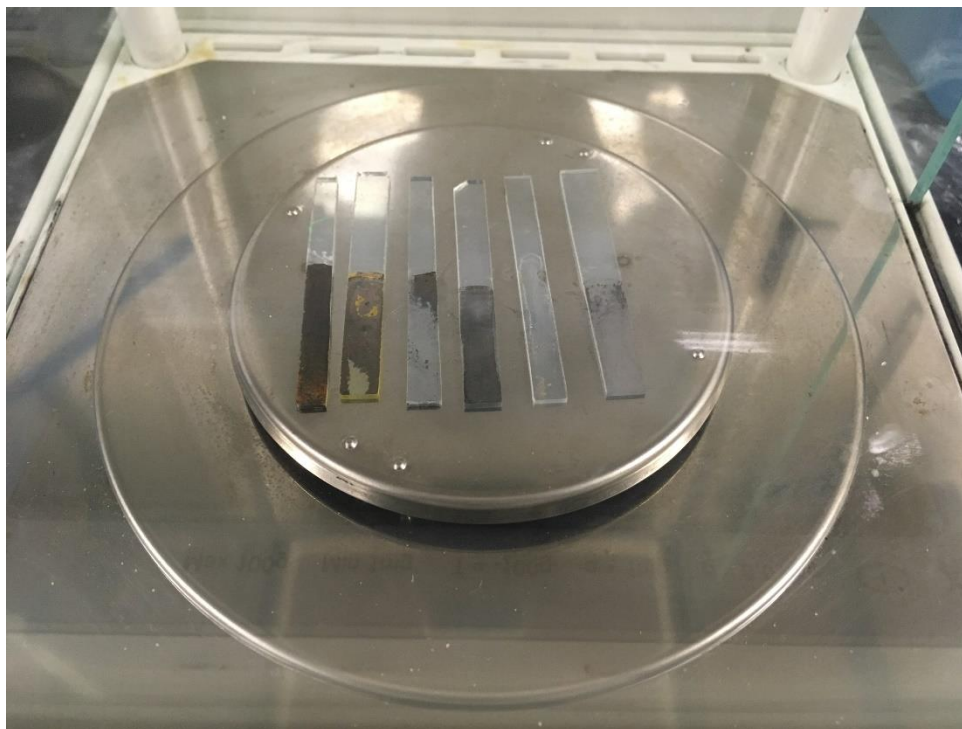


Figure 33: Post 1mA CCD testing of FTO samples from left to right: as deposited CB, annealed CB, as deposited β , annealed β , as deposited α , annealed α

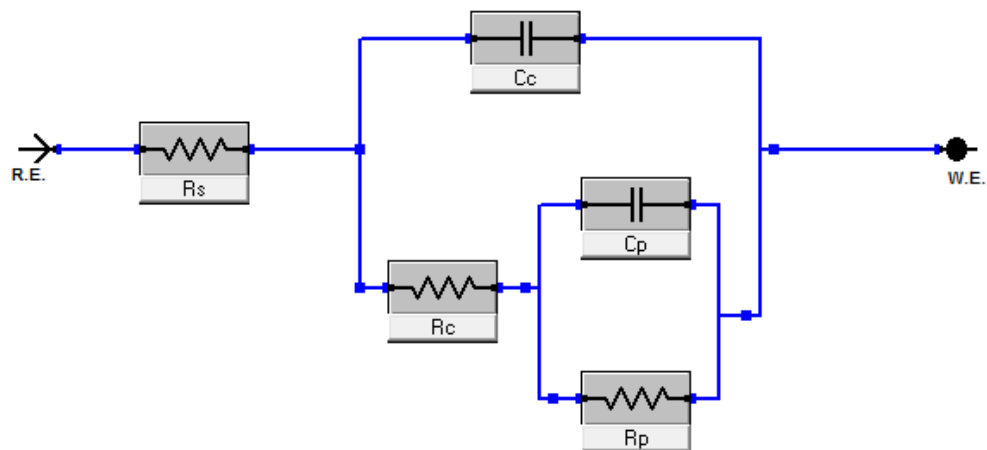


Figure 34: Circuit equivalent for Exp. 3 for annealed α , annealed β , annealed CB

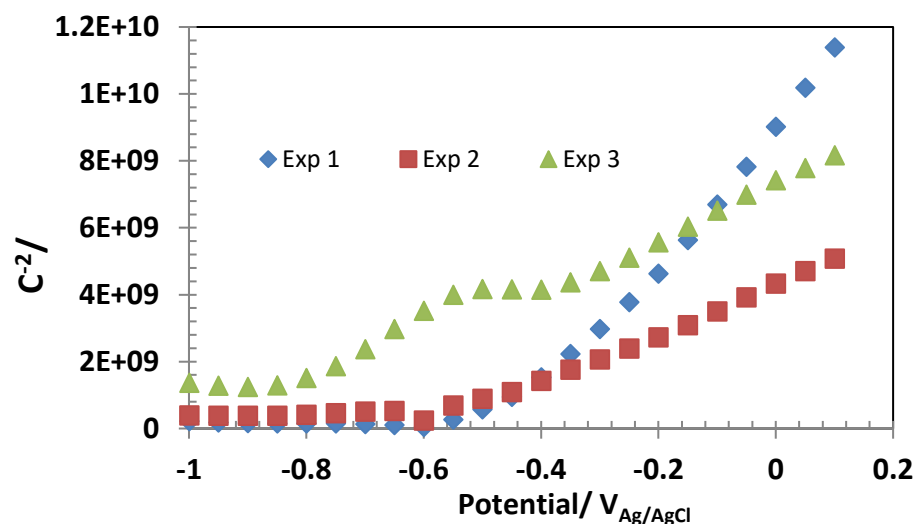


Figure 35: Mott Schottky data for as deposited α phase

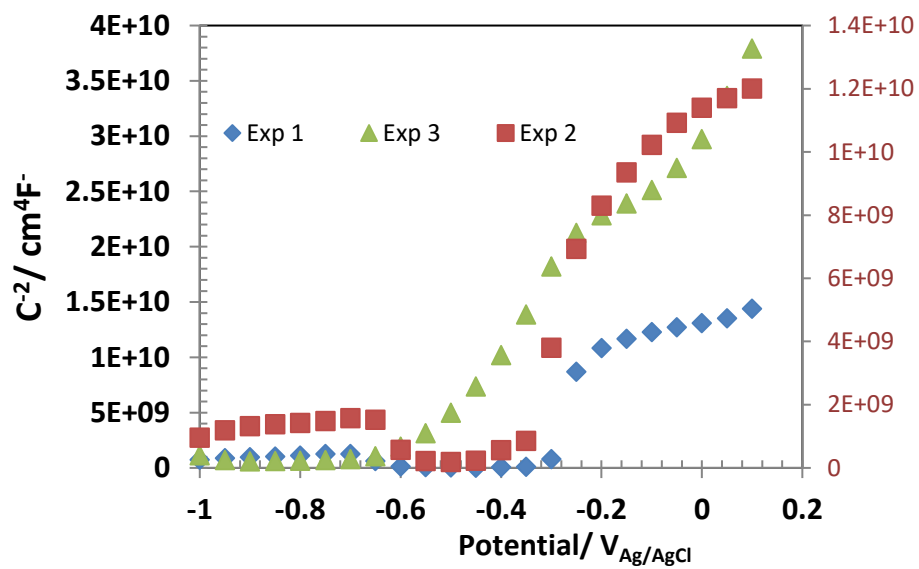


Figure 36: Mott Schottky data for annealed α phase

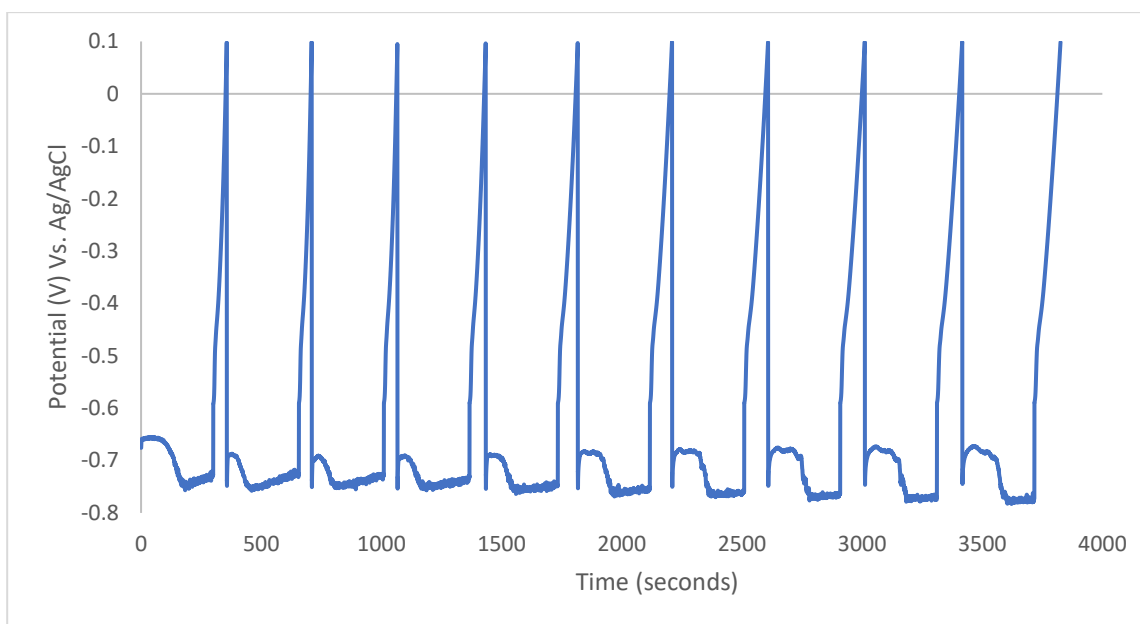


Figure 37: CCD 0.1 mA as deposited α phase

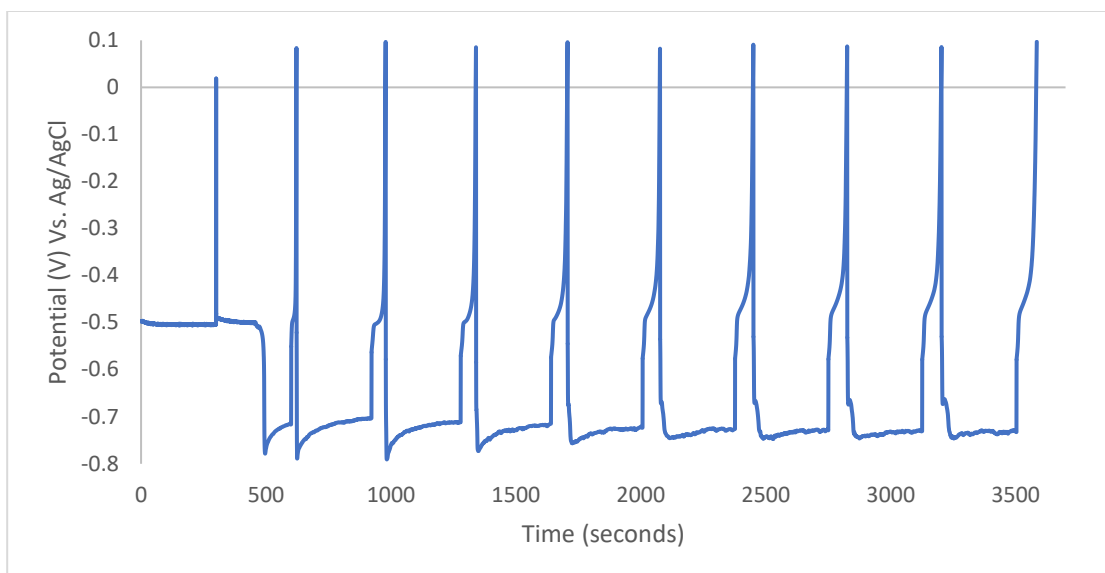


Figure 38: CCD 0.1 mA annealed α phase

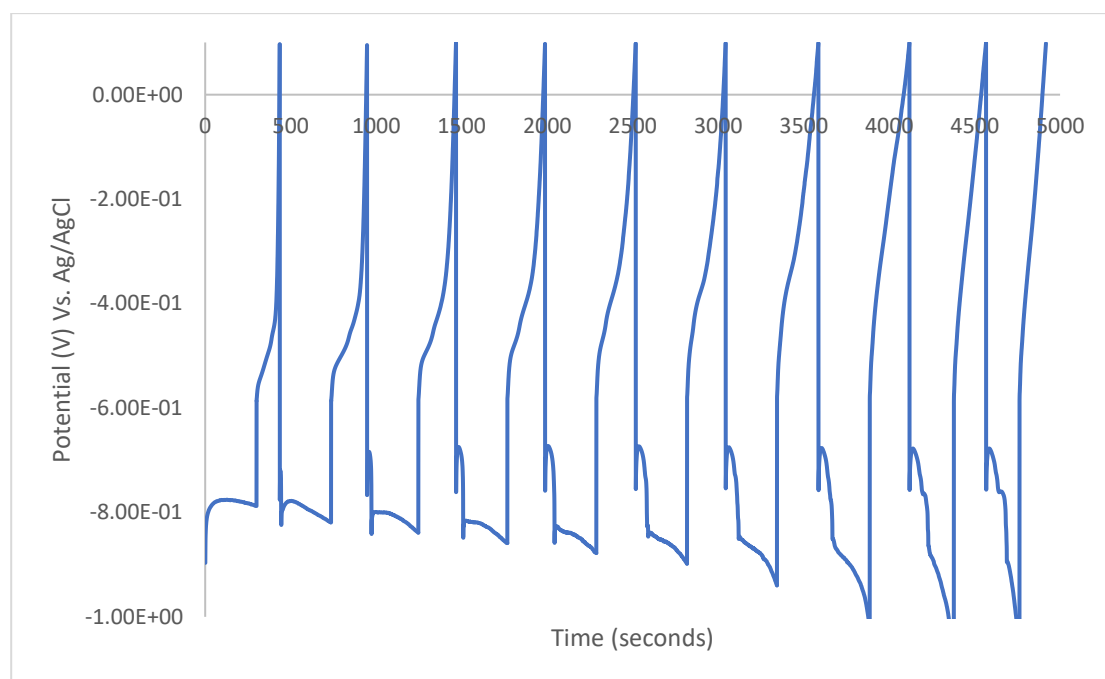


Figure 39: CCD 1 mA annealed α phase

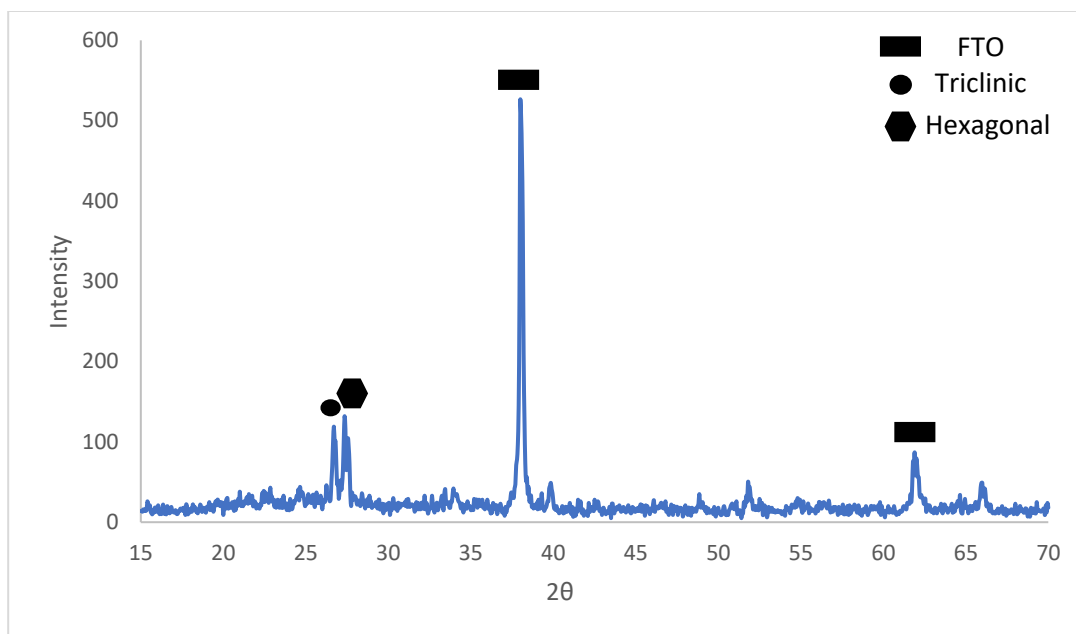


Figure 40: XRD α annealed post-experiment

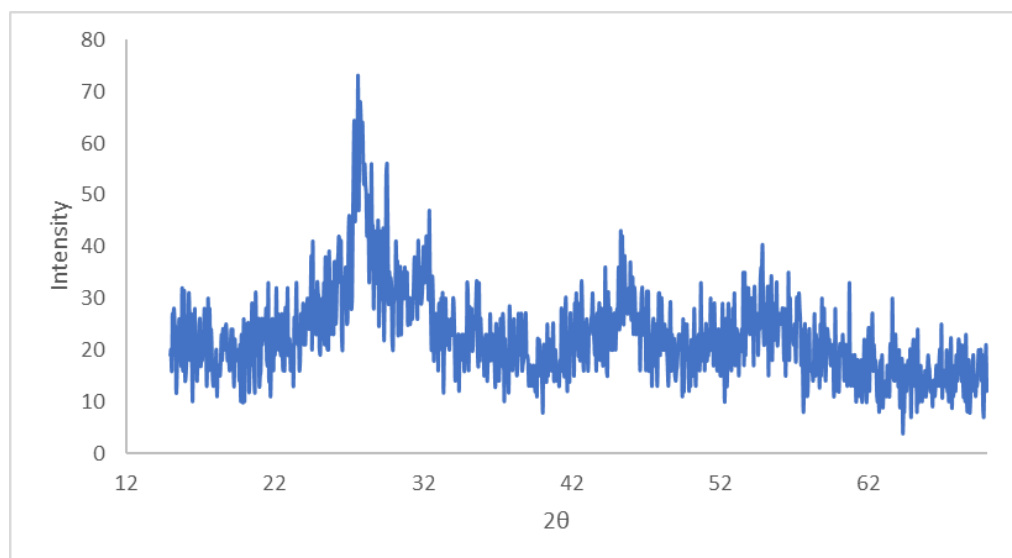


Figure 41: XRD as deposited β phase

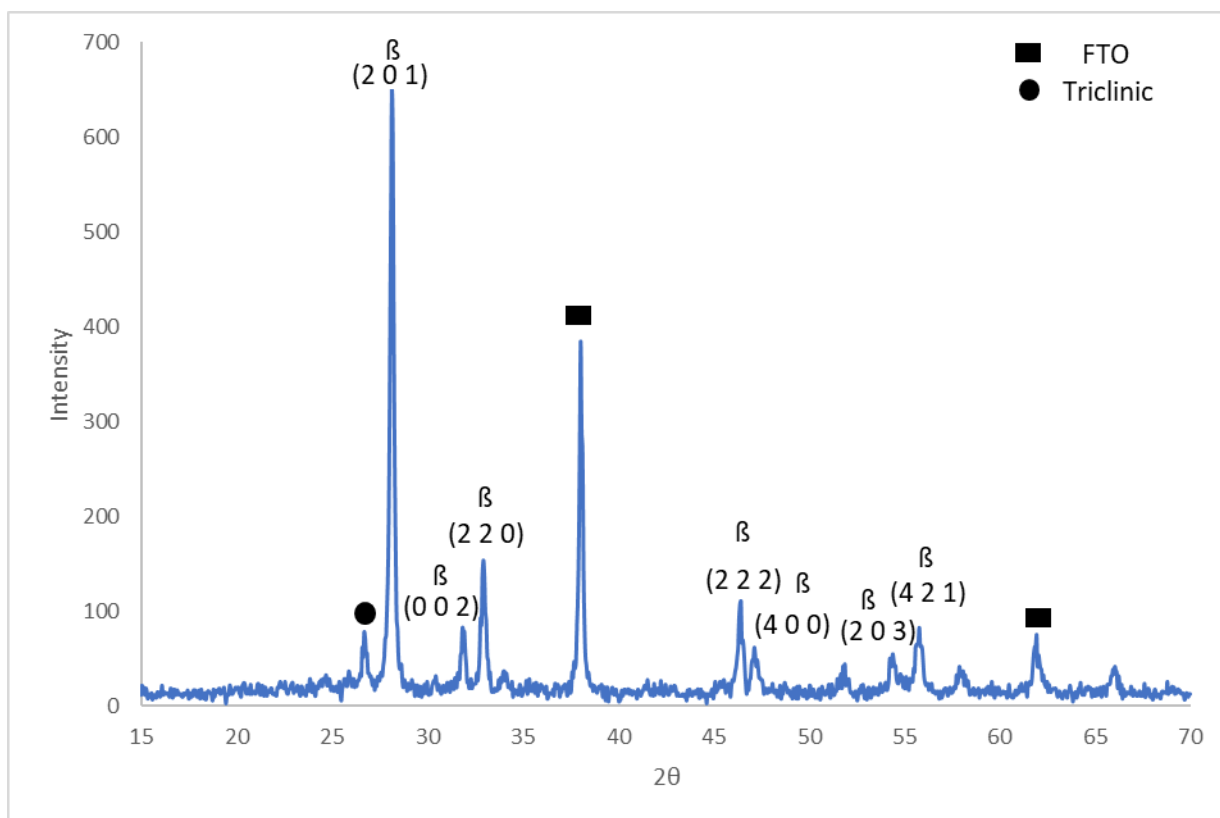


Figure 42: XRD of annealed β phase

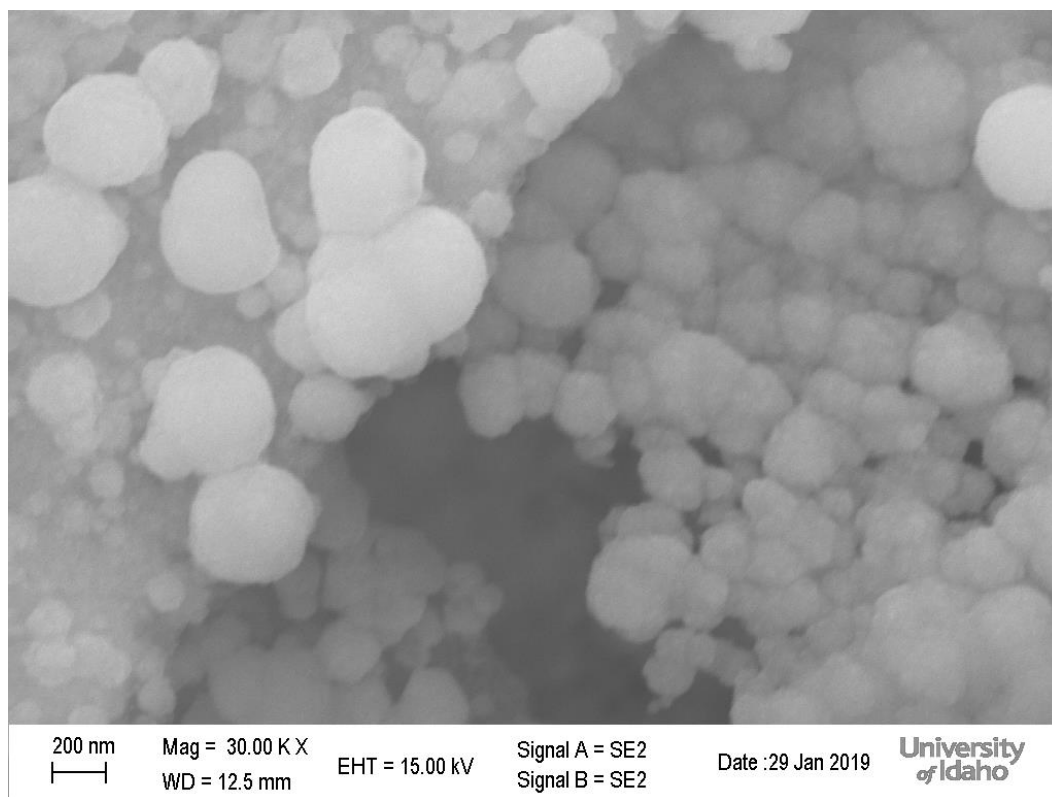


Figure 43: XRD as deposited β phase on glassy carbon

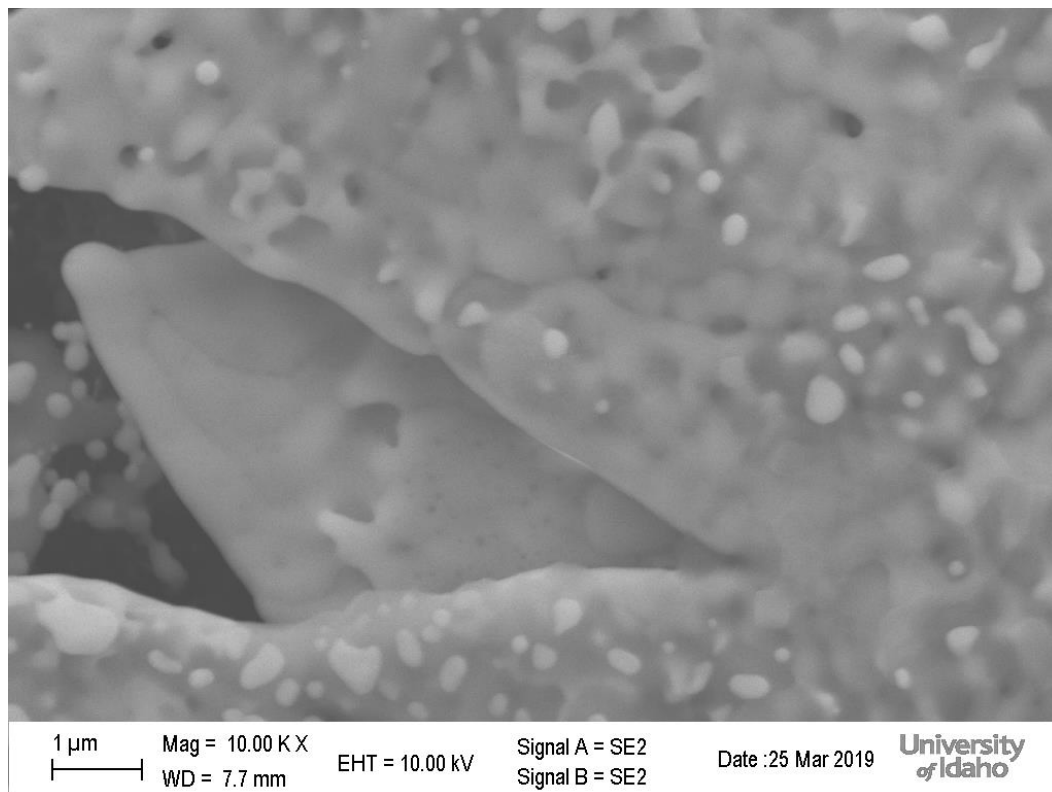


Figure 44: XRD annealed β phase on glassy carbon

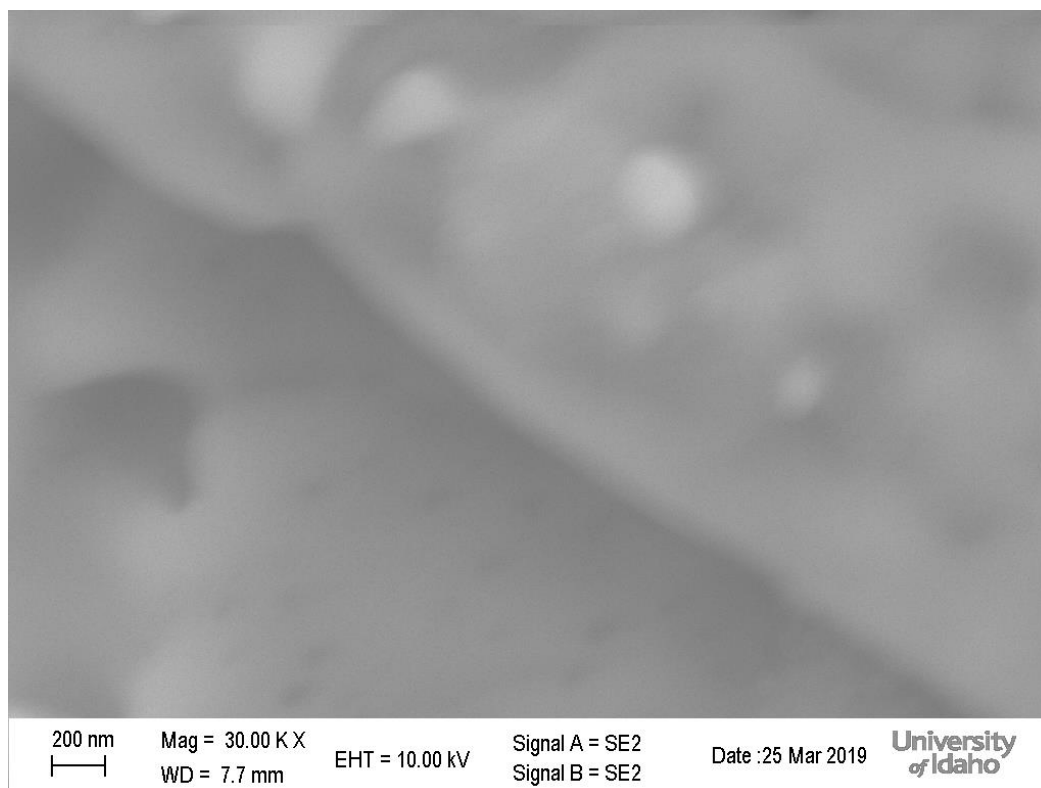


Figure 45: XRD annealed β phase on glassy carbon

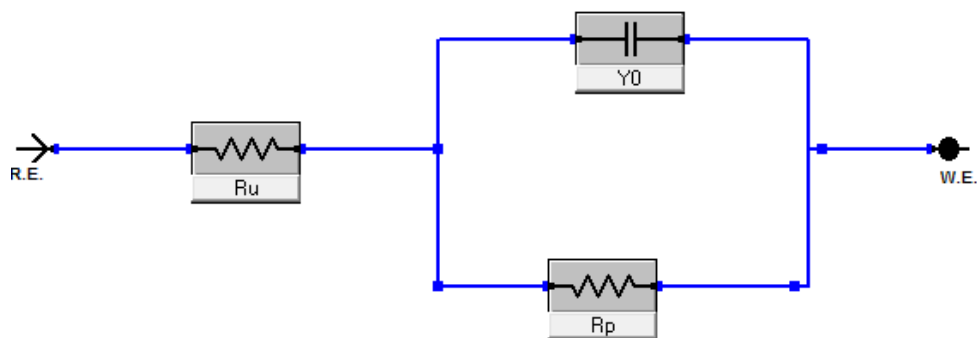


Figure 46: Circuit equivalent for as deposited and Exp.1 and Exp. 2 annealed β phase

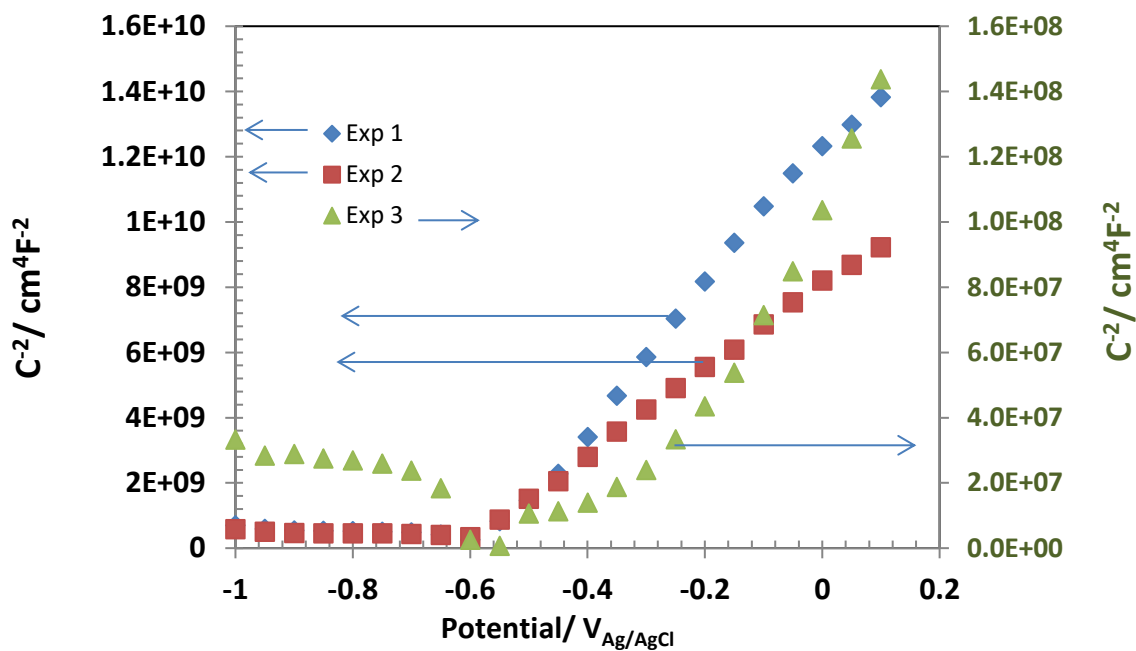


Figure 47: Mott-Schottky for as deposited β phase

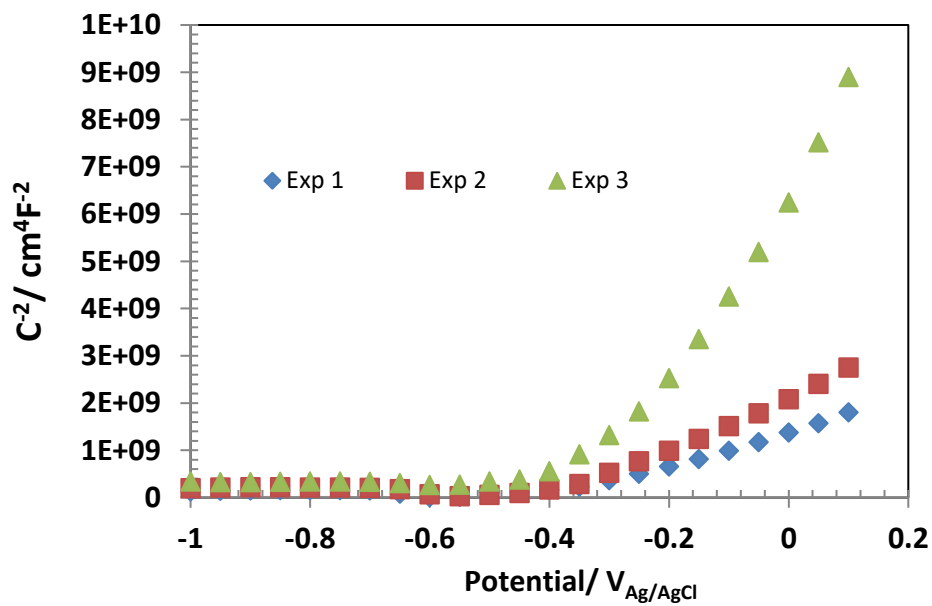


Figure 48: Mott-Schottky for annealed β phase

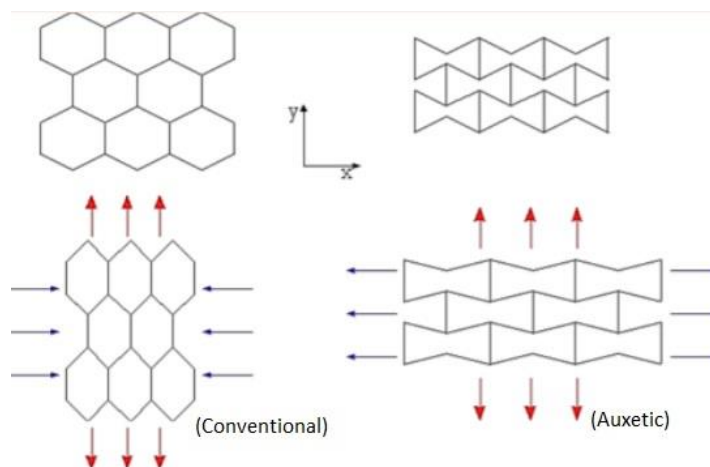


Figure 49: Auxetic behavior [22]

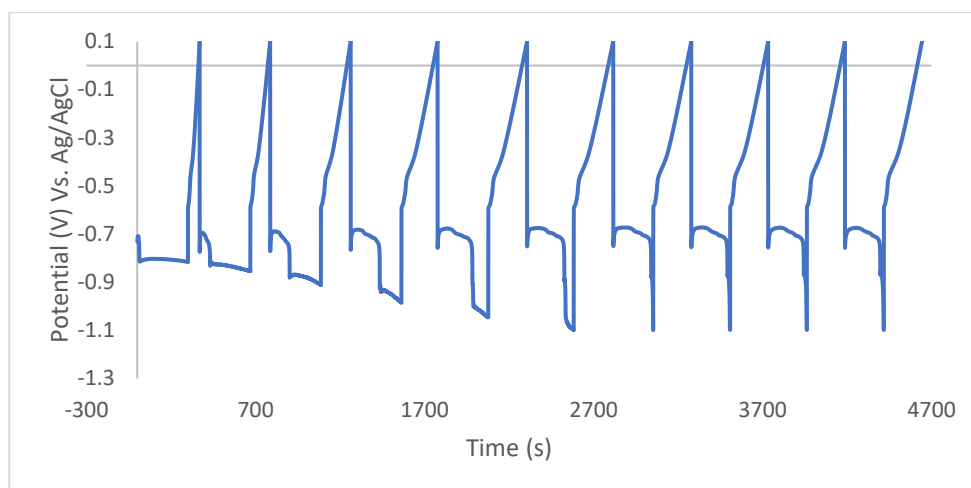


Figure 50: CCD 0.1 mA as deposited β phase

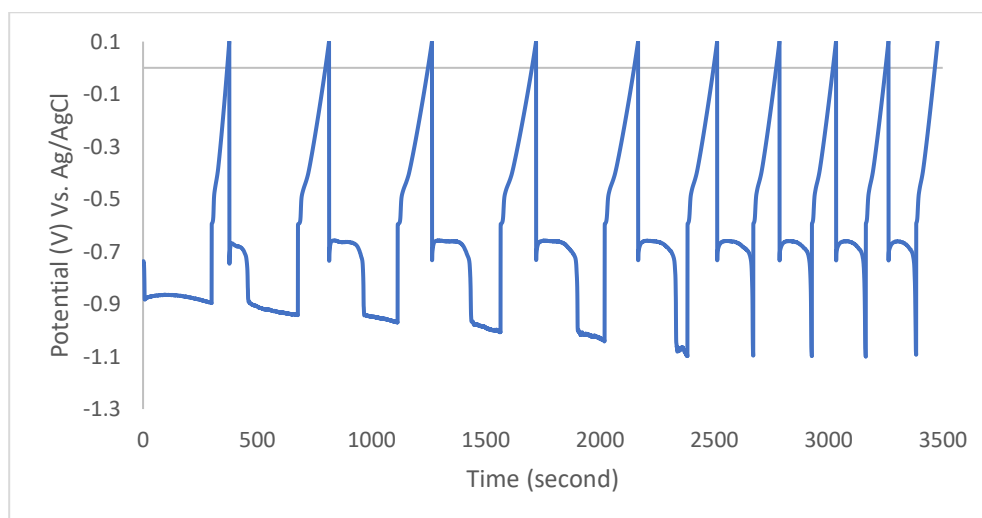
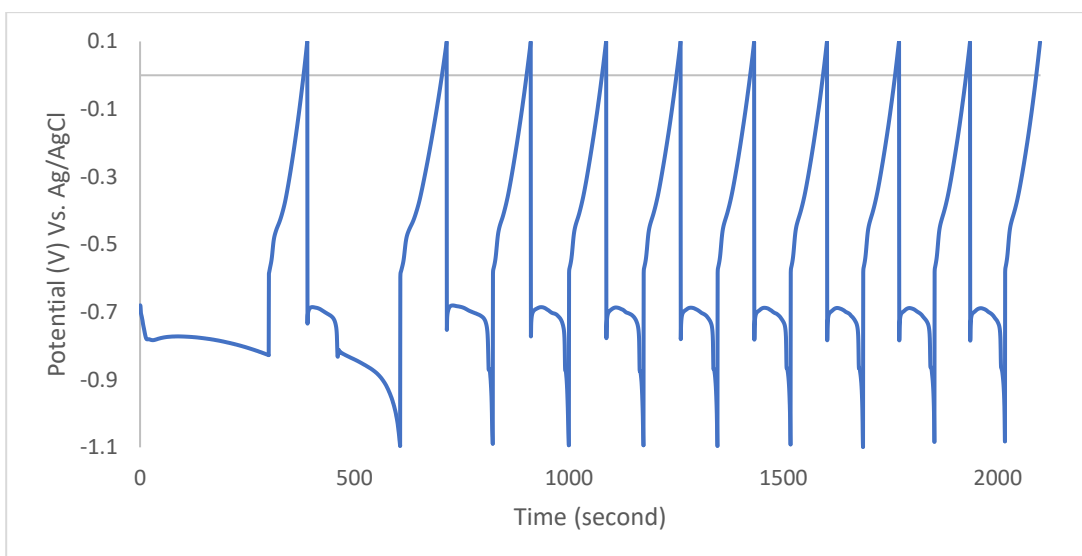
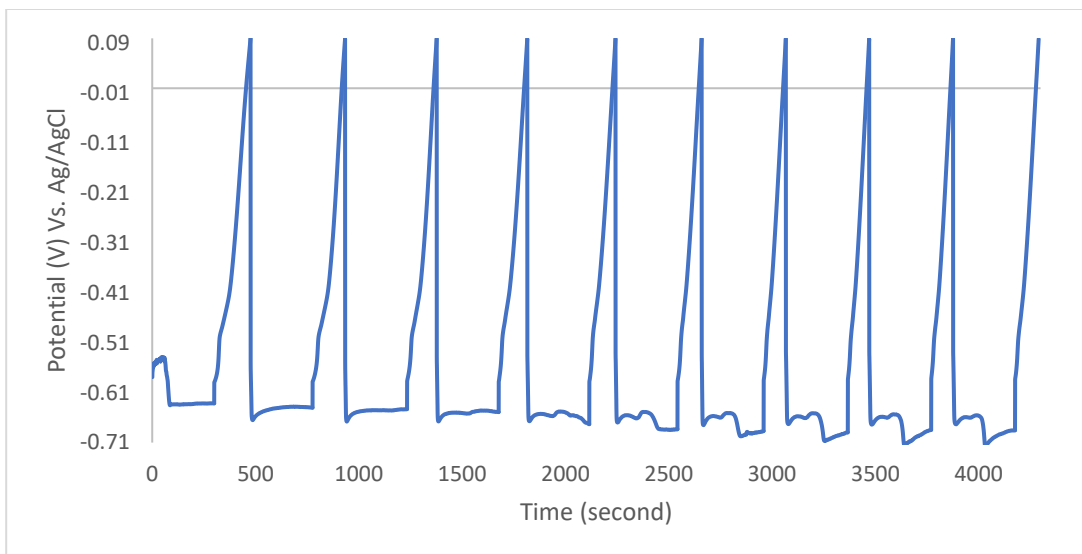


Figure 51: CCD 1 mA as deposited β phase



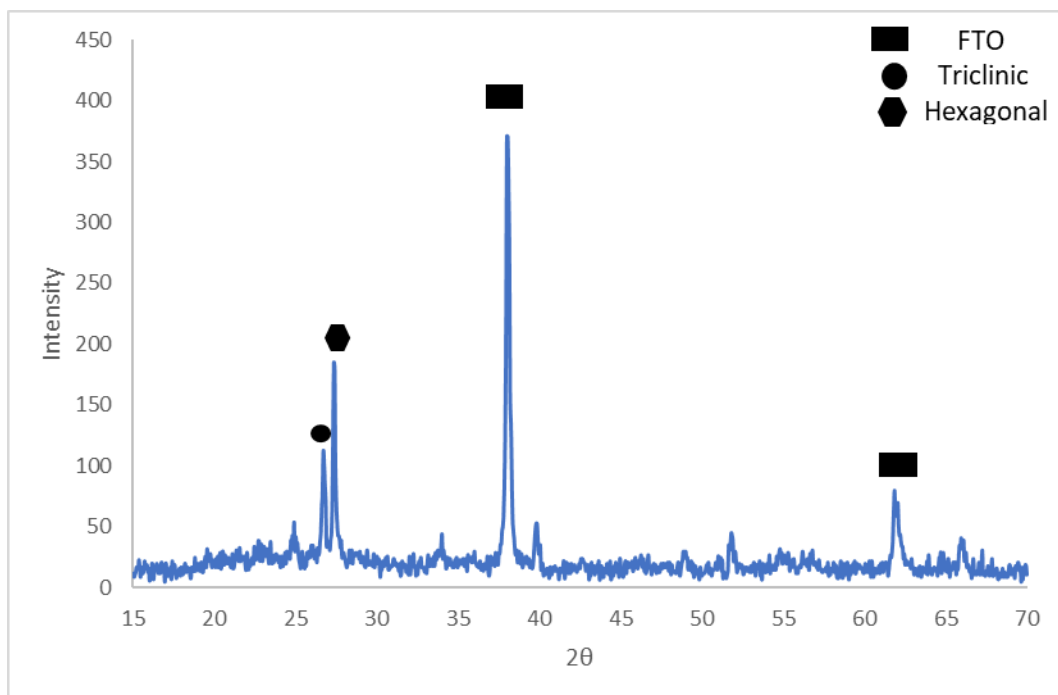


Figure 54: XRD post experiment as deposited β phase

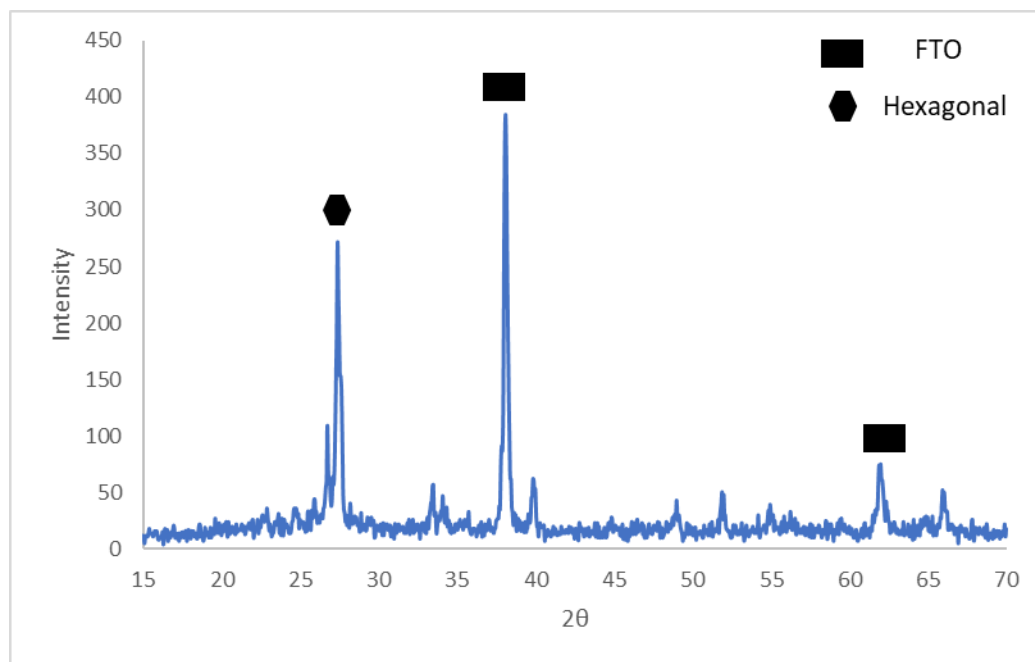


Figure 55: XRD post experiment annealed β phase

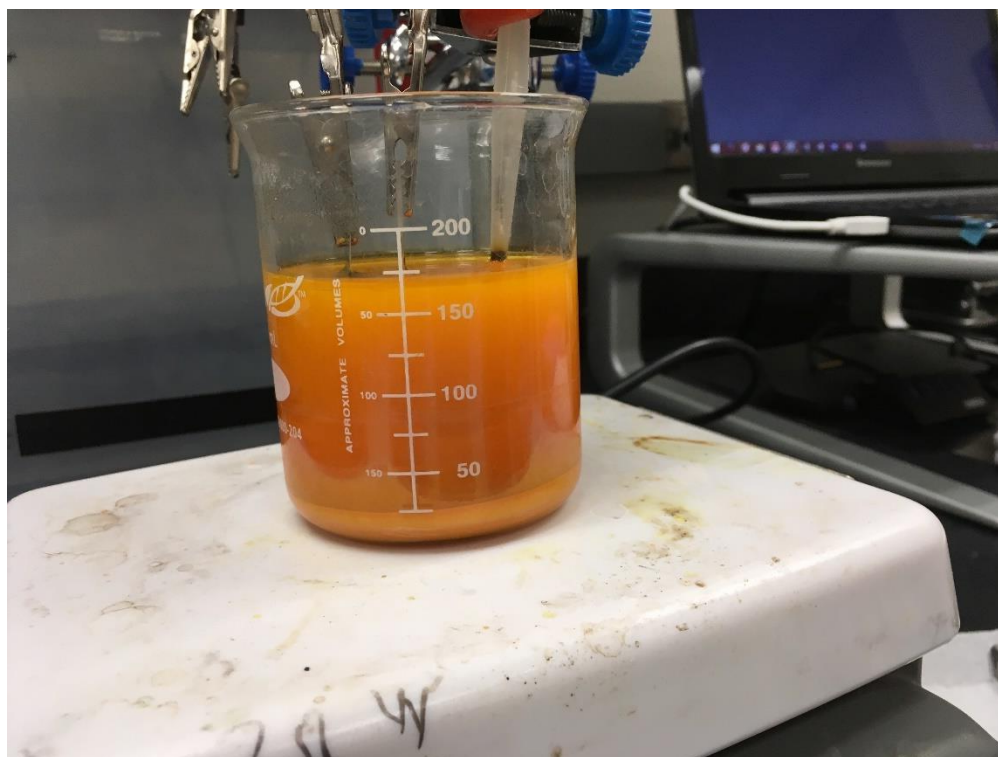


Figure 56: Chombismite solution from left to right: Platinum Counter Electrode, FTO Glass Working Electrode, Ag/AgCl Reference Electrode

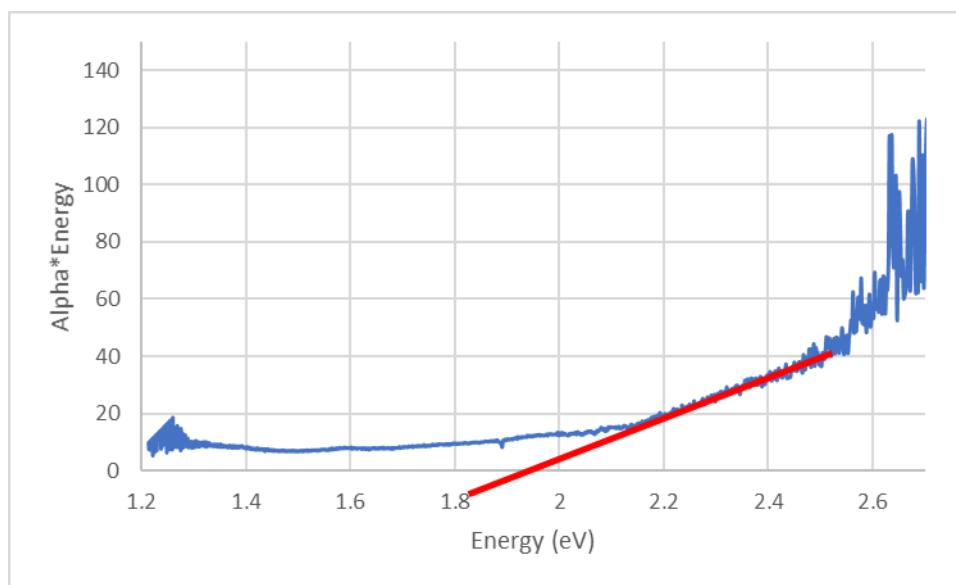


Figure 57: UV-Vis CB

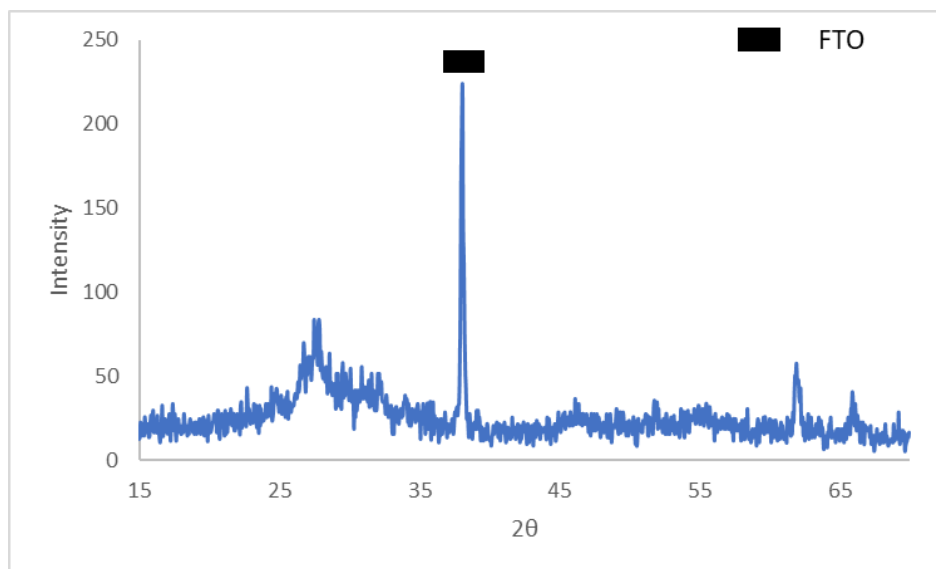


Figure 58: XRD as deposited chrombismite

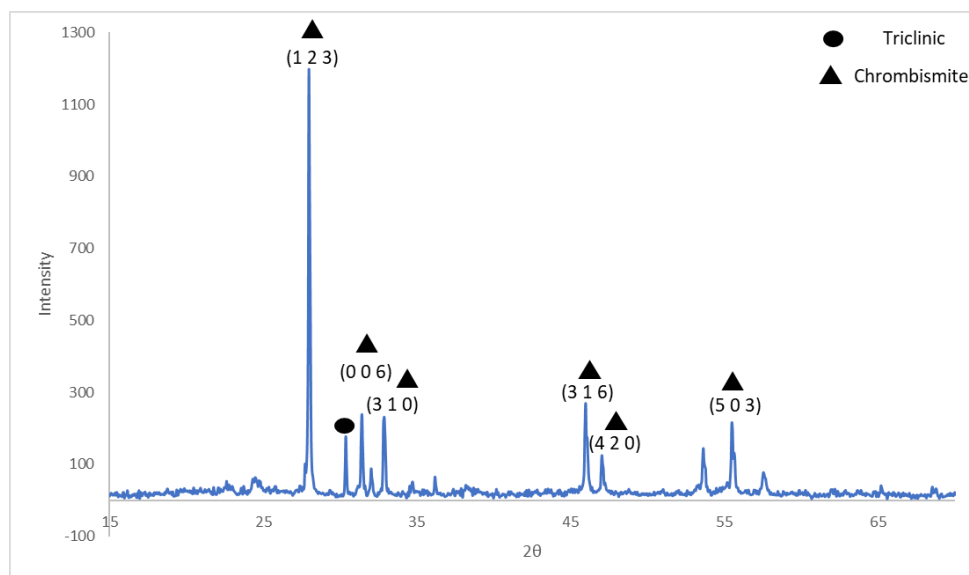


Figure 59: XRD annealed chrombismite

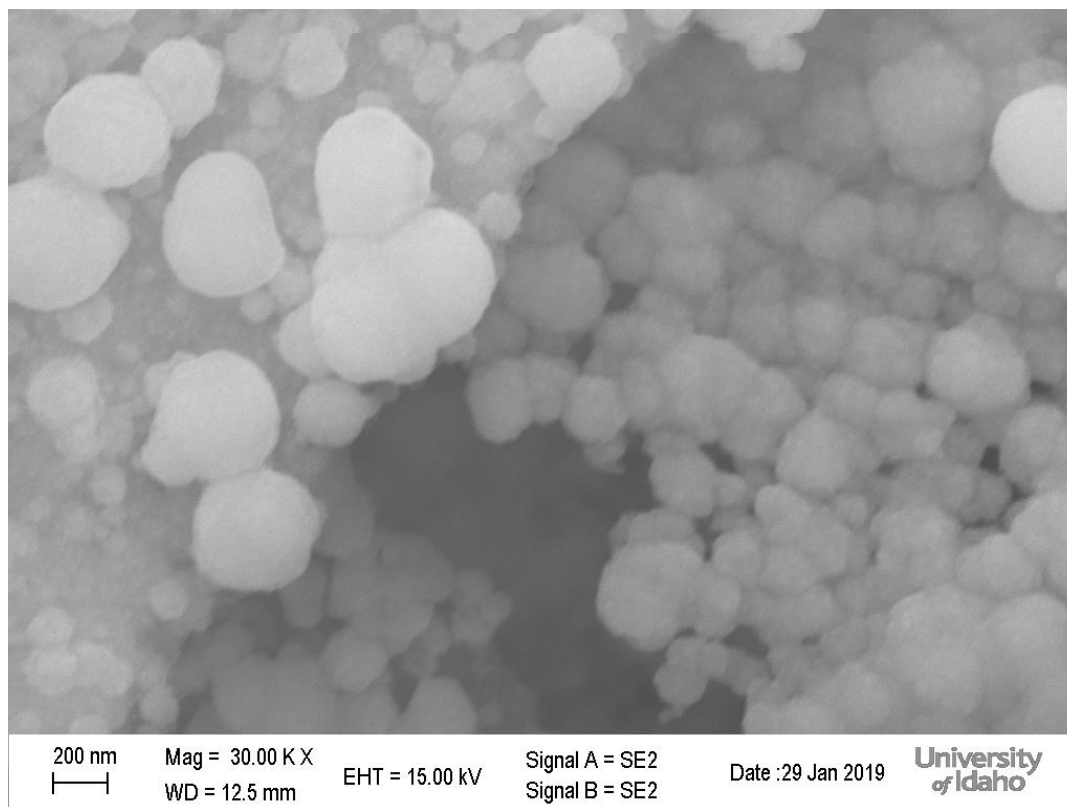


Figure 60: As deposited chrombismite

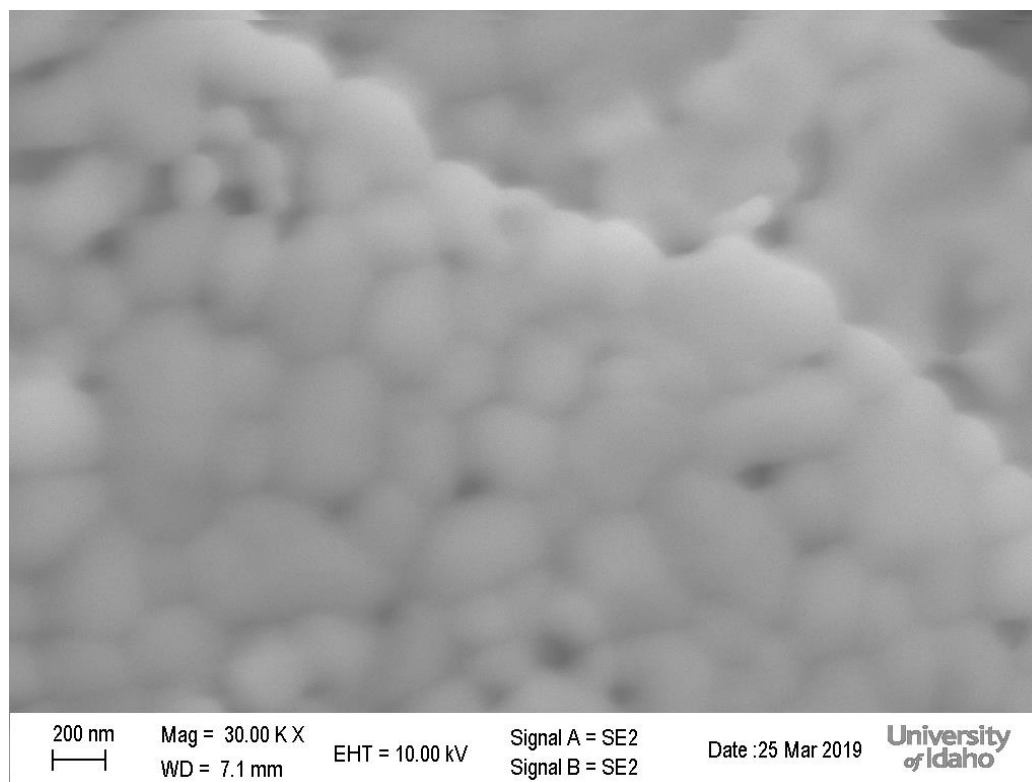


Figure 61: Annealed chrombismite

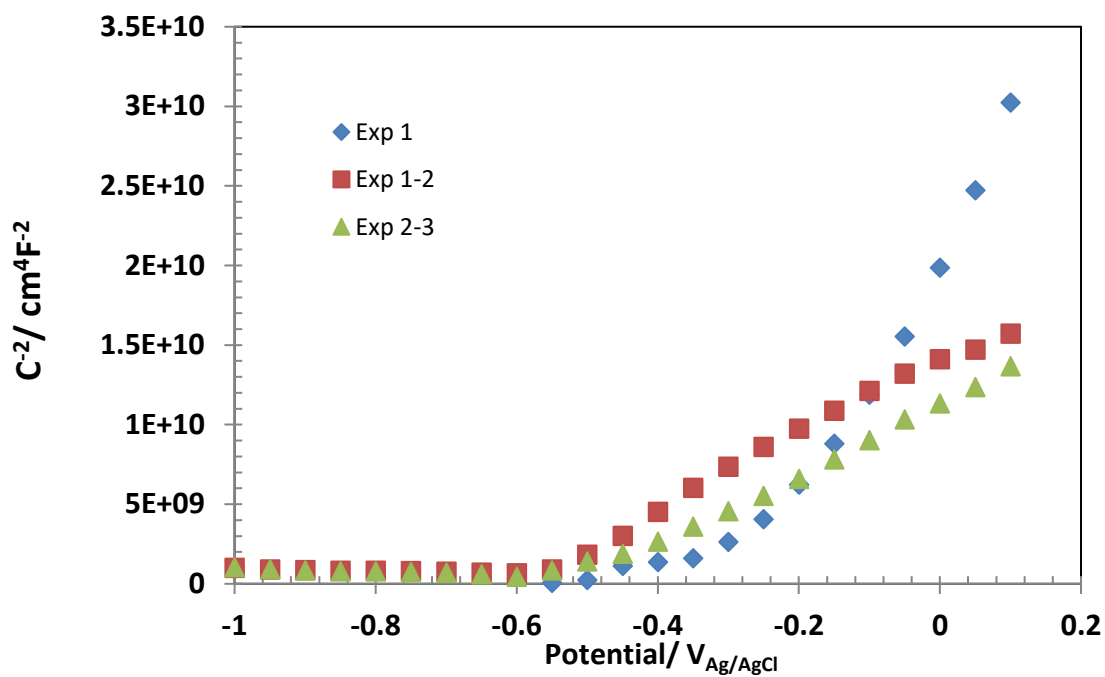


Figure 62: Mott-Schottky for as deposited chrombismite

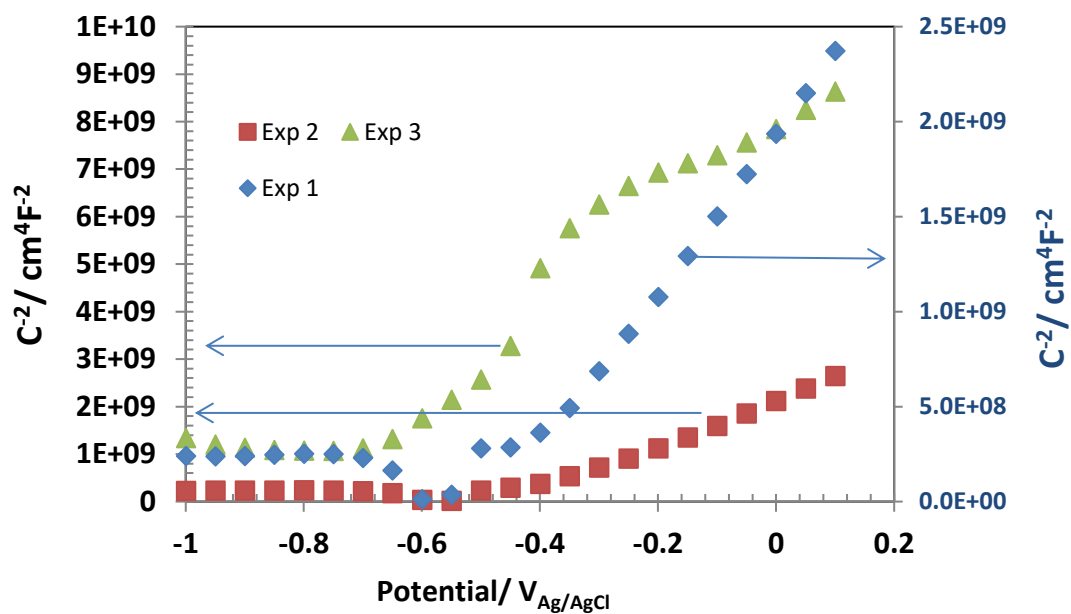


Figure 63: Mott Schottky for annealed chrombismite

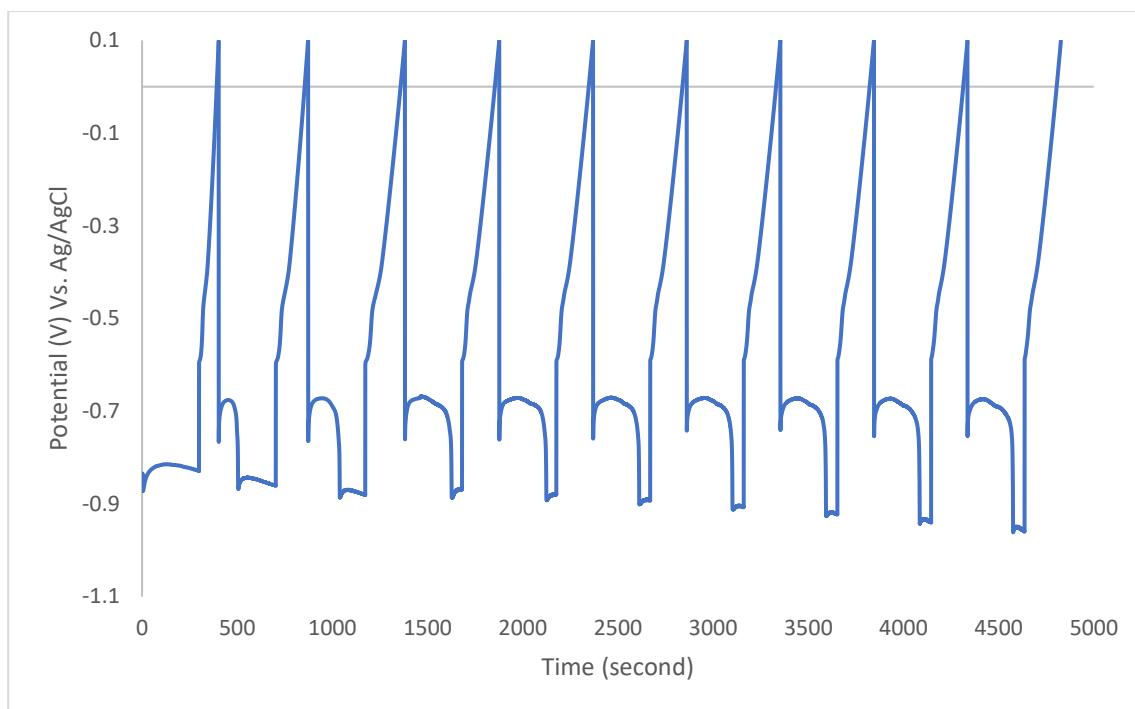


Figure 64: CCD 0.1 mA for as deposited chrombismite

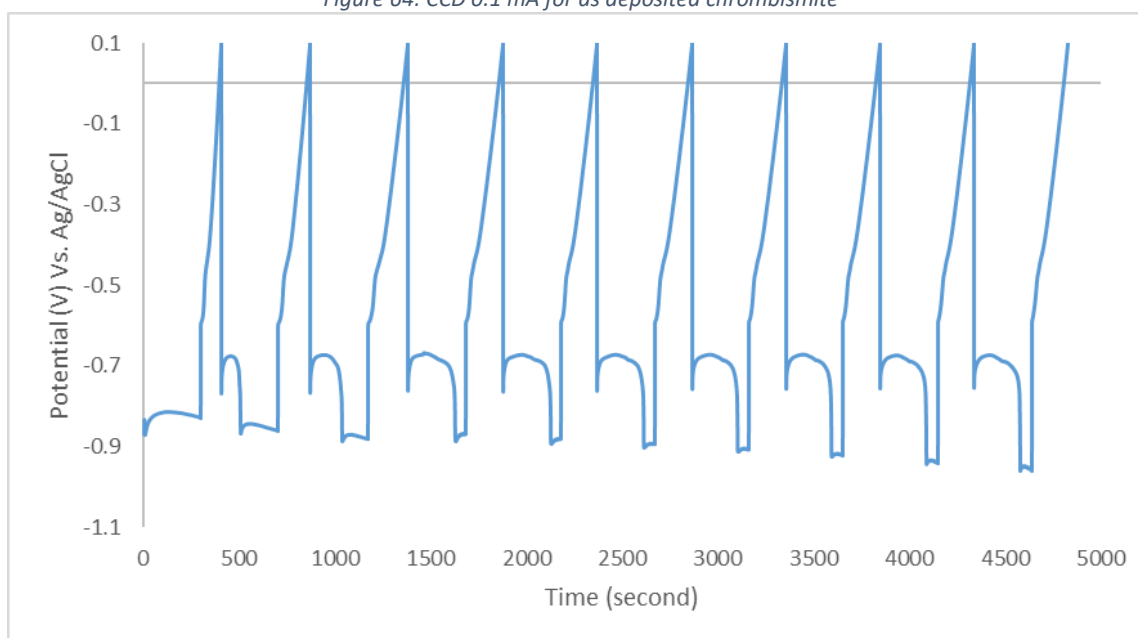


Figure 65: CCD 1 mA for as deposited chrombismite

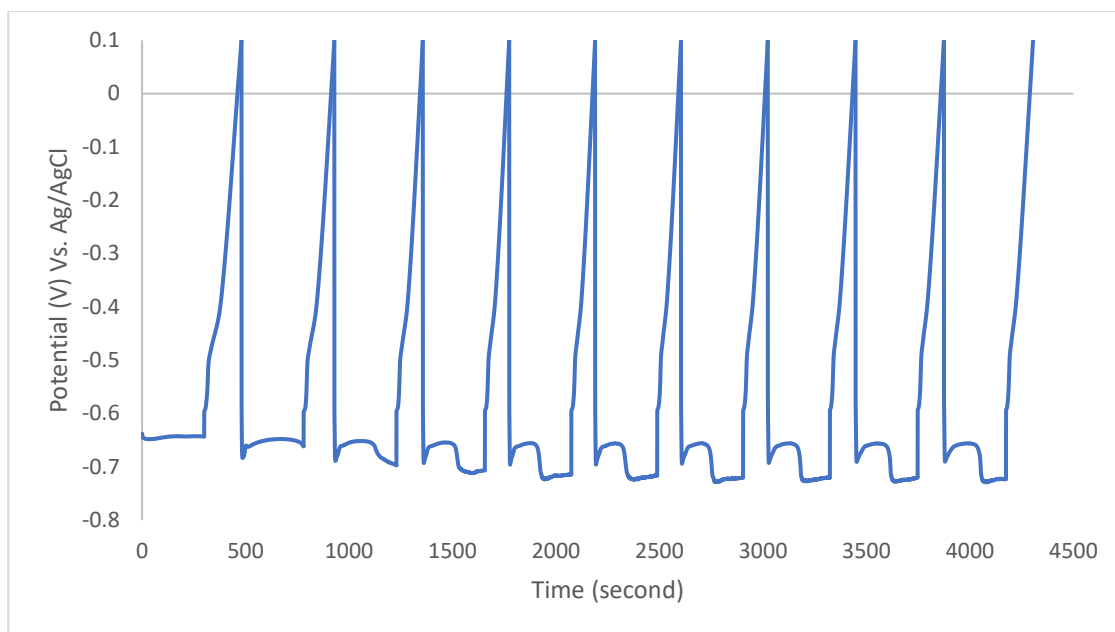


Figure 66: CCD 0.1 mA for annealed chrombismite

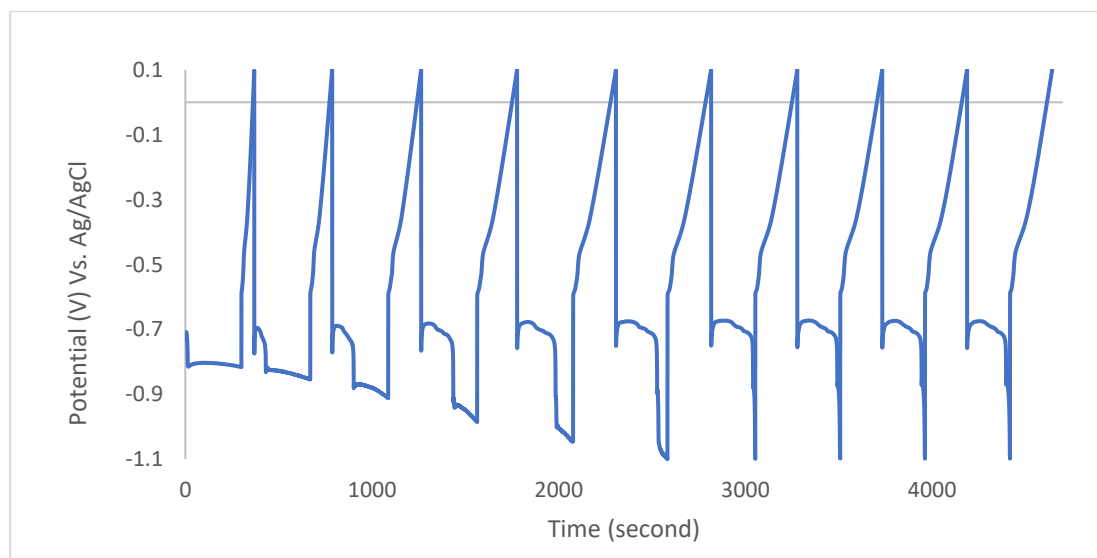


Figure 67: CCD 1 mA for annealed chrombismite

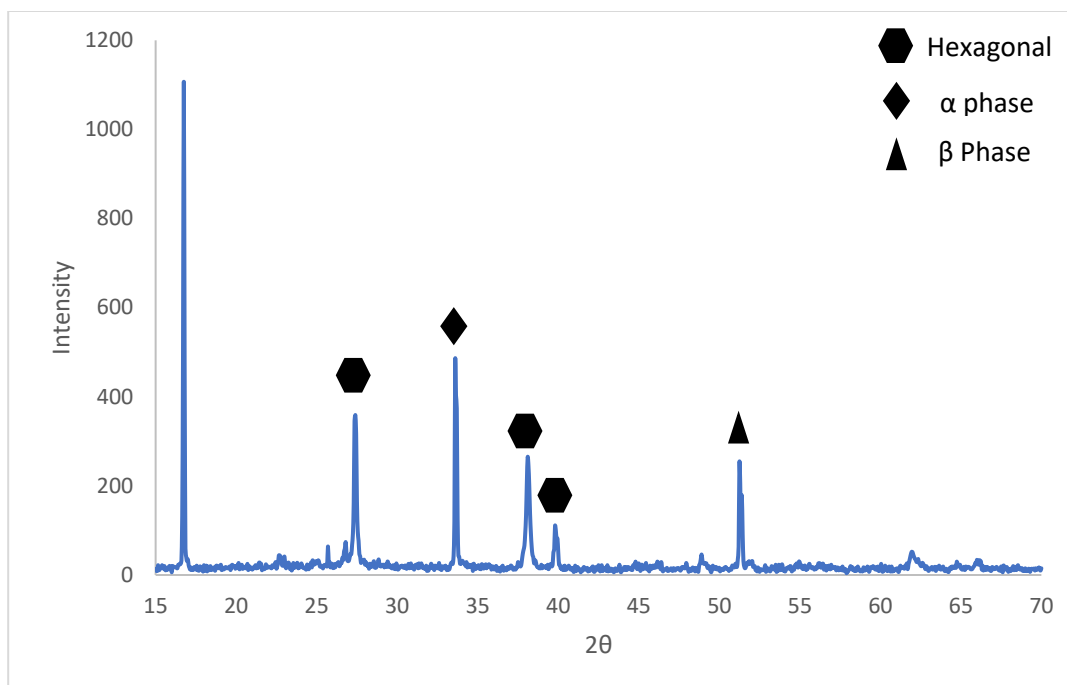


Figure 68: XRD post 1 mA experiment as deposited chrombismite

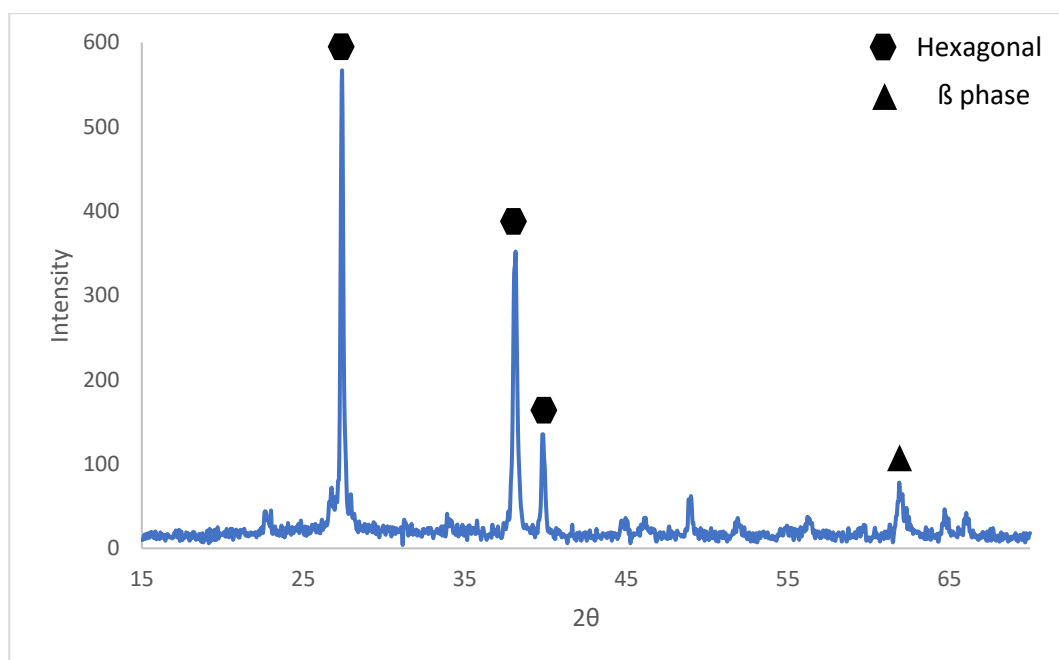


Figure 69: XRD post 1 mA experiment annealed chrombismite

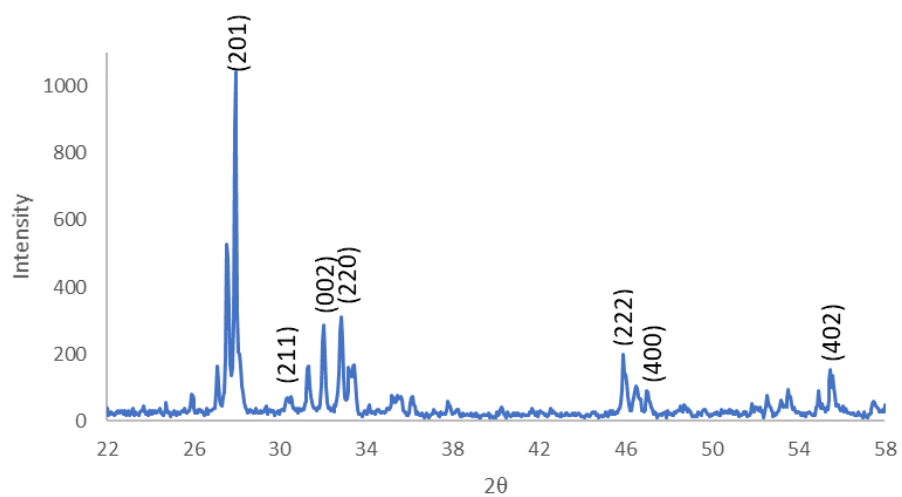


Figure 70: XRD of annealed β phase on ITO

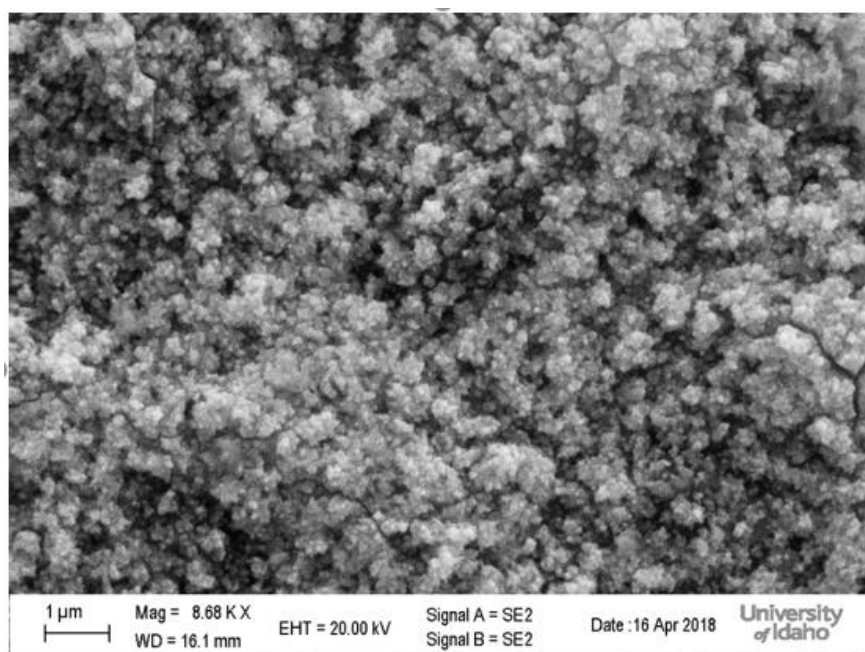


Figure 71: SEM of as deposited α Bi_2O_3 on ITO substrate

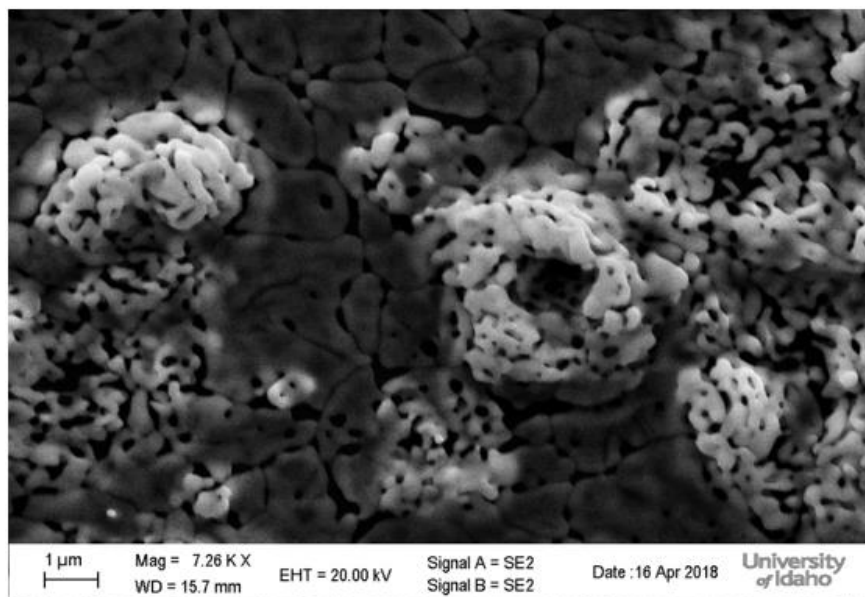


Figure 72: SEM of annealed α Bi_2O_3 on ITO substrate

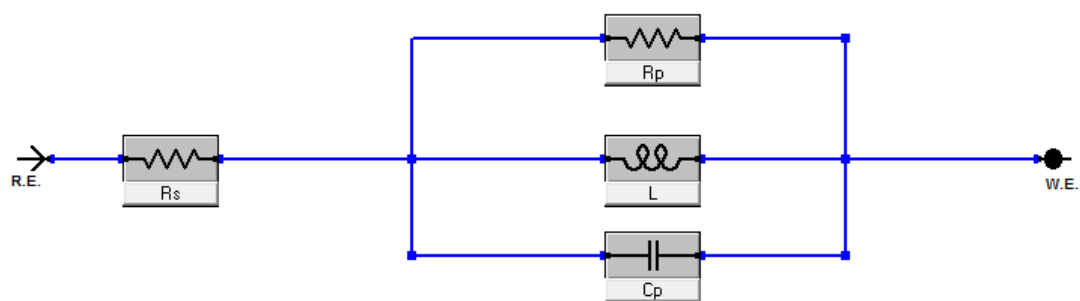


Figure 73: Circuit model for annealed α and β phase on ITO

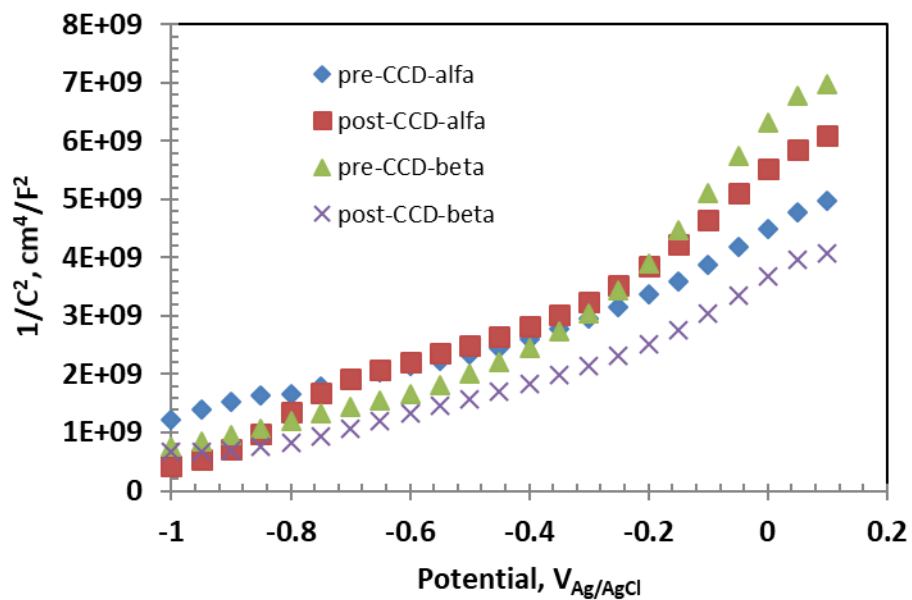


Figure 74: Charge carrier density for annealed α and β phase on ITO

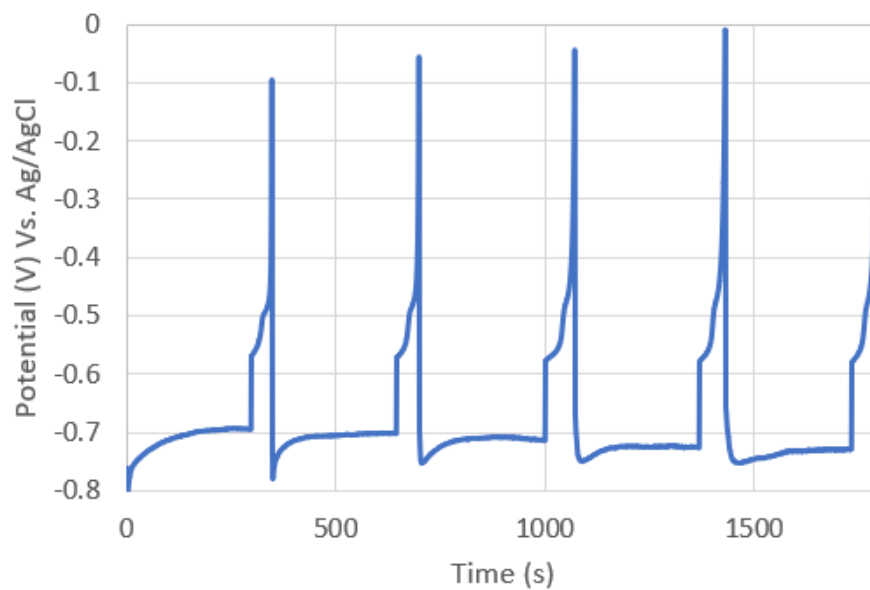


Figure 75: CCD of annealed α phase on ITO

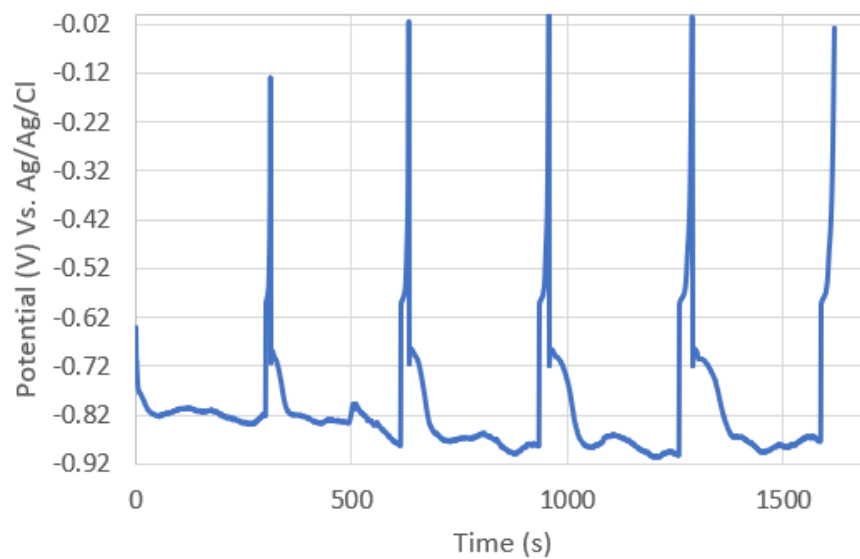


Figure 76: CCD of annealed β phase on ITO

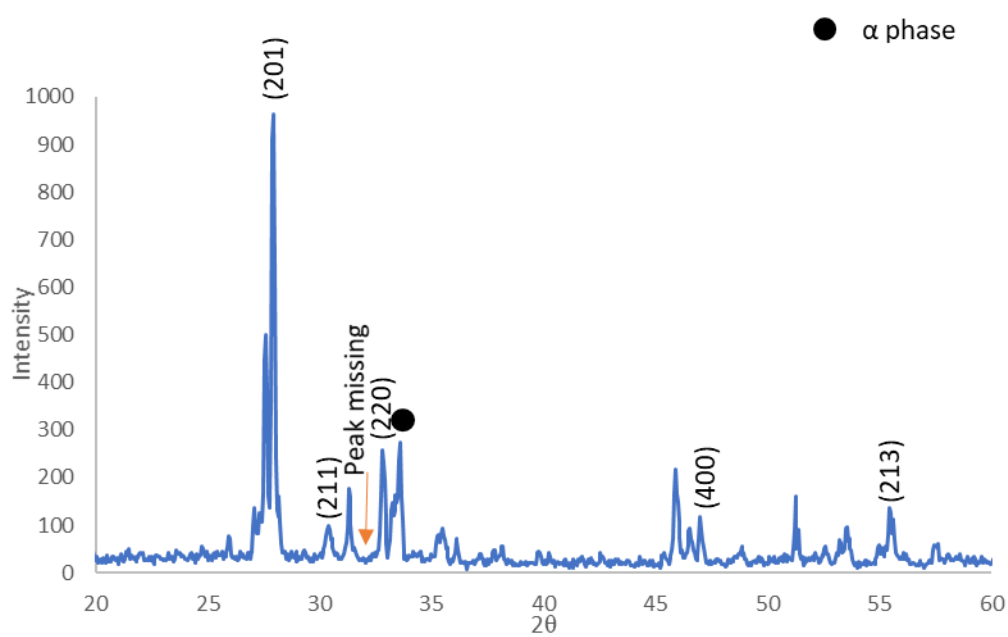


Figure 77: XRD of post CCD annealed β phase on ITO

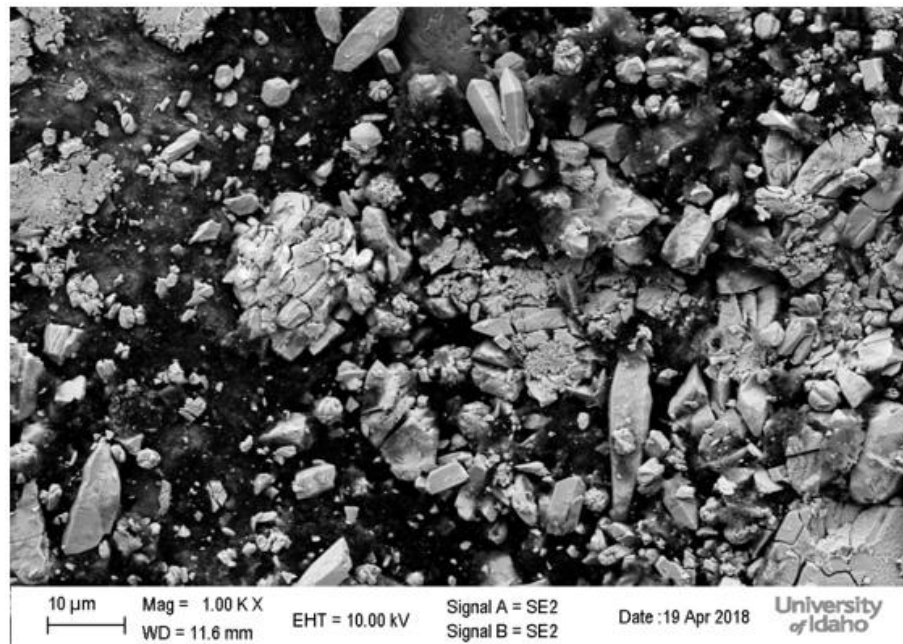


Figure 78: SEM of Bi_2O_3 pressed into nickel foam

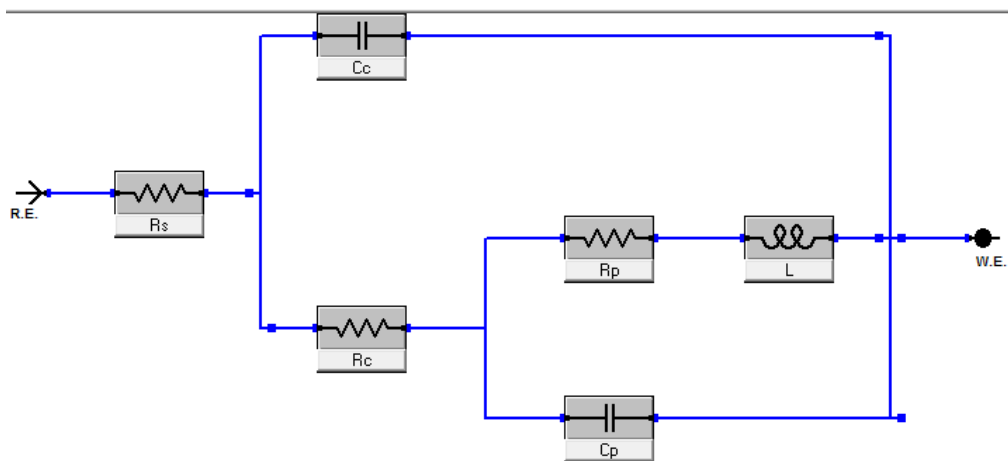


Figure 79: Equivalent Circuit for Bi_2O_3 Ni Foam composite

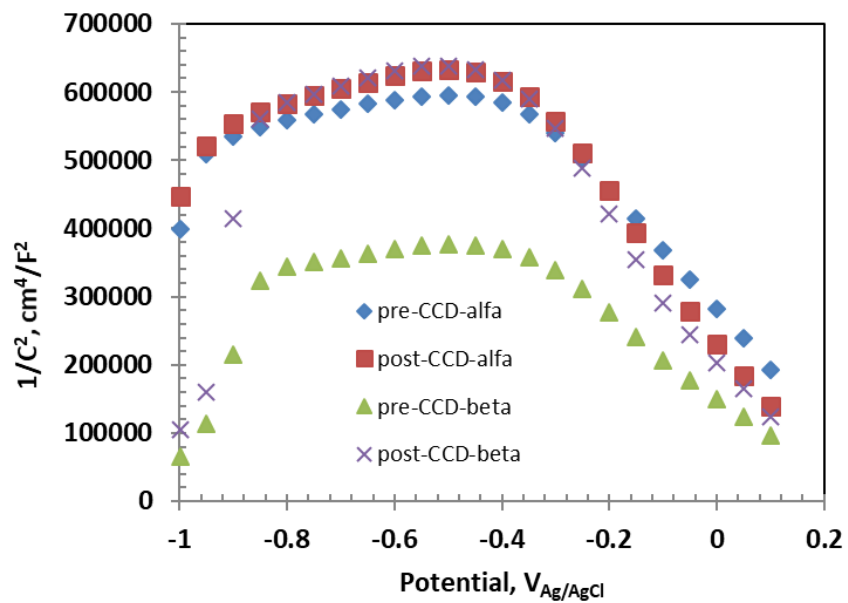


Figure 80: Mott Schottky data for Bi_2O_3 Ni Foam composite

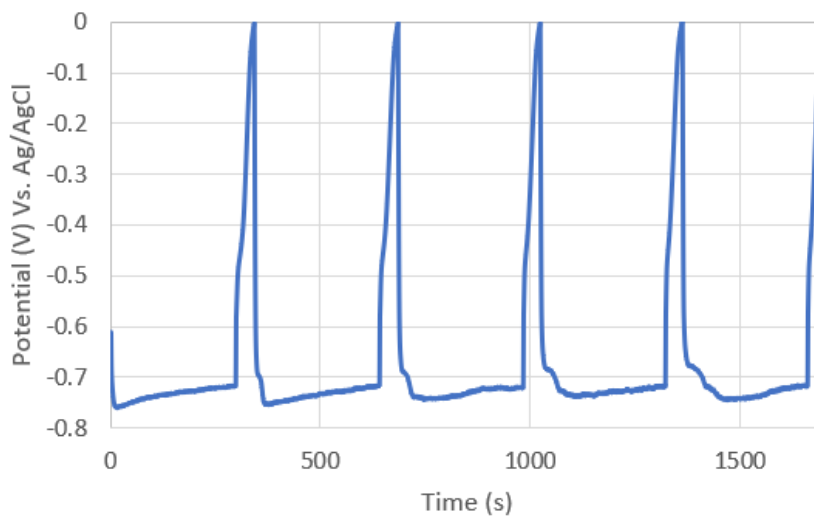


Figure 81: CCD for α phase Bi_2O_3 Ni Foam composite

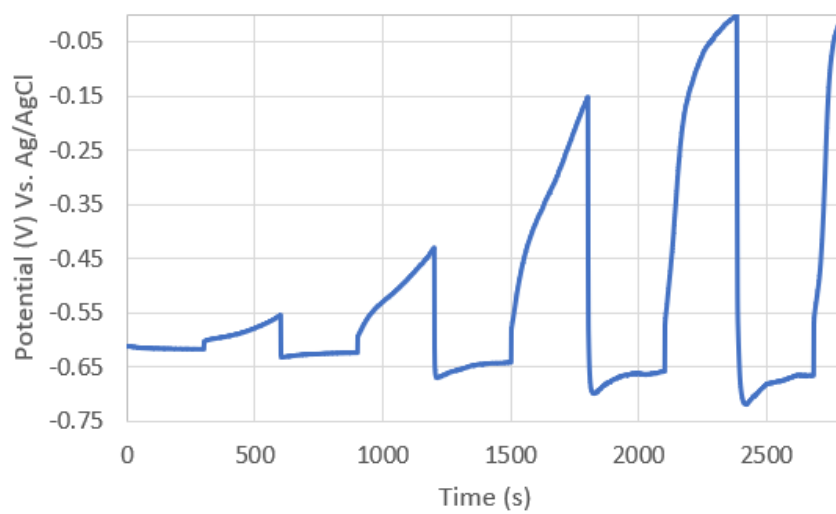


Figure 82: CCD for β phase Bi_2O_3 Ni Foam composite